5-13-2022

Lattice Boltzmann-based Sharp-interface schemes for conjugate heat and mass transfer and diffuse-interface schemes for Dendritic growth modeling

Nanqiao Wang
wangnanqiao@me.com

Lattice Boltzmann-based Sharp-interface schemes for conjugate heat and mass transfer and diffuse-interface schemes for Dendritic growth modeling

By

Nanqiao Wang

Approved by:

Like Li (Major Professor)
Heejin Cho
Matthew W. Priddy
Prashant Singh
Tonya W. Stone (Graduate Coordinator)
Jason M. Keith (Dean, Bagley College of Engineering)

A Dissertation
Submitted to the Faculty of
Mississippi State University
in Partial Fulfillment of the Requirements
for the Degree of Doctor of Philosophy
in Mechanical Engineering
in the Department of Mechanical Engineering

Mississippi State, Mississippi

May 2022

Name: Nanqiao Wang

Date of Degree: May 13, 2022

Institution: Mississippi State University

Major Field: Mechanical Engineering

Major Professor: Like Li

Title of Study: Lattice Boltzmann-based Sharp-interface schemes for conjugate heat and mass transfer and diffuse-interface schemes for Dendritic growth modeling

Pages in Study: 142

Candidate for Degree of Doctor of Philosophy

Analyses of heat and mass transfer between different materials and phases are essential in numerous fundamental scientific problems and practical engineering applications, such as thermal and chemical transport in porous media, design of heat exchangers, dendritic growth during solidification, and thermal/mechanical analysis of additive manufacturing processes. In the numerical simulation, interface treatment can be further divided into sharp interface schemes and diffuse interface schemes according to the morphological features of the interface. This work focuses on the following subjects through computational studies: (1) critical evaluation of the various sharp interface schemes in the literature for conjugate heat and mass transfer modeling with the lattice Boltzmann method (LBM), (2) development of a novel sharp interface scheme in the LBM for conjugate heat and mass transfer between materials/phases with very high transport property ratios, and (3) development of a new diffuse-interface phase-field-lattice Boltzmann method (PFM/LBM) for dendritic growth and solidification modeling.

For comparison of the previous sharp interface schemes in the LBM, the numerical accuracy and convergence orders are scrutinized with representative test cases involving both straight and curved geometries.

The proposed novel sharp interface scheme in the LBM is validated with both published results in the literature as well as in-house experimental measurements for the effective thermal conductivity (ETC) of porous lattice structures. Furthermore, analytical correlations for the normalized ETC are proposed for various material pairs and over the entire range of porosity based on the detailed LBM simulations. In addition, we provide a modified correlation based on the SS420-air and SS316L-air metal pairs and the high porosity range for specific application.

The present PFM/LBM model has several improved features compared to those in the literature and is capable of modeling dendritic growth with fully coupled melt flow and thermosolutal convection-diffusion. The applicability and accuracy of the PFM/LBM model is verified with numerical tests including isothermal, iso-solutal and thermosolutal convection-diffusion problems in both 2D and 3D. Furthermore, the effects of natural convection on the growth of multiple crystals are numerically investigated.

ACKNOWLEDGEMENTS

I would like to extend my deepest gratitude to my advisor, Dr. Like Li, who has provided invaluable support, encourage, and guidance during these years which contribute to completing this work. I am also grateful to my committee members Dr. Heejin Cho, Dr. Matthew Priddy, and Dr. Prashant Singh for all their guidance and help throughout my research. I would like to offer my special thanks to my colleagues David Korba and Inderjot Kaur who provided help and suggestions for my research for the past four years. Additionally, I would like to thank the Mechanical Engineering (ME) Department as well as my colleagues in ME. Finally, I would like to thank my family and my parents, for their patience, understanding, and support.

TABLE OF CONTENTS

LIST OF TABLES

LIST OF FIGURES

CHAPTER I

INTRODUCTION

1.1 Background

In almost all practical science and engineering applications involving heat and mass transfer, such as heat exchangers, thermochemical reactors, thermal and mass transport in porous media and particulate systems, dendritic growth, and the formation of interfacial patterns in solidification [1–11], conjugate conditions at the interface of different phases or materials with different properties are encountered. When using the computational fluid dynamics (CFD) method for heat and mass transfer, one of the major problems is the accurate and effective treatment of complex and/or moving boundaries. In general, interface schemes can be further divided into sharp and diffuse interface schemes. Sharp interfaces are characterized by a zero-width interface between materials/phases. This interface scheme that tracks the explicit local geometry is most often used, such as the aforementioned heat and mass transfer in porous media, and is most easily handable [12]. The basic and most famous conjugate conditions at the sharp interface include the continuity of temperature (concentration) and heat (mass) flux at the interface [13–16] . In contrast, the liquid-solid morphological features in the solidification of pure materials and alloys are extremely complex. Several numerical methods attempt to accurately calculate the interface normals and curvatures [17–20], but due to the problem of tracking sharp boundaries and solving small anisotropy, it is generally very difficult to produce reliable results [21]. Diffuse interface schemes are based on the idea that the phase interface is

not a thin/sharp interface, but instead a finite width with rapid yet smooth transitions in density, viscosity, and other physical properties. In the diffuse interface scheme, a phase-field variable is introduced to describe the bulk phases varies smoothly from zero to unity. Due to the complete avoidance of interface tracking, topology changes can be processed naturally without any special procedures [22].

The Lattice Boltzmann method (LBM) has become a powerful numerical method for simulating complicated geometric fluid flow and heat and mass transfer problems [23–26] with its advantages such as convenient boundary and interface processing. In the sharp interface scheme, the distribution functions (DFs) on the lattice node are determined by interpolation. The phase-field method (PFM), which employs the concept of a diffuse interface and introduces a phase-field variable has become a widely accepted technique for computational modeling of dendritic growth and interfacial pattern formation [27–29]. The inherent advantages of LBM (for example, simple and clear algorithms, convenient boundary/interface processing, and compatibility with parallelization) make it attractive to effectively simulate complex dendritic morphological evolution and all phase fields and flows. Therefore, more and more publications [30–33] have focused on coupling the PFM and LBM for dendrite growth during solidification.

The objective of this dissertation is to investigate the heat and mass transfer between different materials and phases computationally. The following topics have been studied:

Chapter II compares the accuracy and convergence orders of various popular interface schemes for conjugate heat and mass transfer modeling using the lattice Boltzmann method (LBM). The investigated sharp interface schemes are recognized to three groups and numerically tested by both straight and curved interfaces. It is important to understand the accuracy and

applicability of various interface schemes due to the wide involvement of conjugate conditions in heat and mass transfer in engineering applications.

In Chapter III, an LBM-based computational model for predicting the effective thermal conductivity (ETC) of lattice structures with different topologies was proposed and validated with published results and in-house experiments. Based on the LBM simulation results, analytical correlations for the normalized ETC are proposed.

Chapter IV presents a phase-field-lattice Boltzmann method (PFM/LBM)-based model for solidification and dendritic growth simulations with fully coupled melt flow and thermosolutal convection-diffusion. The proposed PFM/LBM model can be an attractive and powerful tool for large-scale dendritic growth simulations given the high scalability of the LBM.

1.2 Literature review

1.2.1 Conjugate heat and mass transfer modeling

Conjugate conditions at the interface of different phases or materials of distinct properties are encountered in almost all practical science and engineering applications involving heat and mass transfer, such as cooling of turbine blades and electronic devices, insulation for pipes, heat exchangers and thermochemical reactors, and thermal and mass transport in porous media and particulate systems, to name a few [1–11]. The basic and most well-known conjugate conditions include the continuity of both the temperature (concentration) and the heat (mass) flux at the interface [13–16]. Other conjugate conditions, such as with temperature (concentration) jumps and flux discontinuities [34–36], the Henry's law relationship [37], and the Kapitza resistance in heat transfer [38], are also noticed. Theoretical analysis for conjugate heat and mass transfer is limited as analytical solutions are only available to simple transport problems with regular geometry. Experimental measurement of interfacial values is often a challenge as the interfaces

are usually inaccessible to probing devices in most cases. Substantial research effort, as a result, has been devoted to numerical simulation of conjugate heat and mass transfer problems with effective interface treatment.

The common approach in dealing with conjugate conditions is to treat them as boundary conditions for the adjacent domains, and the heat and mass transfer in each domain can be solved separately using typical numerical methods for the convection-diffusion equations (CDE). Since the conjugate conditions are implicit (i.e., with given relationships between the scalar and its fluxes in the adjacent domains rather than the explicit interfacial values) and with both Dirichlet and Neumann type conditions, a popular approach for their implementation is applying iterative schemes, e.g., a predictor-corrector based Dirichlet condition is imposed for one domain and with that a Neumann condition can be constructed for the other; and the conjugate conditions at the interface can be satisfied after multiple iterations. Extrapolation is usually required in these iterative schemes to obtain the interfacial temperature (concentration) and fluxes. Conventional numerical methods, such as the finite difference and finite volume methods, therefore generally require substantial computational effort in order to satisfy the conjugate conditions with iterative schemes [39–42]. Moreover, introducing complex geometry or dynamic movement of the interface would further complicate the problem, for which effective and efficient numerical methods are needed.

1.2.2 Determination of effective thermal conductivity of porous lattice structures

The distinctive flow and thermal properties of the open-cell metal foams make them ideal candidates for the fabrication of lightweight and energy-efficient heat exchangers. The three-dimensionally (3D) interconnected metal-fiber skeleton offers high effective thermal conductivity (ETC) and surface area density. The tortuosity provided by the fiber network to the

flow assists in enhanced thermal dispersion. There have been extensive investigations on flow and thermal transport characteristics of high-porosity metal foams, where permeability (K), inertial coefficient (c_f), interstitial heat transfer coefficient (h_{sf}), effective thermal conductivity (k_{eff}) relationships were established with respect to pore density (pores per inch, *ppi*), pore- and fiber-diameter (d_p and d_f), porosities etc. For a comprehensive summary of such investigations, the reader is referred to [43–45]. For volume-averaged simulations, the steady-state energy transport equation with local thermal non-equilibrium between solid- and fluid-phases is given by $\nabla \cdot (k_{eff} \nabla T_s) - h_{sf} a_{sf} (T_s - T_f) = 0$, where T_s and T_f are solid and fluid phase temperatures, respectively. To accurately model the energy transport, the k_{eff} and h_{sf} are the critical quantities.

The k_{eff} determination studies can be broadly categorized into (a) experimental measurements performed on commercially procured metal foams, (b) estimation from theoretically developed empirical or semi-empirical models where the unknown coefficients/parameters were derived by juxtaposing the correlations with the experimental data, and (c) numerical predictions by simulating idealized, near-identical or exact geometries (obtained through μCT imaging). Several asymptotic equations to determine the lower and upper bounds of k_{eff} exist in the literature. The simplest one was obtained considering the conduction through series-mode and parallel-mode structures consisting of the solid and fluid phases, $k_{\perp} = (\frac{\varepsilon}{k_f} + \frac{1-\varepsilon}{k_s})^{-1}$, and $k_{\parallel} = \varepsilon k_f + (1-\varepsilon) k_s$, respectively, where k_f and k_s are the respective fluid- and solid-phase thermal conductivities. Asymptotic solutions for k_{eff} of heterogeneous mixtures were provided by Hadley [46] and Miller [47]. Later, authors including [48–50] suggested modifications to the relatively simple asymptotic models to extend their applicability to reticulated foams.

Experimental approaches have also been undertaken to determine k_{eff} of open-cell metal foams with different solid-fluid phase combinations, e.g. aluminum-air, aluminum-water. Calmidi and Mahajan [49] measured the ETC of aluminum metal foam samples of porosity (ε) values greater than 0.9 with both air and water as the saturated fluid. A simplified 2D hexagonal network with square-shaped intersection nodes was used to develop a theoretical expression for k_{eff} comprising one unknown geometrical parameter, the values of which was deduced by mapping the theoretical predictions with the experimental data. Bhattacharya et al. [51] extended the work presented in [49] by replacing square intersection nodes with circular metal blobs to derive modified analytical expressions. Paek et al. [52] experimentally determined the k_{eff} of aluminum metal foams with ε in the range of 0.89 to 0.96 for three different cell sizes. The ETC was strongly dependent on the porosity but was found to be independent of pore size. Yao et al. [53] measured k_{eff} of copper foams saturated with air, water and paraffin. The k_{eff} decreased with increase in porosity and showed negligible dependence on pore density. The copper foams yielded higher k_{eff} than aluminum foams at the same porosity because of the significantly higher thermal conductivity of the solid phase in case of copper foams. The ETC of nickel foams saturated with paraffin was measured experimentally by Xiao et al. [54], following which a theoretical model was developed which depicted good agreement with the measured values. Representative idealized unit cells are generally used by the researchers to obtain analytical expressions for k_{eff}. Two-dimensional (2D) hexagonal unit cell, representative cubic unit cells with square intersection nodes, 3D tetrakaidecahedron structure was used in several studies including [49,51,55–59] to derive analytical expressions for k_{eff}. Numerical simulations on idealized unit cells and microtomography-based images were conducted in [60–63] to obtain k_{eff}. A critical comprehensive review comparing several existing models with experimental data

including the above-mentioned references was provided by Ranut [43]. The author concluded that correlations including fitting constants provide satisfactory predictions and numerical simulations employing real μCT images or near-identical unit cells could provide accurate results.

Recently, additively manufactured (AM) cellular lattices have been investigated extensively due to the advantages they offer over the conventional metal foams, e.g. the morphological parameter design freedom while ensuring their repeatability and the benefit of zero thermal contact resistance between the substrate and the fibers in its contact. Commercially procured foams when used in cooling applications are typically brazed on the substrate to be cooled or glued on the substrate with the help of high thermal conductivity thermal interface materials (TIMs). The TIMs are usually in the form of pastes where high thermal conductivity particles are loaded at fairly low volume fraction (typically <5%) in a base epoxy. Due to inherent challenges with loading high volume fraction of filler materials, the ETC of TIMs are usually low (~1-5 W/mK), which imposes significant thermal resistance towards heat flow from the substrate to the heat sink.

Although AM related uncertainties in the realization of exact fiber and pore dimensions and unit cell topologies exist with the current state-of-the-art methods, the fact that complex reticulated structures can be fabricated opens up a new design space. From the perspective of k_{eff} determination for AM foams, numerical simulations of accurate model and experimental investigation of the same could yield results which are more consistent and universal for a given topology for a wide range of parameters, as the starting point is a CAD model of a unit cell with precise topology reticulated, in contrast to the previous approach of modeling a representative unit cell of randomly organized pores in metal foams made through *foaming* process. Qu et al.

[64] proposed a theoretical model to solve the ETC of the octet-truss structure based on 1D heat conduction analysis. By comparing with the experimental data, the prediction accuracy of the model was higher for $\varepsilon > 0.8$. Krishnan et al. [65,66] investigated the ETC of octet unit cell and the reported results are in good agreement with the expression of k_{eff} proposed by Gu et al. [67]. Bai et al. [68] considered the vertical heat conduction and simplified the model by neglecting the heat conduction between the air and the outer surface of the rod, and obtained a general expression of k_{eff} for stochastic and periodic structures.

The literature review suggests that most of the previous studies on the ETC analysis were based on semi-empirical correlations which determine the parameters from experimental data and pore-scale simulations of idealized unit cell or structures obtained from μCT imaging. The experimental investigation of the ETC of periodic cellular matrices with preserved geometry is relatively scarce (e.g., [65,66]), although several theoretical models have been reported [68,69]. In addition, the accuracy and applicability of the previous correlations for the ETC of AM structures need to be verified and improved, especially at relatively lower porosities (e.g., in [69], significant ETC deviation from the theoretical "one-third solidity law" can be observed at $0.8 < \varepsilon < 0.9$ for the Cube, Octet and TKD structures). Furthermore, future design and innovation in AM porous structures require general and reliable correlations to predict the ETC. Those considerations motivate the present study to develop accurate and convenient correlations for the ETC of AM structure based on an effective computational model that is able to preserve the geometry and considers heat condition in both phases and will be validated with experimental measurement of the same structures.

Numerical modeling of heat transfer in open-cell metal foams and prediction of transport properties including the ETC becomes a challenging task when the relative size of the strands is

very small and/or the intrinsic transport property ratio of the different materials is very high. When applying traditional numerical methods, a large number of grids/elements is typically required to resolve the conjugate heat transfer at the fluid-solid interface, and the computational time can be rather long due to the implementation of iterative interface schemes. For instance, in [65] for heat conduction simulation and ETC prediction for the octet structure, 0.86 million tetrahedral elements were needed following a mesh independence study.

1.2.3 PFM/LBM model for dendritic growth

Quantification and prediction of the evolution of the microstructure and segregation patterns of solidified pure materials and alloys are of great scientific and technological interest. The dendritic growth during solidification is a complex multiscale phenomenon that involves phase transition, melt flow, heat and solute convection-diffusion that are fully coupled at the evolving liquid-solid interface of complex morphology. In addition to the nature of multiphysics coupling, large transport property ratios are also encountered in the solidification process, for instance, the solutal diffusivity in the liquid state is generally two to four orders of magnitude smaller than the thermal diffusivity, and the solutal diffusivity in the solid state is typically two to four orders of magnitude smaller than that in the liquid [70]. It is also well known that solidification of alloys differs in many respects from solidification of pure substances, e.g., pure metals solidify at their definite melting point temperatures, while most alloys start to solidify at their liquidus temperatures and complete solidification at the solidus temperatures with the latter lower than the former; and undercooling related microstructure can only be produced by thermal means in pure metals, while in alloys it can be produced by changes in both temperature and composition. Direct simulation of solidification and crystal growth on the scale that captures the

local liquid-solid interface geometry (sharp interface) has thus experienced only limited progress [70].

The phase-field method (PFM), which employs the concept of a diffuse interface and introduces a phase field variable (with constant values in the bulk phases and varying steeply yet smoothly in the diffuse interface region), has become a widely accepted technique for computational modeling of dendritic growth and interfacial pattern formation. Several detailed reviews on phase-field modeling of dendritic growth can be found in [27–29]. While the present study focuses on solidification modeling, it should be noted that the PFM has broad applications in modeling and predicting mesoscale morphological and microstructure evolution in materials such as solid-state phase transformations, grain growth and coarsening, domain evolution in thin films [71], morphological evolution of multicomponent vesicles and solving nonlinear high-order PDEs [72–74], among others. In the early works, the PFM was only employed to model solidification controlled by pure diffusion, and the effects of thermal and solutal diffusion were mostly separately studied. The first *coupled* thermosolutal PFM was proposed in [70] where it was also demonstrated that the coupled model can reduce to the isothermal and iso-solutal cases. The effect of fluid flow and melt convection on the crystal growth was well recognized [75–78], but little work was reported mainly due to the lack of effective and reliable coupled models. Beckermann et al. [79] reported the first phase-field simulations including melt convection, in which the mass, momentum, energy, and species conservation equations in the diffuse interface region were formulated based on volume averaging; and a dissipative interfacial stress term (momentum sink) was introduced in the momentum equation to deal with the interaction at the liquid-solid interface. All the conservation equations were solved with traditional computational

fluid dynamics (CFD) schemes in [79]. Since then, a great number of publications on PFM modeling of dendritic growth under melt convection has been reported (e.g., [32,33,80–82]).

In the CFD and heat and mass transfer communities, the lattice Boltzmann method (LBM) has become a powerful and alternative numerical method for modeling fluid flows and thermal/mass transport problems with complex geometry due to its attractive features including simple algorithm, easy implementation, convenience in boundary and interface treatment, and compatibility with parallel computing [14,23,25,26,83–87]. It is no surprise that a growing number of publications have focused (e.g., [30–33]) on coupling the PFM and LBM for dendritic growth simulations. Most of those PFM-LBM models can be considered as *hybrid* models in which finite-difference- or finite-volume-based PFM was applied to simulate the phase field evolution, while the LBM was implemented to model the melt flow and heat and solute transfer. In addition, fully coupled PFM models considering all the effects of melt flow and thermosolutal convection-diffusion in the literature are very rare (e.g., [88]) due to the lack of general, convenient, and efficient numerical schemes.

CHAPTER II

ACCURACY OF SHARP INTERFACE SCHEMES FOR CONJUGATE HEAT AND MASS TRANSFER IN THE LATTICE BOLTZMANN METHOD*

This chapter presents a comparison of the popular interface schemes proposed in the literature with the focus on their numerical accuracy and convergence orders. The various interface schemes examined include the geometry-considered interpolation-based treatment that constructs second-order accurate corrections to the distribution functions across the interface by treating the interface as a shared boundary for the adjacent domains, as well as representative modified schemes that bypass the local geometry and topology consideration by either reformulating the macroscopic governing energy equation with additional source terms, or proposing modified microscopic equilibrium distribution functions in the lattice Boltzmann model. It is recognized that for the interface schemes based on governing equation reformulation, approximation of the discontinuous heat capacitance gradient at the interface is required to account for the interfacial heat flux continuity. Through analysis and numerical tests including both straight and curved interfaces, it is shown that in order to preserve the second-order accuracy in the LBM, the local interface geometry must be considered; and the modified geometry-ignored interface schemes result in degraded convergence orders – at most first order for general cases and only zeroth order is achieved for the schemes requiring discontinuous heat

* This chapter is based on work published in the International Journal of Heat and Mass Transfer in 2020 [89]

capacitance gradient approximation. In addition, much higher error magnitude is observed for the numerical solutions obtained from using these modified schemes without considering the interface geometry.

The structure of the remaining portions of this Chapter is as follows: Section 2.2 presents the governing equations for thermal and mass transfer, and the formal definition of the conjugate conditions. Section 2.3 briefly reviews the general lattice Boltzmann models for the convection diffusion equation for heat and mass transfer. Section 2.4 presents a comparison of the interface treatments for conjugate conditions, including those that require consideration of the local geometry and the three groups mentioned above. Benchmark test cases and numerical analysis are provided in Section 2.5. And Section 2.6 concludes the Chapter.

2.1 Introduction

The lattice Boltzmann method (LBM), which has emerged as an effective and powerful numerical method for complex flow simulations [23], [24], [25], [26], has also witnessed growing interest and success in heat and transfer modeling involving complex geometry and hydrodynamics-transport coupling [85], [87], [90], [91], [92], particularly with the development of lattice Boltzmann (LB) models that introduce two sets of distribution functions (DFs) to recover the Navier-Stokes equations for fluid flow and the CDE for heat and mass transfer, respectively. One of the main advantages of using the LBM for heat and mass transfer is the capability to formulate analytical relationships between the microscopic DFs and the macroscopic physical quantities in (1) the Dirichlet, Neumann and mixed boundary condition implementations, and (2) the evaluation of boundary temperature (concentration) and flux values and the interior thermal (mass) gradients [85,86,93]. This also makes the LBM an attractive numerical method for conjugate heat and mass transfer modeling, i.e., with appropriate interface

schemes, the conjugate conditions can be satisfied analytically during each time step without nested iterations [14,34]. A brief review of the various interface schemes for conjugate conditions is thus presented in the following, and the readers are referred to [85], [87], [86] for detailed reviews of LB models and boundary conditions in heat and mass transfer modeling.

The first work on conjugate heat transfer in LBM was due to Wang et al. [13], in which a "half lattice division" (HLD) scheme was originally proposed to account for the interfacial continuity, however the HLD scheme without correction to the DFs streamed to different domains was only applicable to steady cases with the interface located halfway in the lattice links. Since then, a number of other schemes have been proposed with the objective to satisfy the interfacial conjugate conditions [see 32 and refs therein]. In particular, with the interface treated as a shared boundary between the adjacent domains, the Dirichlet and Neumann boundary condition treatments by Li et al. [86] were combined and applied to interface conditions, and specific interface schemes were proposed in [14] for standard conjugate conditions, and in [34] for conjugate heat and mass transfer with interfacial jump conditions. Second-order accuracy of those interface schemes were verified for both steady and transient problems with straight interfaces located in arbitrary locations in the lattice, and their application to curved interfaces was also studied in [14,34], showing first-order convergence in general. This idea of constructing analytical relationships to modify the DFs across the interface to satisfy the conjugate conditions was also applied in [94] for a counter-extrapolation interface scheme. Moreover, it was also extended to handle general interface conditions in [35,36]. Specifically, Hu et al. [35] constructed interface schemes based on their boundary schemes for the mixed (Robin) conditions [95] for general interfacial conditions, including conjugate conditions with or without jumps in heat and mass transfer, continuity of macroscopic variables and normal fluxes in ion diffusion in

porous media with different porosity, and the Kapitza resistance in heat transfer. Mu et al. [36] further extended the works of Li et al. [14,34] and presented general interface schemes for the comprehensive conjugate conditions with and without interfacial jumps. Consistent with that in [14,34], second-order accuracy for straight interfaces and first-order accuracy for curved interfaces were also verified in [35,36]. Two key notes regarding the interface treatments presented in [14,34–36,94] are that: (1) there is no change in the LB models for the interior in the adjacent domains, i.e., only the DFs across the interface are modified, and (2) the local geometry, as denoted by the lattice link fractions at the interface, must be taken into account in constructing the interface schemes to preserve the second-order accuracy, which requires additional effort and computational resource compared to the simple HLD scheme, especially for curved interfaces or those with complex geometry such as heat and mass transfer in porous media.

Driven by the motivation to bypass the aforementioned consideration of the local geometry or topology at the interface, other methods have also been developed in the LBM community [16,96–107] to model conjugate heat and mass transfer problems. In those approaches, either the macroscopic governing CDE or the microscopic DF in the LB models is modified. We categorize them into three groups with representative examples briefly reviewed. In *Group 1*, additional source terms were introduced in the reformulated CDE for conjugate heat transfer and their implementation follows the standard source term treatment in LB models. For example, Karani and Huber [96] used the conservative form of the energy equation to formulate an additional source term to correct for the difference in heat capacitance between the two materials. Their method demonstrated only first-order accuracy for the diffusion in a 3-layered stratified medium and the convection diffusion in a horizontal channel. They attributed the degradation in the order-of-accuracy to the 1st-order finite-difference approximation of the heat

capacitance gradient at the interface. Hu et al. [100] also formulated a modified CDE that contains a source (correction) term utilizing the Dirac function and a heat flux jump function across the interface, following their previous work in [101]. Only first-order accuracy was obtained in [100,101] even for straight interfaces and the degraded convergence order was attributed to the utilization of discrete delta functions in the formulation.

In *Group 2*, enthalpic formulations were applied to convert the energy conservation equation for temperature to a CDE for the enthalpy-like quantity with additional source terms [102,103]. Similar to the model presented by Karani and Huber [96], this formulation also requires an approximation of the gradient in heat capacitance at the interface. The authors in [102] showed near second-order convergence for a simple diffusion problem, however, no detailed error analysis was presented for convection and diffusion problems or for general interface geometry.

In *Group 3*, modified microscopic DFs were defined in the LB models for conjugate conditions [16,97–99,104–107]. In [16], it was assumed that the interface is always located at the halfway point between the lattice nodes in the two adjacent domains. Second-order accuracy for straight interfaces located halfway in the lattice and first-order accuracy for curved interface are demonstrated in [16]. The alternative interface schemes in [97–99,104–107] aimed at avoiding the modification of the local DFs at the lattice links across the interface, rather by modifying the LB model over the full domain so that the local interface geometry could be ignored. The expressions for the modified DFs in those models are similar to each other, with higher-order terms neglected in some models. It was claimed in the LB models [97,104–107] that the conjugate conditions between different materials are “automatically satisfied” with the modified DFs. While general agreement between LBM simulations and the analytical or previously

published results is shown, a detailed order-of-accuracy analysis for general conjugate heat and mass transfer problems with both straight and curved interfaces is lacking in these models.

Lastly, it should be noted that the above group classification is not exclusive and there can be overlap between the three groups. For instance, the enthalpy-based energy equation formulation in Group 2 was also implemented in [98,99] for conjugate heat transfer problems involving solid-liquid phase change, and modified DFs similar to those in Group 3 were used in their interface treatment.

2.2 Formulation of conjugate heat and mass transfer

2.2.1 Governing equations

The energy equation can be written as

$$\rho c_p \frac{DT}{Dt} = \rho c_p [\frac{\partial T}{\partial t} + \nabla \cdot (\mathbf{u}T)] = \nabla \cdot (k \nabla T) + S_T , \tag{2.1}$$

where ρ is the density, c_p the specific heat, T the temperature, t the time, $\mathbf{u}$ the velocity vector, k the thermal conductivity, and S_T the source term. It is worth noting that Eq. (2.1) is the correct conservation form and it should not follow the form of

$$\rho c_p \frac{\partial T}{\partial t} + \nabla \cdot (\rho c_p \mathbf{u}T) = \nabla \cdot (k \nabla T) + S_T , \tag{2.2}$$

as used in [96], since from the control volume analysis for energy conservation $\frac{Dh}{Dt} = \left(\frac{\partial h}{\partial T}|p = c\right)\frac{DT}{Dt} + \left(\frac{\partial h}{\partial p}|T = c\right)\frac{Dp}{Dt} \simeq c_p \frac{DT}{Dt}$ for low speed incompressible flows with h the specific enthalpy, i.e., $Dh = c_p DT$, rather than $h = c_p T$, should be used in deriving Eq. (2.2). One can rewrite Eq. (2.3) as

$$\frac{\partial T}{\partial t} + \nabla \cdot (\mathbf{u}T) = \nabla \cdot (\frac{k}{\rho c_p} \nabla T) + G_T , \tag{2.3}$$

with the modified source term

$$G_T = -k_{ij}\frac{\partial T}{\partial x_j}\frac{\partial}{\partial x_i}\left(\frac{1}{\rho c_p}\right) + \frac{S_T}{\rho c_p}. \tag{2.4}$$

For mass transport, the governing equation is

$$\frac{\partial C}{\partial t} + \nabla\cdot(\mathbf{u}C) = \nabla\cdot(D_m\nabla C) + S_C, \tag{2.5}$$

where C is the concentration, D_m the mass diffusivity, and S_C the source term. It is easily seen that both the energy and mass transport equations (2.3) and (2.5) follow the standard form of the convection diffusion equation (CDE) with source terms that can be written as

$$\frac{\partial \phi}{\partial t} + \nabla\cdot\left(\mathbf{u}\phi\right) = \nabla\cdot\left(D\nabla\phi\right) + G. \tag{2.6}$$

2.2.2 Conjugate conditions at the interface

The generalized conjugate conditions at an interface for the interfacial scalar variable (ϕ) and fluxes can be expressed as

$$\phi_f = \phi_s + \phi_{\text{jump}}, \tag{2.7}$$

$$\mathbf{n}\cdot(k\nabla\phi + \rho c_p\mathbf{u}\phi)_f = \mathbf{n}\cdot(k\nabla\phi + \rho c_p\mathbf{u}\phi)_s + \mathbf{n}\cdot q^T_{\text{jump}}, \tag{2.8}$$

$$\mathbf{n}\cdot(D_m\nabla\phi + \mathbf{u}\phi)_f = \mathbf{n}\cdot(D_m\nabla\phi + \mathbf{u}\phi)_s + \mathbf{n}\cdot q^C_{\text{jump}}, \tag{2.9}$$

where the subscripts denote the two adjacent domains such as those for fluid-solid conjugate conditions. Physical interpretation of the conjugate heat and mass transfer conditions includes the continuity (or prescribed resistance) of the scalar variable and the normal fluxes at the interface of the adjacent domains. It is noted that the normal fluxes in Eqs. (2.8, 2.9) include both the diffusive and convective components [32,38], and ϕ_{jump} and q_{jump} are possible jump conditions at the interface [16-18] to account for thermal or mass transport resistance. Additional treatment at the interface is required to recover the conjugate conditions with scalar or flux

jumps in Eqs. (2.8, 2.4); however, to show a clear comparison of the various interface schemes for conjugate conditions, we consider only in this paper the transport problems with no jumps. In addition, when the normal component of the velocity is zero at the interface, Eqs. (2.7-2.5) reduce to the basic conjugate conditions as

$$\phi_f = \phi_s, \tag{2.10}$$

$$\mathbf{n}\cdot(D\nabla\phi)_f = \sigma\mathbf{n}\cdot(D\nabla\phi)_s \tag{2.11}$$

where $D = \frac{k}{\rho c_p}$, $\sigma = \frac{(\rho c_p)_s}{(\rho c_p)_f}$ at the interface in heat transfer, and $D = D_m$, σ = 1 in mass transfer problems [14,34].

It is emphasized that for conjugate heat transfer between different materials with distinct heat capacitance, i.e., $\sigma \neq 1$ at the interface, the treatment of the first term on the right side of Eq. (2.4) requires caution. When the CDE in each domain is solved separately with the geometry-considered interface treatment implemented, there is no need to deal with this term across the sharp interface. However, when using the geometry-ignored interface treatment as in Groups 1 and 2, finite-difference type schemes are required to discretize the heat capacitance gradient at the lattice nodes next to the interface, which is assumed to be located in the middle of the lattice link. Importantly, even for the most basic situation with constant and distinct heat capacitances in the two domains ($\sigma = const \neq 1$), a discontinuity shows up in the profile of ρc_p across the interface, for which the discretization of the heat capacitance gradient $\frac{\partial}{\partial x_i}\left(\frac{1}{\rho c_p}\right)$ at the adjacent lattice nodes would introduce significant numerical errors. This will be demonstrated in Chapter 2.4 with numerical examples.

2.3 Lattice Boltzmann model for the convection-diffusion equation (CDE)

The evolution equation in the standard LB model that recovers the CDE in Eq. (2.6) can be written as [85,87]

$$g_\alpha\left(\mathbf{x}+\mathbf{e}_\alpha\delta t, t+\delta t\right)-g_\alpha\left(\mathbf{x},t\right)=\left[\mathbf{L}\cdot\left(\mathbf{g}-\mathbf{g}^{\mathrm{eq}}\right)\left(\mathbf{x},t\right)\right]_\alpha+\omega_\alpha G\left(\mathbf{x},t\right)\delta t\,, \tag{2.12}$$

where the microscopic distribution function, $g_\alpha(\mathbf{x}, t) \equiv g(\mathbf{x}, \xi_\alpha, t)$, is defined in the discrete velocity space, ξ is the particle velocity vector that is discretized to a small set of discrete velocities $\{\xi_\alpha|\alpha = 0, 1, \ldots, m - 1\}$, $\mathbf{e}_\alpha$ the αth discrete velocity vector, δt the time step, $\mathbf{L}$ the collision operator, $g_\alpha^{\mathrm{eq}}\left(\mathbf{x},t\right)$ the equilibrium distribution function, and ω_α the weight coefficient. The macroscopic scalar variable is obtained from

$$\phi\left(\mathbf{x},t\right)=\sum_{\alpha=0}^{m-1}g_\alpha\left(\mathbf{x},t\right). \tag{2.13}$$

A comparison of the different lattice structures was studied by Li et al. [87], and the D2Q5 model by Yoshida and Nagaoka [85] will be used in this work, for which the equilibrium DF is

$$g_\alpha^{\mathrm{eq}}=\omega_\alpha\phi\left(1+\frac{\mathbf{e}_\alpha\cdot\mathbf{u}}{c_s^2}\right). \tag{2.14}$$

Regarding the collision operator $\mathbf{L}$, there are three popular models in the literature. The earliest and simplest one is the BGK [108] or single-relaxation-time (SRT) model

$$\left[\mathbf{L}\cdot\left(\mathbf{g}-\mathbf{g}^{\mathrm{eq}}\right)\right]_\alpha=\lambda\left(g_\alpha-g_\alpha^{\mathrm{eq}}\right)=-\frac{1}{\tau}\left(g_\alpha-g_\alpha^{\mathrm{eq}}\right), \tag{2.15}$$

where τ is the relaxation coefficient/parameter.

In addition, the TRT model [109] has also been successfully applied in various situations. In the most general multiple-relaxation-time (MRT) model, a transformation matrix $\mathbf{M}$ is

introduced to map the DFs to the moment space: $\mathbf{m} = \mathbf{M}\cdot\mathbf{g}$ and $\mathbf{m}^{eq} = \mathbf{M}\cdot\mathbf{g}^{eq}$, and the collision operator is

$$\left[\mathbf{L}\cdot\left(\mathbf{g}-\mathbf{g}^{eq}\right)\right]_\alpha = -\left[\mathbf{M}^{-1}\mathbf{S}\mathbf{M}\cdot\left(\mathbf{g}-\mathbf{g}^{eq}\right)\right]_\alpha = \left[\mathbf{M}^{-1}\mathbf{S}\cdot\left(\mathbf{m}-\mathbf{m}^{eq}\right)\right]_\alpha, \tag{2.16}$$

where $\mathbf{S}$ is a matrix of relaxation time coefficients following

$$\tau_{ij} = \frac{1}{2}\delta_{ij} + \frac{\delta t}{\varepsilon_D \delta x^2} D_{ij}, \tag{2.17}$$

in order to recover the CDE. For the D2Q5 model, $\varepsilon_D = 1/3$, and the equilibrium moments are

$$\mathbf{m}^{eq} = \left[\phi, u\phi, v\phi, 2\phi/3, 0\right]^{\mathrm{T}}. \tag{2.18}$$

More details for the D2Q5 LB model, including the matrices $\mathbf{M}$ and $\mathbf{S}$, can be found in [85,87].

The standard "collision-streaming" procedure is also used in this work for efficient computational implementation, with

collision step:

$$\hat{g}_\alpha\left(\mathbf{x},t\right) = g_\alpha\left(\mathbf{x},t\right) - \left[\mathbf{M}^{-1}\mathbf{S}\cdot\left(\mathbf{m}-\mathbf{m}^{eq}\right)\left(\mathbf{x},t\right)\right]_\alpha + \omega_\alpha G\left(\mathbf{x},t\right)\delta t, \tag{2.19}$$

streaming step:

$$g_\alpha\left(\mathbf{x}+\mathbf{e}_\alpha\delta t, t+\delta t\right) = \hat{g}_\alpha\left(\mathbf{x},t\right), \tag{2.20}$$

where $\hat{g}_\alpha$ represents the post-collision state.

2.4 Interface treatment for conjugate conditions

2.4.1 Interface schemes considering local geometry

In the earlier interface treatment [13,14,34] the DFs at the lattice nodes next to the interface are updated in each time-marching step to satisfy the conjugate conditions. In particular, in the interface treatment proposed by Li et al [14], second-order accurate schemes were derived by constructing a system of equations with the sharp interface considered as a shared boundary for the adjacent domains. With the local link fraction included in the interface

schemes, the second-order accuracy is preserved for parallel straight interfaces located in arbitrary locations within the lattice. Furthermore, the extension of the interface schemes to curved geometry was also studied in [14,34,36] by coupling the interfacial fluxes in the discrete lattice velocity directions using the "Cartesian decomposition method" originally developed in [86]. For brevity, only the decoupled interface scheme, i.e., when the normal of the straight interface is in parallel with one of the discrete velocity vectors in the LB model, is given below; one can refer to [14,34] for more details regarding the coupled interface schemes for inclined or curved interfaces.

$$\begin{aligned} g_{\bar{\alpha}}\left(\mathbf{x}_f, t+\delta t\right) = {} & A_1^f \hat{g}_{\alpha}\left(\mathbf{x}_f, t\right) + A_2^f \hat{g}_{\alpha}\left(\mathbf{x}_{ff}, t\right) + A_3^f \hat{g}_{\bar{\alpha}}\left(\mathbf{x}_f, t\right) \\ & + B_1^f \hat{g}_{\bar{\alpha}}\left(\mathbf{x}_s, t\right) + B_2^f \hat{g}_{\bar{\alpha}}\left(\mathbf{x}_{ss}, t\right) + B_3^f \hat{g}_{\alpha}\left(\mathbf{x}_s, t\right) \end{aligned}, \tag{2.21}$$

$$\begin{aligned} g_{\alpha}\left(\mathbf{x}_s, t+\delta t\right) = {} & A_1^s \hat{g}_{\bar{\alpha}}\left(\mathbf{x}_s, t\right) + A_2^s \hat{g}_{\bar{\alpha}}\left(\mathbf{x}_{ss}, t\right) + A_3^s \hat{g}_{\alpha}\left(\mathbf{x}_s, t\right) \\ & + B_1^s \hat{g}_{\alpha}\left(\mathbf{x}_f, t\right) + B_2^s \hat{g}_{\alpha}\left(\mathbf{x}_{ff}, t\right) + B_3^s \hat{g}_{\bar{\alpha}}\left(\mathbf{x}_f, t\right) \end{aligned}, \tag{2.22}$$

where

$$\begin{cases} A_i^f = \left(\dfrac{\sigma c_{di}}{c_{d4}^* c_{n4}^*} + \dfrac{c_{ni}}{c_{d4}^* c_{n4}} \right) / P \\ B_i^f = \sigma \left(\dfrac{c_{ni}^* - c_{di}^*}{c_{d4}^* c_{n4}^*} \right) / P \\ A_i^s = \left(\dfrac{c_{di}^*}{c_{d4}^* c_{n4}} + \dfrac{\sigma c_{ni}^*}{c_{d4}^* c_{n4}^*} \right) / P \\ B_i^s = \left(\dfrac{c_{ni} - c_{di}}{c_{d4} c_{n4}} \right) / P \end{cases}, (i = 1,2,3), \tag{2.23}$$

with

$$P = \frac{\sigma}{c_{d4}^* c_{n4}^*} + \frac{1}{c_{d4}^* c_{n4}}, \tag{2.24}$$

where $\mathbf{x}_{ff}$ and $\mathbf{x}_{ss}$ are the second closest lattice nodes to the interface in the respective two domains, i.e., $\mathbf{x}_{ff} = \mathbf{x}_f + \mathbf{e}_{\bar{\alpha}}\delta t$ and $\mathbf{x}_{ss} = \mathbf{x}_s + \mathbf{e}_{\alpha}\delta t$, c_{d1}-c_{d4} and c_{n1}-c_{n4} are the coefficients related to the local link fraction $\Delta = ||\mathbf{x}_f - \mathbf{x}_w||/||\mathbf{x}_f - \mathbf{x}_s||$ in Domain 1 for the second-order accurate Dirichlet and Neumann boundary conditions, respectively [86], and the coefficients c_{di}^* and c_{ni}^* (i = 1, 2, 3 and 4) are related to c_{di} and c_{ni} as

$$c_{di}^* = c_{di}\left(\Delta^*\right) = c_{di}\left(1-\Delta\right), \tag{2.25}$$

$$c_{ni}^* = c_{ni}\left(\Delta^*\right) = c_{ni}\left(1-\Delta\right), \tag{2.26}$$

since the intersection fraction in Domain 2 is $\Delta^* = ||\mathbf{x}_s - \mathbf{x}_w||/||\mathbf{x}_f - \mathbf{x}_s|| = 1 - \Delta$ [14].

There is one adjustable parameter in the second-order Dirichlet scheme and three particular schemes were proposed in [86] as

$$\text{Scheme 1: } c_{d1} = \begin{cases} -2\Delta, (0 \le \Delta \le 0.5), \\ -\dfrac{1}{2\Delta}, (\Delta > 0.5), \end{cases} \tag{2.27}$$

$$\text{Scheme 2: } c_{d1} = -2(1-\Delta), \text{ and} \tag{2.28}$$

$$\text{Scheme 3: } c_{d1} = -1, \tag{2.29}$$

and the other coefficients are related to c_{d1} as

$$c_{d2} = -\frac{2\Delta c_{d1}+1}{2\Delta+1}, c_{d3} = \frac{c_{d1}+2\Delta}{2\Delta+1}, c_{d4} = \frac{-c_{d1}+1}{2\Delta+1} \tag{2.30}$$

thus three particular interface schemes corresponding to those in Eq. (2.27-2.29) were obtained [14]. For the second-order Neumann scheme, the coefficients are uniquely determined with

$$c_{n1} = 1, c_{n2} = -\frac{2\Delta-1}{2\Delta+1}, c_{n3} = \frac{2\Delta-1}{2\Delta+1}, c_{n4} = \frac{2}{2\Delta+1} \tag{2.31}$$

Clearly, for straight interfaces located "halfway" between the lattice nodes (Δ = 0.5), the decoupled interface scheme in Eqs. (2.21, 2.22) reduces to

$$g_{\bar{\alpha}}\left(\mathbf{x}_f, t+\delta t\right)=\left(\frac{1-\sigma}{1+\sigma}\right)\hat{g}_{\alpha}\left(\mathbf{x}_f, t\right)+\left(\frac{2\sigma}{1+\sigma}\right)\hat{g}_{\bar{\alpha}}\left(\mathbf{x}_s, t\right), \tag{2.32}$$

$$g_{\alpha}\left(\mathbf{x}_s, t+\delta t\right)=-\left(\frac{1-\sigma}{1+\sigma}\right)\hat{g}_{\bar{\alpha}}\left(\mathbf{x}_s, t\right)+\left(\frac{2}{1+\sigma}\right)\hat{g}_{\alpha}\left(\mathbf{x}_f, t\right), \tag{2.33}$$

In this half lattice division (HLD) scheme, only the local DFs at $\mathbf{x}_f$ and $\mathbf{x}_s$ are required. It is worth noting that single-node second-order accurate interface schemes were also proposed in [35]; however, those schemes use complex coefficients that are dependent not only on the local link fraction, but also the relaxation coefficients in the two domains [35,95]. The conclusion on the order-of-accuracy of those geometry-considered interface schemes in [14,34–36,94] is consistent, and thus only the original scheme proposed in [14] is implemented in this work for numerical tests.

2.4.2 Modified geometry-ignored interface schemes

The details for the various modified interface schemes for conjugate heat and mass transfer are presented in this section. These schemes were constructed with the objective to bypass the consideration of the local geometry at the interface and eliminate the update or correction of the DFs across the interface. The implementation of the modified schemes is applied to the entire domain for efficient computation especially for complex geometry. This study focuses on the analysis of their numerical accuracy compared to the original geometry-considered interpolation-based interface schemes [14,34–36,94]. As discussed in the Introduction, we categorize them into three groups for convenience according to the formulation of the governing equations and the LB model modification. Most of those schemes were formulated for conjugate heat transfer problems with $\sigma \neq 1$ in Eq. (2.11), and for conjugate mass transfer $\sigma = 1$, the interface treatment becomes much simpler.

2.4.2.1 Group 1: introduction of additional source terms in the energy equation

In the first group, the governing CDE for temperature was reformulated with additional source terms to account for the conjugate conditions. Representative examples include those in [96,100,101]. While those formulations were demonstrated to preserve the continuity of interfacial temperature and heat flux for the standard conjugate conditions from a theoretical point of view; their numerical implementation can be problematic or incapable of preserving the second-order accuracy in the LBM due to the treatment of the gradient of the heat capacitance (see Eq. (2.4)). Specifically, in [96], a one-sided finite-difference approximation was directly used for the gradient; and in [100,101], Dirac and discrete delta functions were applied and much more complicated formulations were presented. For brevity, the modified interface treatment in [96] is selected and summarized below to represent the Group 1 schemes.

Following the source term treatment in [96], the heat capacitance gradient at the lattice nodes with indices k and $k + 1$ next to the interface is approximated as (assuming the interface is located halfway between nodes k and $k + 1$)

$$\frac{\partial}{\partial x_i}\left(\frac{1}{\rho c_p}\right)_k = \frac{\dfrac{1}{(\rho c_p)_{avg}} - \dfrac{1}{(\rho c_p)_k}}{0.5\delta x}\mathbf{n}_i \tag{2.34}$$

$$\frac{\partial}{\partial x_i}\left(\frac{1}{\rho c_p}\right)_{k+1} = \frac{\dfrac{1}{(\rho c_p)_{k+1}} - \dfrac{1}{(\rho c_p)_{avg}}}{0.5\delta x}\mathbf{n}_i \tag{2.35}$$

with $\left(\rho c_p\right)_{\text{avg}} = \left[\left(\rho c_p\right)_k + \left(\rho c_p\right)_{k+1}\right] \big/ 2$ the averaged value at the interface, and $\boldsymbol{n}_i$ the unit normal vector in x_i-direction. Thus the additional source term, i.e., the first term in Eq. (2.4), is obtained from

$$-k_{ij}\frac{\partial T}{\partial x_j}\frac{\partial}{\partial x_i}\left(\frac{1}{\rho c_p}\right)_{k,k+1}=\frac{2(\sigma-1)}{\sigma+1}\mathbf{n}_i\left(D_{ij}\frac{\partial T}{\partial x_j}\right)_{k,k+1} \tag{2.36}$$

where $\sigma=\left(\rho c_p\right)_{k+1}/\left(\rho c_p\right)_k$. Since $(x_i)_k$ and $(x_i)_{k+1}$ are the interior nodes, the temperature gradient in Eq. (2.36) can be conveniently obtained from the moment of the non-equilibrium DFs [85–87,110], yielding

$$-k_{ij}\frac{\partial T}{\partial x_j}\frac{\partial}{\partial x_i}\left(\frac{1}{\rho c_p}\right)_{k,k+1}=-\frac{2(\sigma-1)}{\sigma+1}\mathbf{n}_i\frac{\delta x}{\delta t}\left(\sum_{\alpha=1}^{m}e_{\alpha i}g_\alpha^{\mathrm{neq}}-\frac{\delta_{ij}}{2\tau_{ij}}\sum_{\alpha=1}^{m}e_{\alpha j}g_\alpha^{\mathrm{neq}}\right)_{k,k+1} \tag{2.37}$$

As pointed out in [96], the treatment of the source term in Eq. (2.37) can be applied to the entire computational domain as its value will be zero everywhere except at the nodes $(x_i)_k$ and $(x_i)_{k+1}$ next to the interface where the heat capacitance experiences a jump. It is worth noting that such a statement is only valid for the simplest case where the heat capacitance is constant in each domain. More importantly, finite-difference type approximation of the gradient of a jump function, such as the first-order scheme in Eq. (2.34, 2.35) or any higher-order schemes, could result in substantial numerical errors. It is noted that the above source term treatment in Eq. (2.37) is equivalent to the flux source terms in Eqs. (41, 42) of [100] where the Dirac function was used. For simple heat transfer problems with small capacitance ratios, first-order convergence could be obtained with a coarse grid, which was also observed in [96,100]; however, for large σ values, the effect of the jump condition becomes crucial and zeroth-order convergence is expected. This will be demonstrated with detailed numerical tests in Chapter 2.5.

2.4.2.2 Group 2: enthalpy-based formulation for the energy equation

In this group, enthalpic formulations were applied to convert the energy equation to a CDE for an enthalpy-like quantity [102,103]. For instance, with $(\rho c_p)_0$ as the reference heat capacitance, $h^* = (\rho c_p)_0 T$ was introduced in [102] and the energy equation (assuming $S_T = 0$ in Eqs. (2.1, 2.2)) was transformed to

$$\frac{\partial h^*}{\partial t} + \nabla \cdot \left(\mathbf{u} h^* \right) = \nabla \cdot \left(\frac{k}{\rho c_p} \nabla h^* \right) + S_H \tag{2.38}$$

where

$$S_H = -\frac{k}{\left(\rho c_p\right)_0} \nabla h^* \cdot \nabla \frac{1}{\sigma^*} - \frac{h^*}{\sigma^*} \mathbf{u} \cdot \nabla \sigma^*, \text{ with } \sigma^* = \frac{\rho c_p}{\left(\rho c_p\right)_0} \tag{2.39}$$

It should be noted that Eq. (2.38) was derived based on Eq. (2.2). As discussed in Section II, when the formulation of the energy equation in Eq. (2.1) is used, the second term in the expression of S_H would disappear. It was argued in [102] that the conjugate heat transfer conditions are satisfied with the above formulation. The standard LBM in Section III can be applied to the modified CDE in Eq. (2.38) if S_H is properly dealt with. Similar to that in the Group 1 schemes, the challenge for this enthalpic formulation and LBM implementation is also the approximation of the gradients $\nabla \frac{1}{\sigma^*}$ and $\nabla \sigma^*$, both related to the heat capacitance profile that experiences a jump at the interface. In [102], the following approximation, as proposed in [24] for computing the gradient of a continuous function, was applied for both $\psi = \frac{1}{\sigma^*}$ and $\psi = \sigma^*$

$$\partial_j \psi = \frac{1}{c_s^2 \delta t} \sum_\alpha \omega_\alpha \psi \left[\mathbf{x} + \left(\mathbf{e}_\alpha \cdot \mathbf{x} \right) \delta t \right] e_{\alpha j} \tag{2.40}$$

When the D2Q5 LB model is used, the above gives $\frac{\partial \psi}{\partial x_j} = \frac{\psi_{i,j+1} - \psi_{i,j-1}}{2\delta x}$. Such central-difference type approximations are second-order accurate for continuous functions, however, they would result in large errors for discontinuous or jump functions. It is expected that the interface treatment in Group 2 would give similar error behavior as that in Group 1. This will also be demonstrated in Chapter 2.5 with numerical examples.

2.4.2.3 Group 3: modified equilibrium distribution function in the LBM

Recognizing the challenge in approximating the gradient of the discontinuous heat capacitance in Groups 1 and 2, there is another group of alternative LB models [16,97–99,104–107] for conjugate heat transfer problems with modification of the microscopic equilibrium DF g_α^{eq}. Their expressions are quite similar and the main idea was incorporating the heat capacitance into g_α^{eq} so that the LBE recovers the energy equation and the diffusion coefficient is related to the thermal conductivity rather than the diffusivity as in Eq. (2.3). In such a manner, the conjugate condition with the heat flux continuity at the interface can be satisfied. We point out in this work that such a treatment is analogous to the HLD scheme and it is able to preserve the second-order accuracy only for the special situation with the straight interface located halfway in the lattice links, i.e., $\Delta = 0.5$ for all the interface nodes and with the interface parallel to one of the discrete velocity vectors. For all other cases, it degrades to a first-order scheme.

When neglecting the higher-order terms, the modified equilibrium DF in [97–99,104–107] can be written as

$$g_\alpha^{\mathrm{eq}} = \begin{cases} \left(\rho c_p\right)T - \left(\rho c_p\right)_0 T + \omega_\alpha \left(\rho c_p\right)_0 T, & (\alpha = 0) \\ \omega_\alpha \left(\rho c_p\right)T \left[\dfrac{\left(\rho c_p\right)_0}{\left(\rho c_p\right)} + \dfrac{\mathbf{e}_\alpha \cdot \mathbf{u}}{c_s^2} \right], & (\alpha = 1, 2, ..., m-1) \end{cases} \tag{2.41}$$

where $(\rho c_p)_0$ is also a constant reference heat capacitance. The standard LBE in Section III can still be used for the above modified g_α^{eq}, with the temperature in each domain obtained from $T = \sum_{\alpha=0}^{m-1} g_\alpha \Big/ \left(\rho c_p\right)$, and the relationship in Eq. (2.17) replaced by the following between the thermal conductivity and the relaxation coefficient

$$\tau_{ij} = \frac{1}{2}\delta_{ij} + \frac{\delta t}{\varepsilon_D \delta x^2} \frac{k_{ij}}{\left(\rho c_p\right)_0} \tag{2.42}$$

When the MRT-LBM is used, the modified m^{eq} in the D2Q5 model becomes

$$\mathbf{m}^{\mathrm{eq}} = \left[\rho c_p T, \rho c_p u T, \rho c_p v T, 4\rho c_p T - \frac{10}{3}\left(\rho c_p\right)_0 T, 0 \right]^{\mathrm{T}} \tag{2.43}$$

This D2Q5 MRT-LBM will be used in the next section for numerical tests. For stable computation, $(\rho c_p)_0 = 1$, and $(\rho c_p)_1 = 1$, $(\rho c_p)_2 = \sigma$ are used for $\sigma \geq 1$, and $(\rho c_p)_1 = 1/\sigma$, $(\rho c_p)_2 = 1$ are used for $\sigma \leq 1$. In addition, it will also be verified that for the Group 3 LB models, the order-of-accuracy of the LB solution can be improved from the 1st-order to 2nd-order if the geometry-considered interpolation-based interface scheme in [14,34–36,94] is implemented for $\Delta \neq 0.5$.

2.5 Numerical tests and discussion

Three tests are studied in this section to compare the numerical accuracy of the various interface schemes in Chapter 2.4. The first test is for one-dimensional (1D) diffusion in a slab consisting of two different materials. The other test case is for 2D diffusion within a circular domain of two different materials to further demonstrate the effect of interface geometry on the accuracy of the various interface schemes. All examples are at steady state and exact solutions

are available. With the focus on the comparison of the interface schemes, second-order boundary schemes in [86] for all the outer boundaries are applied for all cases. The following relative L_2-norm error is defined for the LB solution of the scalar field in the whole domain

$$E_2 = \left[\sum_{x,y} \left(\phi_{\mathrm{LBE}} - \phi_{\mathrm{ex}} \right)^2 \Big/ \sum_{x,y} \phi_{\mathrm{ex}}^2 \right]^{1/2} \tag{2.44}$$

Furthermore, the interfacial scalar value, ϕ_{int}, and interfacial flux, $q_{\mathrm{int}} = -k\,\partial\phi/\partial n$, can also be obtained from the DFs at the lattice nodes in each domain next to the interface using the evaluation schemes in [14,34]. The numerical accuracy of those interfacial quantities are valuable additional metrics to compare the performance of the interface schemes. It was verified in [14,34] that when the interpolation-based interface schemes were implemented, the interfacial scalar and flux values obtained from the different domains are exactly the same with the second-order accuracy preserved; however, when the HLD interface scheme was applied for $\Delta \neq 0.5$, only first-order accuracy is obtained for both the interfacial scalar and flux values. In this work, the evaluation schemes for Groups 1-3 can also be constructed as

$$\phi_{\mathrm{int\_1}} = \left[g_{\bar{\alpha}} \left(\boldsymbol{x}_f, t + \delta t \right) + \hat{g}_{\alpha} \left(\boldsymbol{x}_f, t \right) \right] \Big/ \varepsilon_D \,, \tag{2.45}$$

$$\phi_{\mathrm{int\_2}} = \left[g_{\alpha} \left(\boldsymbol{x}_s, t + \delta t \right) + \hat{g}_{\bar{\alpha}} \left(\boldsymbol{x}_s, t \right) \right] \Big/ \varepsilon_D \,, \tag{2.46}$$

$$q_{\mathrm{int\_1}} = -k_1\,\partial\phi_1/\partial n_1 = \left[g_{\bar{\alpha}} \left(\boldsymbol{x}_f, t + \delta t \right) - \hat{g}_{\alpha} \left(\boldsymbol{x}_f, t \right) \right] \delta x/\delta t \,, \tag{2.47}$$

$$q_{\mathrm{int\_2}} = -k_2\,\partial\phi_2/\partial n_2 = \left[g_{\alpha} \left(\boldsymbol{x}_s, t + \delta t \right) - \hat{g}_{\bar{\alpha}} \left(\boldsymbol{x}_s, t \right) \right] \delta x/\delta t \,, \tag{2.48}$$

Since the regular streaming step in Eq. (16b) is used for Groups 1-3, $g_{\bar{\alpha}} \left(\boldsymbol{x}_f, t + \delta t \right) = \hat{g}_{\bar{\alpha}} \left(\boldsymbol{x}_s, t \right)$ and $g_{\alpha} \left(\boldsymbol{x}_s, t + \delta t \right) = \hat{g}_{\alpha} \left(\boldsymbol{x}_f, t \right)$ are noted and the respective interfacial scalar and flux values obtained from the two domains in Eqs. (2.45, 2.46) and (2.47, 2.48) are also consistent, i.e., $\phi_{\mathrm{int\_1}} = \phi_{\mathrm{int\_2}}$ and $q_{\mathrm{int\_1}} = -q_{\mathrm{int\_2}}$. With the above, the following relative L_2-

norm errors for the interfacial quantities are thus defined for Groups 1-3 and the interpolation-based interface scheme in Eq. (2.21, 2.22)

$$E_{2\_\mathrm{tint}} = \left[\sum_{\mathrm{interface}} \left(\phi_{\mathrm{int\_LB}} - \phi_{\mathrm{int\_ex}} \right)^2 \Big/ \sum_{\mathrm{interface}} \phi_{\mathrm{int\_ex}}^2 \right]^{1/2}, \tag{2.49}$$

$$E_{2\_\mathrm{qint}} = \left[\sum_{\mathrm{interface}} \left(k_i \, \partial \phi_i / \partial n_i \big|_{\mathrm{LB}} - k_i \, \partial \phi_i / \partial n_i \big|_{\mathrm{ex}} \right)^2 \Big/ \sum_{\mathrm{interface}} \left(k_i \, \partial \phi_i / \partial n_i \big|_{\mathrm{ex}} \right)^2 \right]^{1/2}, (i = 1,2), \tag{2.50}$$

2.5.1 One-D diffusion in a slab of two materials

First, the incapability of the geometry-ignored interface schemes in Groups 1-3 to preserve the second-order accuracy of the LB solutions can be simply understood from the comparison of the two cases in Figure 2.1 (a) and (b). When the same outer boundary conditions are imposed for (a) and (b), each of the interface schemes in Groups 1-3 would give the same LB solutions for the two cases as they do not consider the actual location of the interface within the link. However, the exact solutions for these two cases are clearly different (the difference is of the first-order of the grid spacing). Thus, the interface schemes in Groups 1-3 can at most preserve the first-order accuracy for $\Delta \neq 0.5$ at the interface.

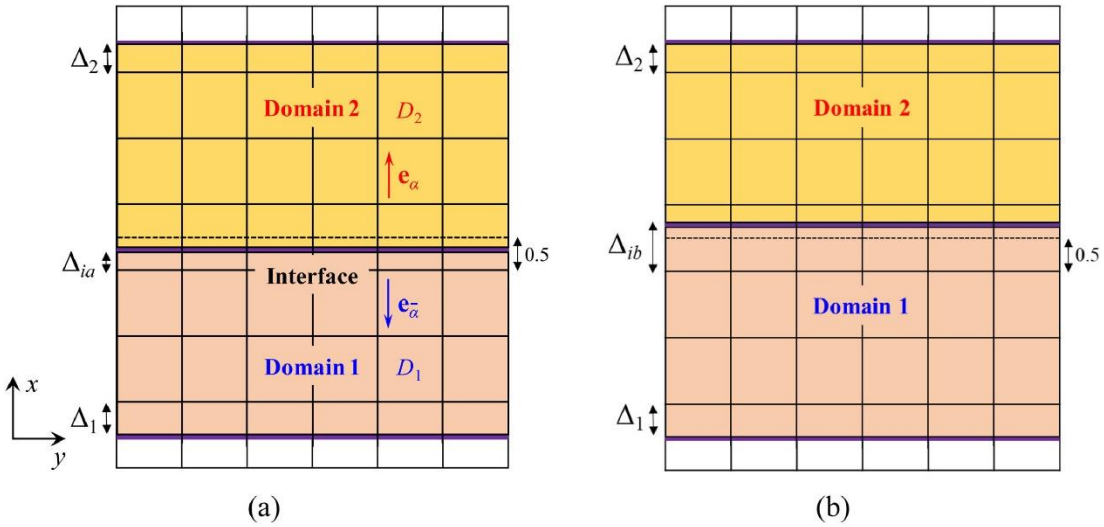

Figure 2.1 Schematic depiction of the lattice for 1D diffusion in a two-solid slab with the intersection link fraction at the interface (a) $\Delta_{ia} < 0.5$, and (b) $\Delta_{ib} > 0.5$.

Specifically, one can consider the simplest steady-state test with $\phi(x = 0) = 0$, $\phi(x = L) = 1$, $\Delta_1 = \Delta_2 = 0.5$, and $\sigma = 1$ so that Groups 1-3 all reduce to the simplified HLD scheme in Eq. (2.32, 2.33). The comparison of both the LB solutions from using the HLD scheme and the geometry considered interpolation-based scheme in [14] (see Eq. (2.21, 2.22)) with the exact solutions is shown in Figure 2.2, where very coarse grid ($L = 8\delta x$) was used and the other simulation parameters are $\tau_1 = 0.55$, $\tau_2 = 1.0$ ($k_2/k_1 = D_2/D_1 = 10$), $\Delta_{ia} = 0.01$, and $\Delta_{ib} = 0.99$. Excellent agreement is observed between the LB solutions using the interface scheme in [14] and the exact solution; while the solutions based on the HLD scheme for $\Delta_{ia} = 0.01$ and $\Delta_{ib} = 0.99$ are irresponsive to the variation of the exact solutions due to the interface location change, and large discrepancy between the LB solution and the exact solution is noticed. The first-order convergence for the HLD scheme is clearly seen in Figure 2.3 for the interior field and Figure 2.4 for the interfacial scalar and flux values. It is worth noting that for this linear diffusion problem, the LB solution based on the interface scheme in Eq. (2.21, 2.22) and all three

boundary schemes in Eq. (2.27-2.29) is almost exact for all Δ values at the interface and the outer boundaries, with machine epsilon errors achieved in the present numerical test.

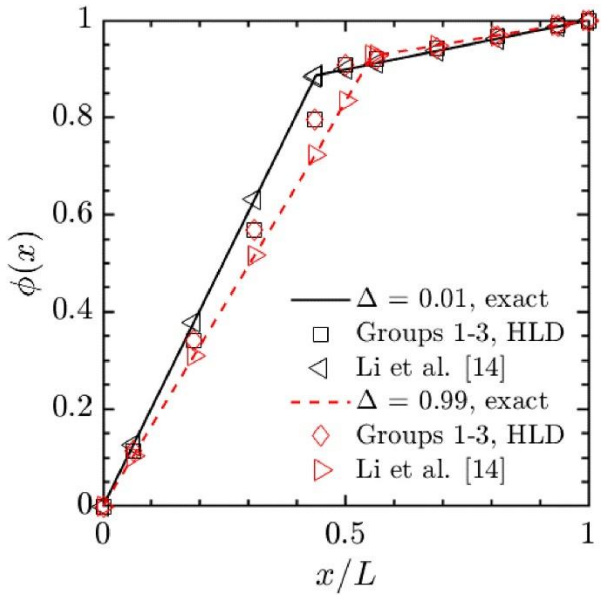

Figure 2.2 Profiles of the scalar variable ϕ(x) for the 1D diffusion problem in Fig. 2.1 with σ = 1.

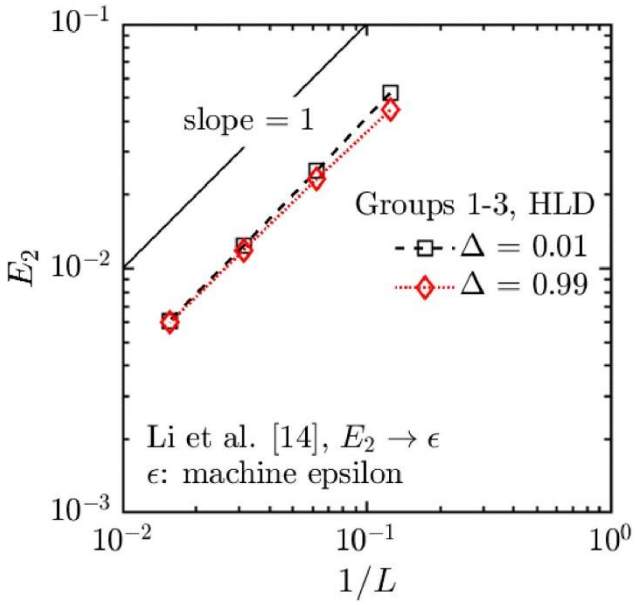

Figure 2.3 Relative L_2 norm error, E_2, for the interior scalar field versus the grid resolution, $1/L$, for the 1D diffusion problem.

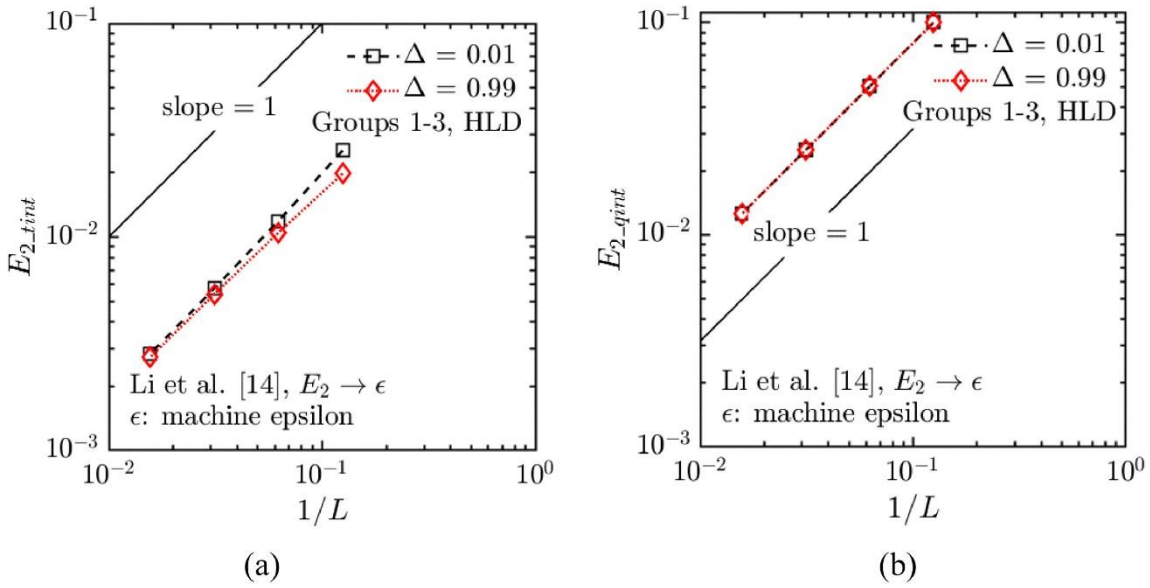

Figure 2.4 Relative L_2 norm errors, (a) E_{2_tint}, for the interfacial scalar, and (b) E_{2_qint}, for the interfacial flux, versus $1/L$ for the 1D diffusion problem.

Next, we consider the cases with $\sigma = \dfrac{(\rho c_p)_2}{(\rho c_p)_1} = \dfrac{k_2/k_1}{D_2/D_1} = \dfrac{k_{21}}{D_{21}} \neq 1$ to compare the performance of the various interface schemes in Groups 1-3. For brevity, the boundary and interface link fractions are all fixed at $\Delta = 0.5$ and the two adjacent domains with different materials are assumed to have the same length so that the exact solution is fixed. Since $\sigma \neq 1$ is applied, and also with different boundary conditions $\phi(x = 0) = 0$ and $\phi(x = L) = 1$, the present solution as shown below is slightly different from that in [34] for the same heat source $G_{T,i}(x) = D_i S(x) = D_i \left[\dfrac{12a}{L^2}\left(\dfrac{x}{L}\right)^2 + \dfrac{6b}{L^2}\left(\dfrac{x}{L}\right) + \dfrac{2c}{L^2} \right]$ applied

$$\phi_{1,\text{ex}} = -\left[a(x/L)^4 + b(x/L)^3 + c(x/L)^2 \right] + \lambda_1 x, \tag{2.51}$$

$$\phi_{2,\text{ex}} = -\left[a(x/L)^4 + b(x/L)^3 + c(x/L)^2 \right] + \lambda_2 x + \lambda_3, \tag{2.52}$$

where

$$\lambda_1 = \frac{(2a+3b+4c)+k_{21}(6a+5b+4c+8)}{4L(1+k_{21})}, \tag{2.53}$$

$$\lambda_2 = \frac{(6a+5b+4c+8)+k_{21}(2a+3b+4c)}{4L(1+k_{21})}, \tag{2.54}$$

$$\lambda_3 = \frac{(k_{21}-1)(2a+b+4)}{4L(1+k_{21})}, \tag{2.55}$$

Figures 2.5 and 2.6 show the scalar ϕ profiles with the different interface schemes implemented for varying heat capacitance ratio and diffusivity ratio, respectively, where in Figures 2.5b and 2.6b a quadratic source term with $a = 1$ and $b = c = 0$ in Eq. (2.51, 2.52) is applied. It is observed that the results using the interface schemes from Group 3 and Li et al. [14] match the exact solutions extremely well for all cases, close examination of the data for these two schemes at $\Delta = 0.5$ reveals that their LB solutions are almost identical, with very slight difference noticed only at large heat capacitance ratios (e.g., when $\sigma = 0.2$). Furthermore, both Group 1 and Group 2 yield large errors, especially when σ is far away from 1, e.g., with $\sigma = 0.2$ and 5; of these two schemes, Group 1 shows larger errors in Figure 2.6 and Group 2 has larger errors in Figure 2.5. Only when σ is very close to 1 ($\sigma = 0.99$ in Figure 2.5) Groups 1 and 2 are able to match the exact solutions. The finite-difference type approximation of the discontinuous heat capacitance gradient at the lattice nodes next to the interface in Groups 1 and 2 are the main reason for their large errors in this 1D diffusion problem. In the next test, more detailed error analysis will be presented for a 2D convection-diffusion problem.

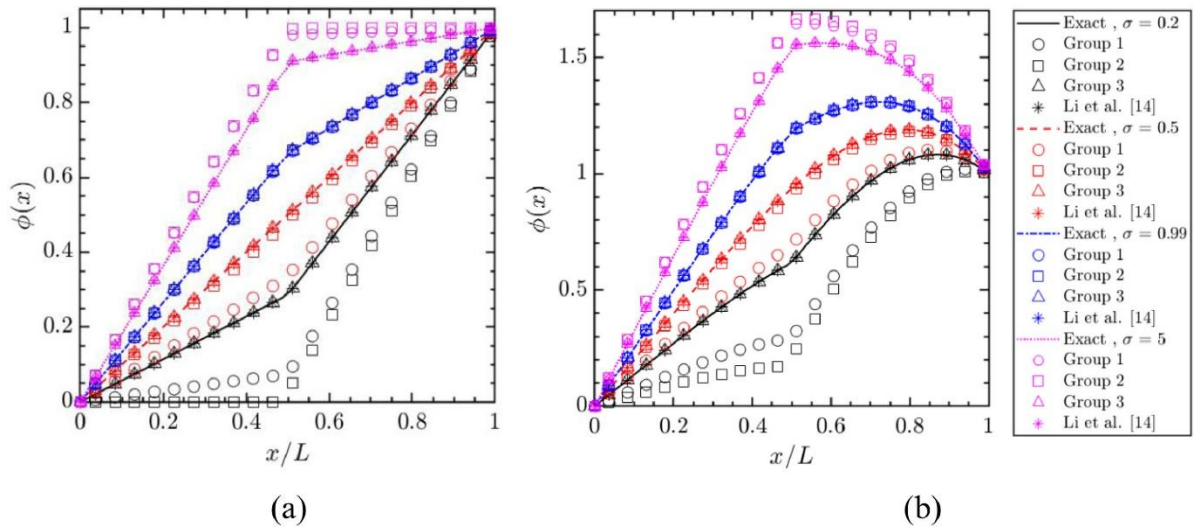

(a) (b)

Figure 2.5 Profiles of the scalar variable ϕ(x) for the 1D diffusion problem with different σ values and a fixed diffusivity ratio D_{21} = 2: (a) without heat source, and (b) with a quadratic source.

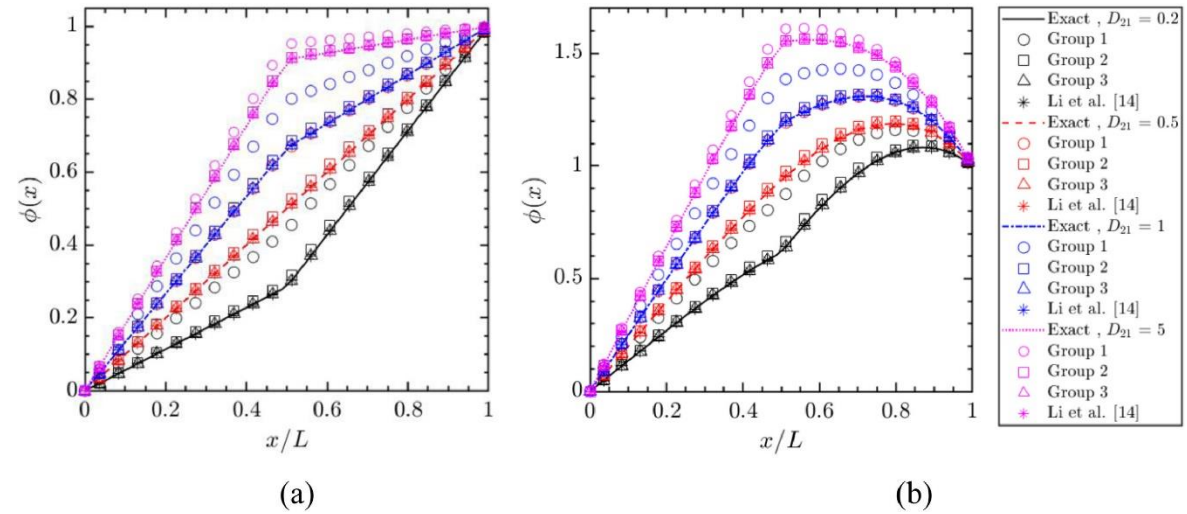

(a) (b)

Figure 2.6 Profiles of the scalar variable ϕ(x) for the 1D diffusion problem with different diffusivity ratios D_{21} and a fixed σ = 2: (a) without heat source, and (b) with a quadratic source.

2.5.2 Two-D diffusion in a circular domain

In this test, scalar diffusion in a circular domain of two different materials is simulated to verify the effect of curved geometry on the accuracy of the various interface schemes. The computational domain is illustrated in Figure 2.7 following [14]. The same exact solution given in [14] for the case with an outer boundary condition $\phi_2(r = R_2) = \cos(4\theta)$ and the standard conjugate conditions at the interface ($r = R_1$) is used here while $\sigma \neq 1$ is applied. The procedures for implementation of the interface schemes in Groups 1-3 and the coupled scheme in [14] are the same as those in the previous test for the inclined interface. In addition, an improved Group 3 scheme which combines the modified equilibrium DFs in Group 3 and the coupled interface scheme in [14] is also included for comparison.

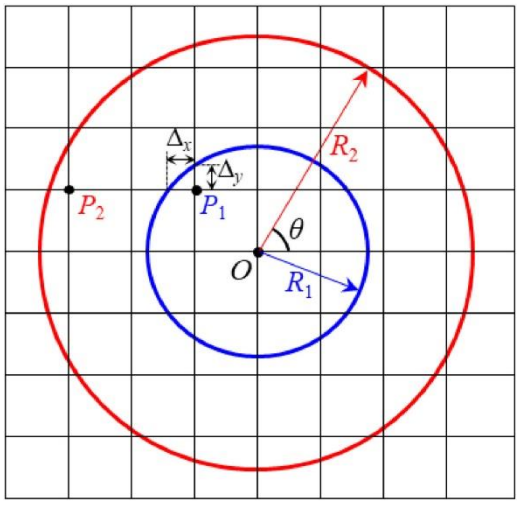

Figure 2.7 Schematic depiction of the lattice in a circular domain for 2D conjugate scalar diffusion.

Using the parameters $\sigma = 2$, $D_{21} = 5$, $(\tau_1, \tau_2) = (0.55, 1.0)$ for the Group 3 and improved Group 3 schemes and $(\tau_1, \tau_2) = (0.55, 0.75)$ for the other schemes, the results for E_2, E_{2_tint}, and E_{2_qint} are

shown in Figures 2.8 and 2.9 (a, b), respectively. For the cases where the interpolation-based schemes are applied, the particular Scheme 2 in Eq. (2.28) for the coefficient c_{d1} is used.

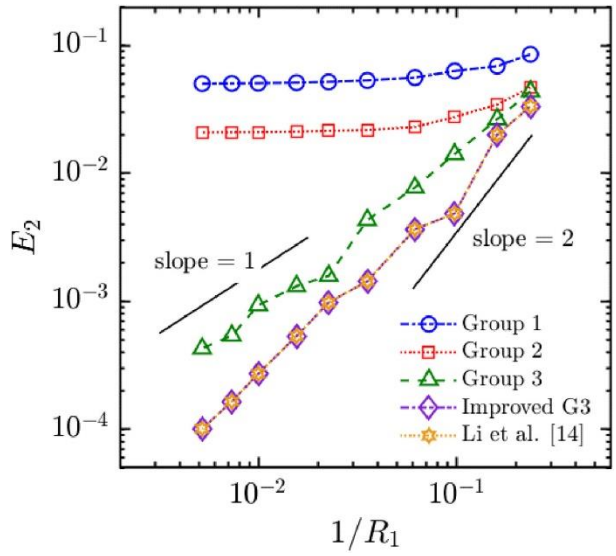

Figure 2.8 Relative L_2 norm error, E_2, for the interior scalar field versus the grid resolution, $1/R_1$, for the 2D diffusion in a circular domain.

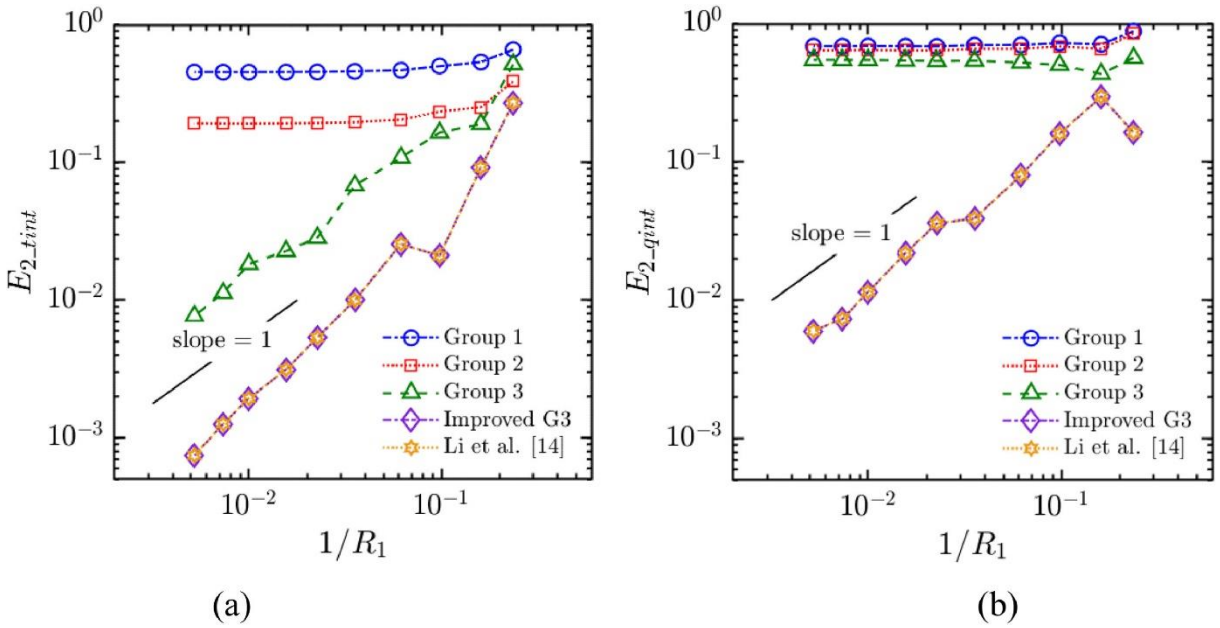

Figure 2.9 Relative L_2 norm errors, (a) E_{2_tint}, for the interfacial scalar, and (b) E_{2_qint}, for the interfacial flux, versus $1/R_1$ for the 2D diffusion in a circular domain.

As expected, zeroth-order accuracy is observed for all three quantities of interest for Groups 1 and 2. The original Group 3 scheme yields first-order convergence for the interior and interfacial scalar values and zeroth-order for the interfacial flux. For both the improved Group 3 scheme and the coupled scheme in [14], near second-order convergence at low resolution and eventually first-order convergence at high resolution are obtained for all three quantities, which is consistent with that reported in [14,34]. It is also noticed that the results from using these two geometry-considered interface schemes are almost identical, which is consistent with that observed in Figures 2.5 and 2.6 for the 1D diffusion problem. Lastly, it should be emphasized that even though the same first-order convergence rate is obtained for the original Group 3 and the two coupled schemes for the interior and interfacial scalar values in Figures 2.8 and 2.9a, the

error magnitude for the cases with coupled interface schemes is much lower than that for the geometry-ignored Group 3 scheme.

2.6 Conclusions

A detailed comparison with theoretical analysis and numerical tests was conducted for the popular interface schemes for conjugate heat and mass transfer modeling using the lattice Boltzmann method (LBM). The various interface schemes considered include the second-order accurate interpolation-based treatments in [14,34–36,94] that consider the interface geometry and arrangement in the lattice, and several modified schemes that bypass the local geometry and topology consideration by utilizing other corrections, such as adding source terms (Group 1), reformulating the transport problem with an alternative governing equation for an enthalpy-like quantity (Group 2), and using modified equilibrium distribution functions in the LB model (Group 3). While the Group 3 scheme can be considered an alternative for the first-order accurate "half-lattice-division" (HLD) scheme discussed in [14], Groups 1 and 2 require approximation of the heat capacitance gradient at the interface to account for the heat flux continuity for conjugate heat transfer problems. The gradient approximation in Groups 1 and 2 results in persistent numerical errors even for the simple cases with constant yet different heat capacitances in different materials as the gradient of a discontinuous function is encountered. Compared to the second-order accuracy obtained in [14] for straight parallel interfaces located in arbitrary locations in the lattice, both the analysis and numerical tests confirm that without considering the local geometry and topology at the interface, the accuracy of the LB results with the modified schemes in Groups 1–3 is at most of the first-order for general cases. More importantly, while the Group 3 scheme can be improved to preserve second-order accuracy by also including the interpolation-based interface scheme, Groups 1 and 2 always yield zeroth-

order accuracy at moderate to high resolution due to the discontinuity effect in the heat capacitance gradient approximation, and there is no convenient approach to improve that. When the various sharp interface schemes are applied to more complex situations involving curved interfaces, the effect of the interface geometry on the accuracy of the LB results becomes more obvious. In particular, the interpolation-based interface schemes, including that proposed in [14] and the improved Group 3, are capable of retaining first-order accuracy; and their error magnitude is also much smaller than that obtained from using the basic Group 3 scheme; however, the schemes in Groups 1 and 2 always yield zeroth-order accurate results with large error magnitude.

CHAPTER III

PREDICTION OF EFFECTIVE THERMAL CONDUCTIVITY OF POROUS LATTICE STRUCTURES AND VALIDATION WITH ADDITIVELY MANUFACTURED METAL FOAMS*

After examining the accuracy of various sharp interface schemes, this Chapter focuses on developing an accurate lattice Boltzmann method (LBM) model and convenient correlation for effective thermal conductivity (ETC) of four periodic unit cell topologies, viz. Cube, FD-Cube, TKD and Octet, over the entire range of porosities $0 \leqslant \varepsilon \leqslant 1.0$. Since the Cube and Octet demonstrate the simplest and most complex fiber network, respectively, these four structures were deliberately chosen for investigating the ETC of cellular lattices of various topologies and over a wide range of porosities. The correlations for the ETC of different unit cell topologies are proposed with critical discussion on the porosity range in which each of them is valid. The ETC predictions of those structures at high porosities $\varepsilon > 0.9$ are consistent with published experimental and theoretical/computational data, while those at lower porosities $\varepsilon < 0.9$ are validated with our in-house experimental data as well as with the available reported data in the recent literature. The correlations developed for the normalized ETC, k_{eff}/k_s, based on the high-fidelity LB simulations are simple 2nd-order polynomials as a function of the porosity only for each unit cell topology, thus they are extremely convenient to use for future metal foams design

* Part of this chapter is based on work published in Applied Thermal Engineering in 2021 [111]

and innovation with different materials and structures.

The remaining of this chapter is organized as follows: Chapter 3.2 illustrates the topologies of the four different porous lattice structures. Chapter 3.3 introduces the experimental setup for measuring the ETC of those structures. The details of the LB-based numerical method and model verification are provided in 3.4 Numerical method, 3.5 Model verification, respectively. Chapter 3.6 presents and discusses the present experimental data and the computational results for the ETC of those structures of interest, where the comparison and validation of the computational results as well as the ETC correlations are given in detail. And conclusions are summarized in Chapter 3.7.

3.1 Introduction

The feasibility and attractiveness of using the lattice Boltzmann method (LBM) to simulate conjugate heat transfer and predict the ETC of porous media have been demonstrated in previous studies (e.g., [15,112,113]) with the advantages of simple and explicit algorithm and convenience in boundary condition treatment with complex geometry in the LBM. As demonstrated in [113] with the LBM and an effective interface scheme, a $50 \times 50 \times 50$ grid was sufficient to represent the complex random open-cell porous foams and obtain the ETC. Moreover, with effective interface treatments as in [14,34,89], for conjugate heat and mass transfer problems using the LBM, the conjugate interface conditions are satisfied up to 2^{nd}-order accuracy during each time step without iterations. However, the LB models proposed in the previous studies still suffer numerical instability and degraded accuracy when simulating transport between materials or phases with very high transport property ratios (e.g., the thermal conductivity ratio of the most extensively studied aluminum-air pair with $k_s/k_f = 8303$). Specifically, the relaxation coefficient, τ, in the LB model is directly related to the diffusion

coefficient and the magnitude of τ has a significant effect on both the numerical stability and accuracy [14,86,110]: the typical τ values are chosen within the range of (0.5, 2.0), and large numerical errors are expected when τ is close to or >2.0, while numerical stability becomes an issue when τ is very close to 0.5. This poses a practical dilemma in choosing τ_s and τ_f to satisfy $(\tau_s - 0.5)/(\tau_f - 0.5) = k_s/k_f$ when k_s/k_f is extremely large. In this paper, we propose a novel interface scheme to tackle this problem by decoupling the relaxation coefficients τ_s and τ_f in the LB model while satisfying the conjugate conditions (details given Chapter 3.4.3). Hence the LB model is very efficient in computationally determine the ETC of various structures with large property ratios.

3.2 Configurations of porous lattice structures

In this chapter, four types of porous structures are considered in the open-cell metal foams family with Cube, face diagonal (FD)-Cube, Tetrakaidecahedron (TKD), and Octet unit lattice, as shown in Fig. 3.1. The Cube and FD-Cube are the simplest 3D structures. The TKD structure has been extensively studied in the literature and is considered the basic structure for most commercial metal foams typically made from foaming process [114], [115], [116]. The Octet structure has recently attracted great interest and seen promising applications in developing lightweight high-strength structures [117], [118], [119] and multi-functional heat sinks where a robust mechanical performance in addition to heat dissipation is required [65], [66], [120], [121].

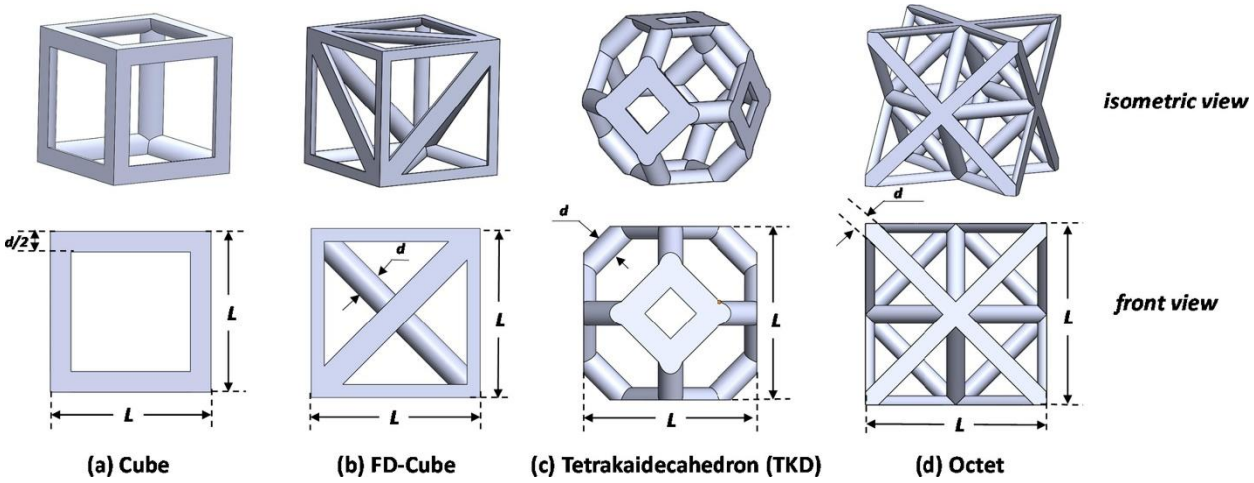

Figure 3.1 Geometry of the periodic unit cells of the porous (a) Cube, (b) FD-Cube, (c) TKD, and (d) Octet structures.

It should be noted that all 4 structures in Figure 3.1 are designed for convenient additive manufacturing processes: all fibers in each cell are of the same size with a cylindrical shape, and the porosity of the structures can be conveniently controlled by varying the unit cell length L and the fiber diameter d. In particular, the TKD structure in Figure 3.1 is constructed in an "additive" manner that is different from the traditional TKD structures obtained through "subtractive" procedures [122], [123], [124], [125], where the strand (fiber) thickness could become extremely small. It is clear in Figure 3.1 that all four unit cells are periodic in geometry along the three main axis directions [1, 0, 0], [0, 1, 0] and [0, 0, 1]. It should also be mentioned that thermal hysteresis and convection are not considered in this study for the ETC prediction, and the magnitude of the temperature on each surface and their difference are not very high. With those assumptions, the ETC in each of the three axis directions is the same for each structure shown in Figure 3.1.

3.3 Experimental setup

The ETC of porous blocks made from Octet and TKD unit cells were measured from steady-state heat transfer experiments. The experimental setup is shown in Figure 3.2 and the samples are shown in Figure 3.3. The samples were first insulated from the four faces to minimize the heat loss. Further, a patch heater was glued on the top face of the sample and Styrofoam insulation was glued on the backside of the patch heater as well. This assembly was attached to a copper slab which was placed such that it was partially submerged in the chilled thermal reservoir with the help of a pair of supporting legs. Copper slab of 25.4 mm thickness and 100 mm × 100 mm was chosen due to its marked high thermal mass. The thermal reservoir held the ice-water slurry for the duration of heat transfer experiments. Water in the reservoir was periodically circulated to mix the heat transferred from the copper slab. Such an experiment is desired to maintain an effectively 1D heat transfer along the thickness of the porous block.

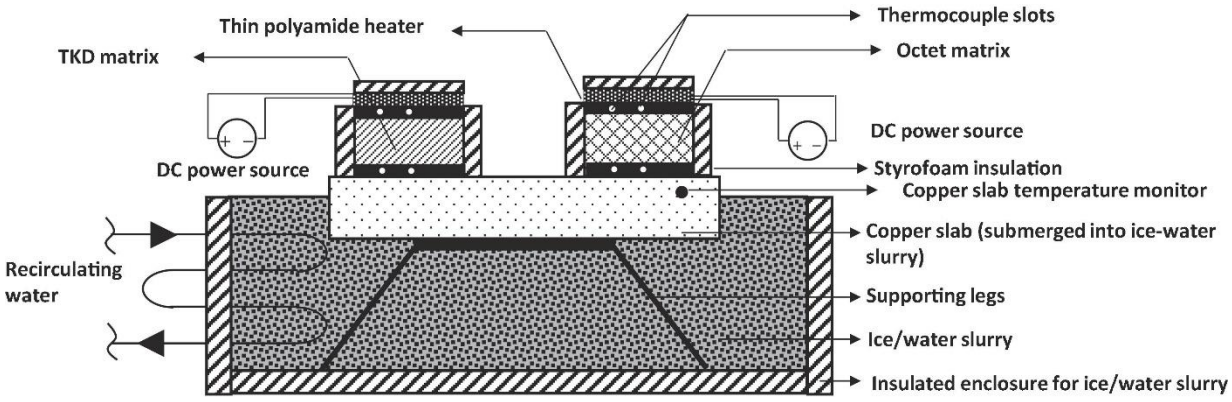

Figure 3.2 Experimental setup for k_{eff} determination.

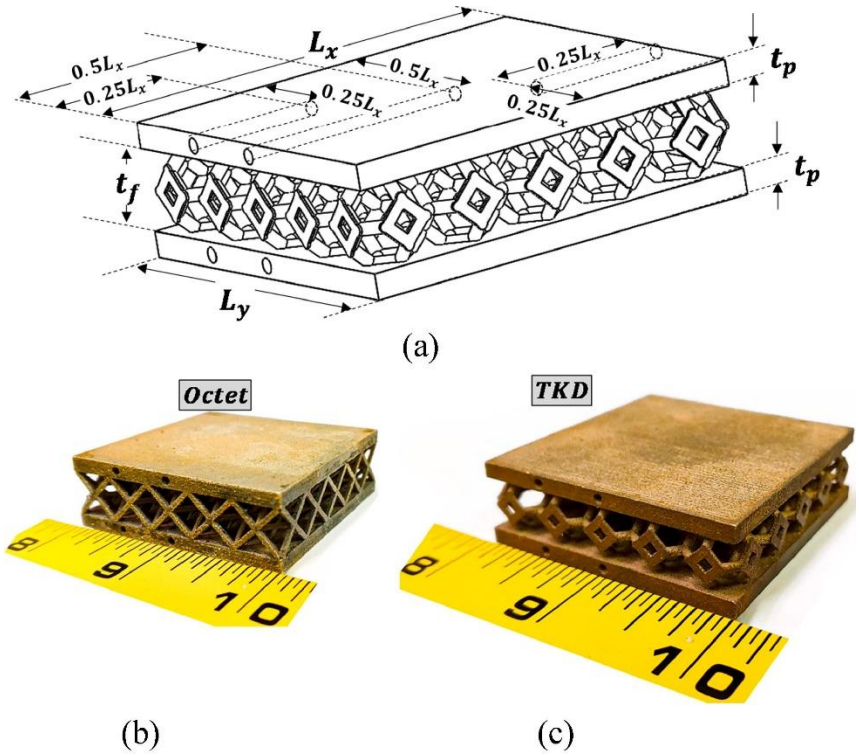

Figure 3.3 (a) Depiction of the TKD sample for k_{eff} experiments with thermocouple locations, and illustration of the (b) Octet and (c) TKD test samples.

The 3D printed porous block comprised of top and bottom plates, each of thickness 3.175 mm, between which an array of 5 × 5 unit cells was placed. The unit cells were an integral component of the top and bottom plates with zero thermal contact resistance. This is a requirement for accurate measurement of k_{eff} of the porous samples. Both Octet and TKD samples were tested together under the same thermal boundary conditions. Heat transfer experiments were carried out at three different heat flux inputs from a DC power source. The top and bottom plates of the porous blocks featured slots for thermocouple measurements and the respective locations are shown in Figure 3.3a; also, both the Octet and TKD test samples are presented in Figures 3.3b and 3.3c, respectively.

The ETC was calculated using Eq. (3.1),

$$k_{eff} = \frac{(q_{total} - \sum q_{loss})t_f}{A_b(T_{top} - T_{bottom})}, \tag{3.1}$$

where q_{total} is the total heat supplied by patch heater, $\sum q_{loss}$ is the total heat lost from the four side faces and the top face, $\tilde{T}_{top}$ and $\tilde{T}_{bottom}$ are the average temperatures at the top and bottom plates, A_b is the cross-sectional area through which heat is being transferred, and t_f is the thickness of the unit cell.

The total heat supplied was measured through the current output in the DC power source and the resistance across the patch heater measured via. a multimeter ($q_{total} = i^2 R_{htr}$). The heat loss through each face was calculated by measuring the temperature difference between the inner and outer sides of the Styrofoam insulations ($q_{loss} = k_{ins} A_{ins}(T_{ins,in} - T_{ins,out})/t_{ins}$). Separate experiments were conducted for the measurement of solid-phase thermal conductivity. The principle was same as the one described above, where a sample of dimensions 25.4 mm × 25.4 mm × 50.8 mm was additively manufactured through the same process as the porous blocks. The k_{eff} results are presented in normalized form of k_{eff}/k_s. The porosity of each sample was determined using $\varepsilon = 1 - (m_s/\rho_s)/\forall_{total}$, where m_s is the mass of the porous structure (excluding the mass of top and bottom plates) which was measured by a chemical balance, ρ_s is the density of solid which was determined by the mass and volume measurement of the 3D printed solid block mentioned above, and $\forall_{total}$ is the total volume between the top and bottom plates.

3.4 Numerical method

In this Chapter, the D3Q7 LB model [85], [86], [87] is applied to simulate the conjugate heat transfer within the porous lattice structures. In particular, a novel decoupled interface

treatment that is suitable for transport simulation between materials and phase of very large property ratios is proposed. For completeness, the LB model and boundary schemes are briefly reviewed, then followed by the explanation of the proposed interface scheme and the efficient ETC evaluation within the LBM framework.

3.4.1 Lattice Boltzmann model

To numerically predict the ETC, the heat conduction through the porous structures is simulated. The conjugate conditions at the interface without temperature or flux jumps can be expressed as

$$\phi_f = \phi_s , \tag{3.2}$$

$$-k_f \frac{\partial \phi_f}{\partial n_f} = k_s \frac{\partial \phi_s}{\partial n_s} , \tag{3.3}$$

where ϕ is the scalar variable of temperature, k is the thermal conductivity, n represents the outward normal direction, and the subscripts f and s denote the fluid and solid phases, respectively.

The multiple-relaxation-time (MRT) D3Q7 LB model [14,122,123] is applied to simulate the 3D heat conduction, for which the evolution equation of the microscopic distribution functions (DFs) is written as

$$g_\alpha(\mathbf{x}+\mathbf{e}_\alpha \delta t, t+\delta t) - g_\alpha(\mathbf{x},t) = -[\mathbf{M}^{-1}\mathbf{S}(\mathbf{m}(\mathbf{x},t) - \mathbf{m}^{(\mathrm{eq})}(\mathbf{x},t))]_\alpha + \omega_\alpha G \delta t , \tag{3.4}$$

where the DF $g_\alpha(\mathbf{x}, t) \equiv g(\mathbf{x}, \xi_\alpha, t)$, $\mathbf{x}$ is the special vector, $\boldsymbol{\xi}$ is the particle velocity vector discretized to a small set of discrete velocities $\{\xi_\alpha | \alpha = 0, 1, \ldots, m-1\}$, δt is the time step, G is the source term, the discrete velocity set is defined as

$$\mathbf{e}_\alpha = \begin{cases} (0,0,0) & (\alpha = 0), \\ (\pm 1,0,0),(0,\pm 1,0)(0,0,\pm 1), & (\alpha = 1,2,3,4,5,6), \end{cases} \tag{3.5}$$

the weight coefficients ω_α are

$$\omega_\alpha = \begin{cases} 1/4, & (\alpha = 0), \\ 1/8, & (\alpha = 1,2,3,4,5,6), \end{cases}, \tag{3.6}$$

and the equilibrium moments $\mathbf{m}^{\text{eq}}$ are

$$\mathbf{m}^{\text{eq}} = \left(0, u\phi, v\phi, w\phi, a\phi, 0, 0\right)^T, \tag{3.7}$$

where *u*, *v*, and *w* are the macroscopic velocity components that can be set to zero for pure conduction, and *a* is a constant related to the weight coefficients with $a = 7(\omega_0 - 1) = \frac{3}{4}$.

In Eq. (3.4), the transformation matrix **M** relates the DFs $g_\alpha(\mathbf{x}, t)$ to their moments $m_\alpha(\mathbf{x}, t)$, $\mathbf{m} = \mathbf{Mg}$, and **S** is the relaxation matrix in which the relaxation coefficients τ_{ij} are related to the diffusion coefficient as

$$\tau_{ij} = \frac{1}{2}\delta_{ij} + \frac{\delta t}{\varepsilon_D \delta x^2} k_{ij}, \tag{3.8}$$

where δ_{ij} is the Kronecker delta, and the constant $\varepsilon_D = \frac{1}{4}$ in D3Q7. The detailed matrices **M** and **S** for the D3Q7 LB model can be found in [86,126].

For efficient computations, the evolution equation (3.4) is usually solved in two consecutive steps:

Collision step:

$$\hat{g}_\alpha(\mathbf{x}, t) = g_\alpha(\mathbf{x}, t) - [\mathbf{M}^{-1}\mathbf{S}(\mathbf{m}(\mathbf{x}, t) - \mathbf{m}^{(\text{eq})}(\mathbf{x}, t))]_\alpha + \omega_\alpha G \delta t, \tag{3.9}$$

Streaming step:

$$g_\alpha(\mathbf{x} + \mathbf{e}_\alpha \delta t, t + \delta t) = \hat{g}_\alpha(\mathbf{x}, t), \tag{3.10}$$

where $\hat{g}_\alpha$ is the post-collision state.

3.4.2 Boundary schemes

In the LB model for scalar convection-diffusion such as the heat conduction in this work, the given physical boundary conditions including prescribed temperature (Dirichlet condition

$\phi = \Phi_d$) and heat flux (Neumann condition $-k\dfrac{\partial \phi}{\partial n} = \Phi_n$) can be conveniently converted to corresponding boundary conditions for the DFs. Following [86] the general boundary schemes are

$$g_{\bar{\alpha}}\left(\mathbf{x}_f, t+\delta t\right) = c_{d1}\hat{g}_{\alpha}\left(\mathbf{x}_f, t\right) + c_{d2}\hat{g}_{\alpha}\left(\mathbf{x}_{ff}, t\right) + c_{d3}\hat{g}_{\bar{\alpha}}\left(\mathbf{x}_f, t\right) + c_{d4}\varepsilon_D\Phi_d, \tag{3.11}$$

$$g_{\bar{\alpha}}\left(\mathbf{x}_f, t+\delta t\right) = c_{n1}\hat{g}_{\alpha}\left(\mathbf{x}_f, t\right) + c_{n2}\hat{g}_{\alpha}\left(\mathbf{x}_{ff}, t\right) + c_{n3}\hat{g}_{\bar{\alpha}}\left(\mathbf{x}_f, t\right) + c_{n4}\left(\delta t/\delta x\right)\Phi_{n\bar{\alpha}}, \tag{3.12}$$

where c_{di} and c_{ni} ($i = 1 \sim 4$) are coefficients related to the local intersection link Δ denoted by $\Delta = ||\mathbf{x}_f - \mathbf{x}_w|| / ||\mathbf{x}_f - \mathbf{x}_e||$ with $0 \le \Delta < 1$, $\mathbf{x}_w$ the boundary node, $\mathbf{x}_e$ the exterior node, $\mathbf{x}_f$ and $\mathbf{x}_{ff}$ the respective first and second interior nodes in the lattice structure, and $\Phi_{n\bar{\alpha}}$ is the flux component in the lattice velocity direction (see Figure 3.4a).

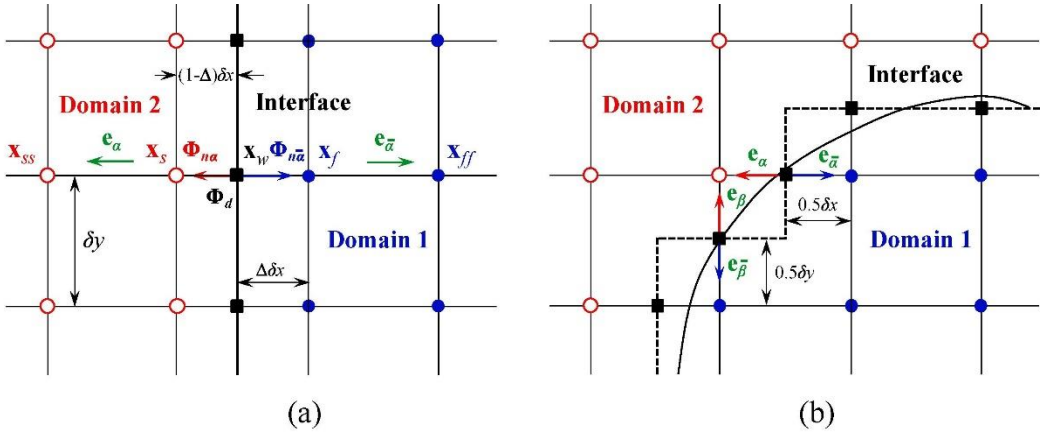

Figure 3.4 Illustrations of the (a) straight and (b) curved interface geometry in the lattice (solid circles, lattice nodes in Domain 1; solid squares, interface nodes; open circles, lattice nodes in Domain 2). In (b), the curved interface (solid curve) is approximated as zigzagged segments (dashed line) with intersection links all at $\Delta = 0.5$.

It was shown in [86] that the second-order scheme in Eq. (3.12) for the Neumann condition is unique, while for the Dirichlet condition, there is an adjustable parameter in Eq.

(3.11). Here we use the Scheme 3 in [86] for the Dirichlet condition; and the explicit boundary schemes become

$$g_{\bar{\alpha}}\left(\mathbf{x}_f, t+\delta t\right) = -\hat{g}_{\alpha}\left(\mathbf{x}_f, t\right) + \left(\frac{2\Delta-1}{2\Delta+1}\right)\hat{g}_{\alpha}\left(\mathbf{x}_{ff}, t\right) + \left(\frac{2\Delta-1}{2\Delta+1}\right)\hat{g}_{\bar{\alpha}}\left(\mathbf{x}_f, t\right) + \left(\frac{2}{2\Delta+1}\right)\varepsilon_D \Phi_d, \quad (3.13)$$

$$g_{\bar{\alpha}}\left(\mathbf{x}_f, t+\delta t\right) = \hat{g}_{\alpha}\left(\mathbf{x}_f, t\right) - \left(\frac{2\Delta-1}{2\Delta+1}\right)\hat{g}_{\alpha}\left(\mathbf{x}_{ff}, t\right) + \left(\frac{2\Delta-1}{2\Delta+1}\right)\hat{g}_{\bar{\alpha}}\left(\mathbf{x}_f, t\right) + \left(\frac{2}{2\Delta+1}\right)\frac{\delta t}{\delta x}\Phi_{n\bar{\alpha}}. \quad (3.14)$$

3.4.3 Decoupled interface scheme

Various interface schemes have been proposed in the literature and their applicability and accuracy have been verified for conjugate heat and mass transfer with the LB method (see [14,34,89] and refs therein). The improved interface scheme proposed in this work is particularly attractive and powerful in modeling heat and mass transfer between domains with very large transport property ratios. For brevity, we consider here the cases with either straight interface geometry (see Figure 3.4a) or approximated zigzagged interface geometry for curved interfaces (Figure 3.4b). When $\Delta = 0.5$ was chosen for all the interface nodes, the "half-lattice division" (HLD) scheme [14,112] becomes

$$g_{\bar{\alpha}}\left(\mathbf{x}_f, t+\delta t\right) = \hat{g}_{\bar{\alpha}}\left(\mathbf{x}_s, t\right), \quad (3.15)$$

$$g_{\alpha}\left(\mathbf{x}_s, t+\delta t\right) = \hat{g}_{\alpha}\left(\mathbf{x}_f, t\right) \quad (3.16)$$

It should be noted that for the above HLD scheme to satisfy the conjugate conditions, the relaxation coefficients in the two domains must follow the relationship

$$\frac{2\tau_2 - 1}{2\tau_1 - 1} = \frac{k_s}{k_f}, \text{ or} \quad (3.17)$$

$$\tau_2 = \left(\tau_1 - 0.5\right)\frac{k_s}{k_f} + 0.5. \quad (3.18)$$

Only isotropic diffusion is considered here in both domains for brevity to yield Eq. (3.17, 3.18) (see Eq. (3.8)). The relationship in Eq. (3.17, 3.18) clearly shows that only one of the relaxation coefficients can be selected as adjustable, and the other is determined accordingly for given domain properties [124]. This poses a critical challenge when simulating conjugate heat and mass transfer between materials or phases of very large property ratios. Following the idea in [124], where two different time scales were introduced for the adjacent domains, we introduce here a decoupling scaling factor, λ, for the two relaxation coefficients,

$$\lambda \frac{2\tau_{2\lambda}-1}{2\tau_1-1}=\frac{k_s}{k_f}, \text{ or} \tag{3.19}$$

$$\tau_{2\lambda}=\left(\tau_1-0.5\right)\frac{1}{\lambda}\frac{k_s}{k_f}+0.5=\left(\tau_1-0.5\right)\frac{k_{s\lambda}}{k_f}+0.5\,. \tag{3.20}$$

Comparing Eq. (3.20) with (3.18), one can clearly see that the choice of the relaxation coefficient, $\tau_{2\lambda}$, in Domain 2 becomes adjustable by selecting different λ values. Appropriate λ values can be chosen such that both τ_1 and $\tau_{2\lambda}$ will satisfy the stability and accuracy requirements. This will be verified with numerical tests in Chapter 3.5.

With the rescaled $\tau_{2\lambda}$ in Eq. (3.20), the flux continuity at the interface in Eq. (3.3) can be rewritten as

$$\Phi_{n1}=-k_f\frac{\partial\phi_f}{\partial n_f}=\lambda k_{s\lambda}\frac{\partial\phi_s}{\partial n_s}=-\lambda\Phi_{n2} \tag{3.21}$$

to derive the present decoupled HLD interface scheme

$$g_{\bar{\alpha}}(\mathbf{x}_f,t+\delta t)=(\frac{1-\lambda}{1+\lambda})\hat{g}_{\alpha}(\mathbf{x}_f,t)+(\frac{2\lambda}{1+\lambda})\hat{g}_{\bar{\alpha}}(\mathbf{x}_s,t)\,, \tag{3.22}$$

$$g_{\alpha}(\mathbf{x}_s,t+\delta t)=-(\frac{1-\lambda}{1+\lambda})\hat{g}_{\bar{\alpha}}(\mathbf{x}_s,t)+(\frac{2}{1+\lambda})\hat{g}_{\alpha}(\mathbf{x}_f,t)\,. \tag{3.23}$$

Obviously, the above scheme reduces to that in Eq. (13) when $\lambda = 1$. It should also be emphasized that the scheme in Eq. (3.22, 3.23) is 1st-order accurate in general, and can preserve 2nd-order accuracy only for the special case with straight interfaces located halfway in the lattice with $\Delta = 0.5$ for all the interface nodes [14,34,89]. One can also follow the process in [14,34,89] to construct interpolation-based decoupled interface schemes to preserve the 2nd-order accuracy for straight interfaces with arbitrary Δ values; and for curved interfaces, even though only 1st-order accuracy can be obtained, the interpolation-based interface scheme could render much more accurate results. Considering the complex geometry of the open-cell metal foams, preserving the exact geometry of the porous structure and finding the local Δ values is a rather tedious task; thus the zigzagged interface approximation as shown in Figure 3.1b is applied and only the interface scheme in Eq. (3.22, 3.23) is implemented.

3.4.4 Effective thermal conductivity evaluation

By applying constant Dirichlet boundary conditions in the y-direction, $T(y = 0) = T_L$ and $T(y = H) = T_H$, and insulated boundary conditions in the x- and z-directions, the ETC, k_{eff}, of the cubic unit lattice structure of length L in each direction can be evaluated from

$$k_{\text{eff}} = \frac{\dot{Q}_w}{(\Delta T/L)A_{xz}} = \frac{\dot{Q}_w}{\Delta TL}, \tag{3.24}$$

where $\dot{Q}_w$ is the heat transfer rate. In the LBM, $\dot{Q}_w$ can be conveniently computed using the scheme proposed in [93], and the ETC evaluation becomes

$$k_{\text{eff}} = \frac{1}{\Delta TL}\left\{ \sum_{\text{Domain 1}} \left[g_{\bar{\alpha}}(\mathbf{x}_f, t+\delta t) - \hat{g}_{\alpha}(\mathbf{x}_f, t) \right] \delta_x^2 + \lambda \sum_{\text{Domain 2}} \left[g_{\bar{\alpha}}(\mathbf{x}_f, t+\delta t) - \hat{g}_{\alpha}(\mathbf{x}_f, t) \right] \delta_x^2 \right\} \tag{3.25}$$

It should be noted that in Eq. (3.25) the diffusion coefficient is rescaled in Domain 2, i.e., $k_{s\lambda} = k_s/\lambda$, thus λ is multiplied by the flux evaluated in the LBM.

3.5 Model verification

In this section, we first verify the applicability and accuracy of the decoupled interface scheme in the LB model. The simulated results for the ETC are compared with the analytical solutions for the 3D parallel and the series mode structures (see Figure 3.5). Then the accuracy of the model is also verified by comparing the predicted ETC of the Cube structure with square cross-section fibers (SQ-Cube) and the Octet structure with circular cross-section fibers with the theoretical and computational results reported in the previous studies [60,64,65,127,128].

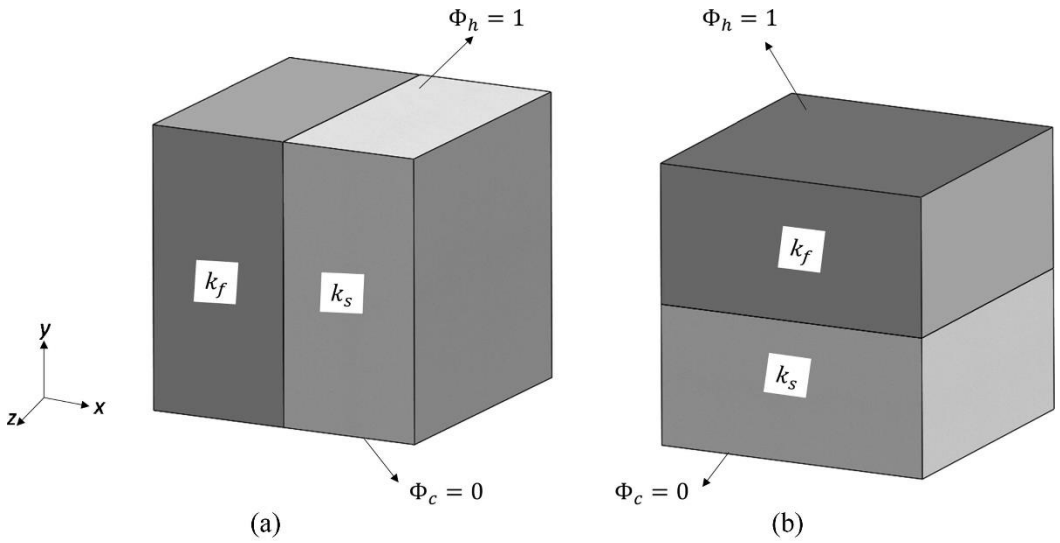

Figure 3.5 The schematic illustration of the computation domain in 3D for (a) parallel mode and (b) series mode.

3.5.1 3D parallel and series mode structures

The 3D parallel and series mode configurations are shown in Figure 3.5. Constant temperature boundary conditions are applied on the top and bottom walls in the *y*-direction, and insulated boundary conditions are on all the other walls. Considering the simplest situation with

volumes $V_s = V_f$ thus $\varepsilon = 0.5$, the analytical solutions of the ETC for the parallel and series mode structures are

$$k_{\text{eff, parallel}} = \frac{k_f + k_s}{2}, \tag{3.26}$$

$$k_{\text{eff, series}} = \left(\frac{1}{2k_f} + \frac{1}{2k_s} \right)^{-1}. \tag{3.27}$$

In the LBM simulations, the parameters used are $\Phi_h = 1$, $\Phi_c = 0$, $\tau_f = 0.51$, and $\tau_{s\lambda}$ was determined by the ratio k_s/k_f and the decoupling scaling factor λ according to Eq. (3.19, 3.20). Coarse meshes were used with $L = 30\delta x$ in all three directions for the cases with $\lambda = 10$ and $\lambda = 100$ and $L = 60\delta x$ for $\lambda = 1000$ and $\lambda = 5000$. The simulated results for the normalized ETC, k_{eff}/k_f, are compared with the exact solutions at various λ values as listed in Tables 3.1 and 3.2 for the respective thermal conductivity ratios $k_s/k_f = 10^3$ and 10^4. The comparison clearly confirms the accuracy of the proposed decoupled interface scheme: near machine-epsilon errors were achieved at $\lambda = 10$, 100 for both the parallel and series mode structures; while the effect of λ on the numerical results becomes more noticeable at $\lambda = 1000$, 5000 the error magnitude on the order of 10^{-4} can be considered extremely low.

Table 3.1 Comparison of LBM prediction of the normalized effective thermal conductivity, $(k_{eff})_{\text{LBM}}/k_f$, with the analytical solution at $k_s/k_f = 10^3$.

λ	Parallel mode[¶] $(k_{\text{eff}}/k_f)_{\text{LBM}}$	Relative error	Series mode[§] $(k_{\text{eff}}/k_f)_{\text{LBM}}$	Relative error
10	500.500000	1.23×10^{-10}	1.998002	5.14×10^{-8}
100	500.500000	1.37×10^{-10}	1.998002	8.76×10^{-8}
1000	500.499953	-9.40×10^{-8}	1.998135	6.68×10^{-5}
5000	500.499722	-5.55×10^{-7}	1.998717	3.58×10^{-4}

[¶] $(k_{\text{eff}}/k_f)_{\text{analytical}} = 500.5$ for the parallel mode

[§] $(k_{\text{eff}}/k_f)_{\text{analytical}} = 1.998002$ for the series mode

Table 3.2 Comparison of LBM prediction of the normalized effective thermal conductivity, $(k_{eff})_{LBM}/k_f$, with the analytical solution at $k_s/k_f = 10^4$.

λ	Parallel mode[¶] $(k_{eff}/k_s)_{LBM}$	Relative error	Series mode[§] $(k_{eff}/k_s)_{LBM}$	Relative error
10	5000.500000	1.22×10^{-11}	1.99980012	4.88×10^{-8}
100	5000.500000	1.22×10^{-11}	1.99980012	4.99×10^{-8}
1000	5000.500000	1.37×10^{-11}	1.99980020	8.91×10^{-8}
5000	5000.499949	-1.01×10^{-8}	2.0003495	2.75×10^{-4}

[¶] $(k_{eff}/k_f)_{analytical} = 5000.5$ for the parallel mode

[§] $(k_{eff}/k_f)_{analytical} = 1.99980002$ for the series mode

3.5.2 Structure with square cross-section fibers

Heat conduction simulation in the Cube structure with square cross-section fibers (SQ-Cube, see Figure 3.6) is considered in this test as the geometry can be exactly preserved in the LBM and all the boundary and interface schemes have second-order accuracy. To the best of the authors' knowledge, the exact analytical solution for the 3D temperature field is not available and thus the existing approximate models (typically assuming 1D conduction) for the ETC are used for verification.

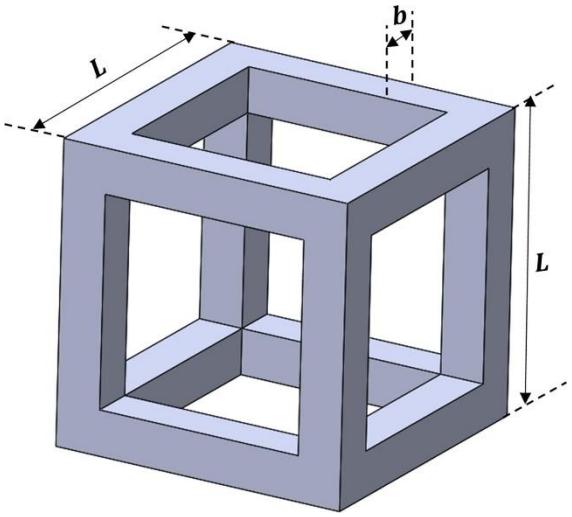

Figure 3.6 Schematic of SQ-Cube unit cell structure.

Dul'nev [129] proposed the following expression for the ETC of the SQ-Cube structure

$$k_{eff} = k_s t^2 + k_f (1-t)^2 + \frac{2t(1-t)k_f k_s}{k_s(1-t)+k_f t}, \tag{3.28}$$

where $t = b/L$ with b the thickness of the fiber (beam), and Fu et al. [59] developed an analytical model for the same SQ-Cube structure based on the thermal-circuit analogy

$$k_{eff} = \left[\frac{2t}{4t(1-t)k_s + (1-2t)^2 k_f} + \frac{1-2t}{4t^2 k_s + (1-4t^2)k_f} \right]^{-1}, \tag{3.29}$$

Figure 3.7 compares the LBE results for the normalized ETC of SQ-Cube with Dul'nev and Fu et al.'s models. In LBE simulations, $L = 180\delta x$ was used for all cases and the porosity was characterized by $t = b/L$. The porosity calculated in the LBE is exact with the SQ-Cube structure. The other parameters used are $\tau_f = 0.525$, $\lambda = 250$ (thus rescaled $\tau_{s\lambda} = 1.33$) for the aluminum-air, and $\tau_f = 0.55$, $\lambda = 75$ ($\tau_{s\lambda} = 0.74$) for the aluminum-water case. The present simulation results are in good agreement with the two analytical models for both cases. It is also observed that the ETC results of the aluminum-air and aluminum-water cases are very close,

indicating that the effect of the ratio k_s/k_f on the normalized ETC k_{eff}/k_s is small, especially at high porosity. This will be further discussed in the Results and Discussion section.

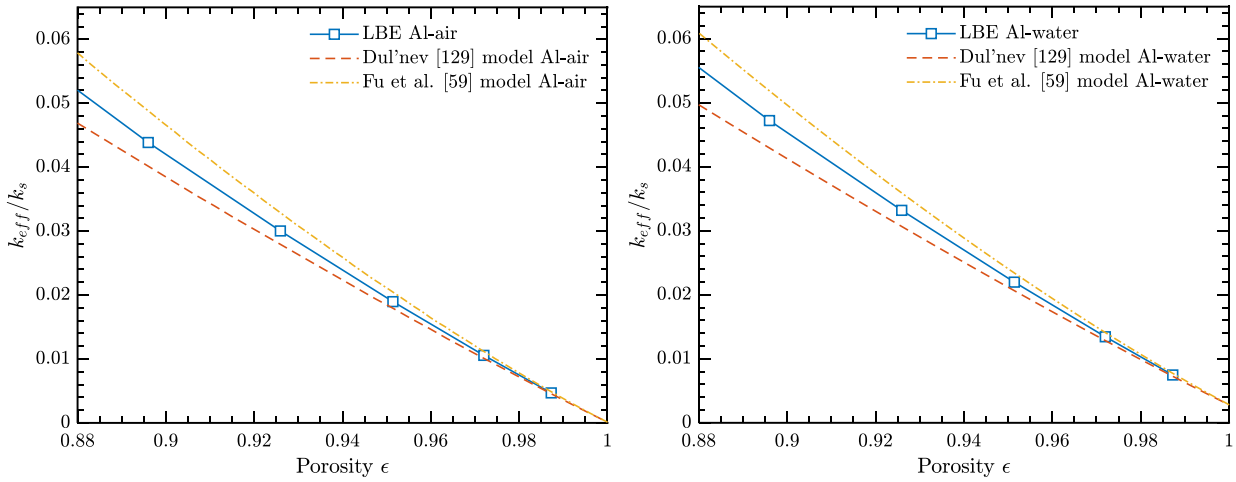

Figure 3.7 Comparison of normalized effective thermal conductivity (k_{eff}/k_s) for SQ-Cube structures (a) aluminum-air, and (b) aluminum-water cases.

3.5.3 Octet structure with circular cross-section fibers

The LB model with the decoupled interface scheme is further applied to predict the ETC of the Octet truss structure with circular cross-section fibers of radius r, and the results are compared with the direct simulations and experimental data in the present study as well as in previous research [65,66,69] to verify the accuracy of the model for the curved-interface structure. In present LB simulations for all porous structures, the zigzagged interface as shown in Figure 3.4b is used to approximate the curved interface, and the porosity is conveniently computed using $\varepsilon = 1 - \frac{N_{fiber}\delta_x^3}{L^3}$ with N_{fiber} the total number of solid fiber nodes. Table III shows

the porosity comparison at $L = 180\delta x$ with those in Ekade et al. [65] obtained with commercial software.

Table 3.3 Porosity comparison between present calculations and those in [127] for the Octet structure.

L/r	Ekade et al. [65]	Present	Relative deviation
10	0.62	0.6213	0.210%
13.333	0.765	0.7692	0.549%
15	0.809	0.8089	-0.012%
20	0.886	0.8843	-0.192%
30	0.946	0.9465	0.053%

The comparison in Table 3.3 confirms the reliability in the porosity calculation of the zigzagged interface approximation with the LB mesh of $L = 180\delta x$. Furthermore, a grid independence study was conducted to ensure that the resolution is sufficient to compute the ETC. Table 3.4 shows the results for both the AM TKD and Octet structures with material pair of 420 stainless steel with 40% bronze infiltration-air ($k_s/k_f = 792.7$) at different grid resolution. The simulation parameters include $\tau_f = 0.55$, $\lambda = 150$ for both, and $L/d_{fiber} = 6$ for the TKD and $L/d_{fiber} = 7.5$ for the Octet structures, respectively. The present measurement data for those structures at similar porosities are also included for comparison (more details can be found in Chapter 3.6.1). The data in Table 3.4 confirms that the resolution with $L = 180\delta x$ is sufficient and this will be used for all the results presented in Chapter 3.6.

The normalized ETC results, k_{eff}/k_s, for the Octet structure at different porosities are compared with the present experimental data and those previous published data in [66], [65], [69] in Figure 3.8.

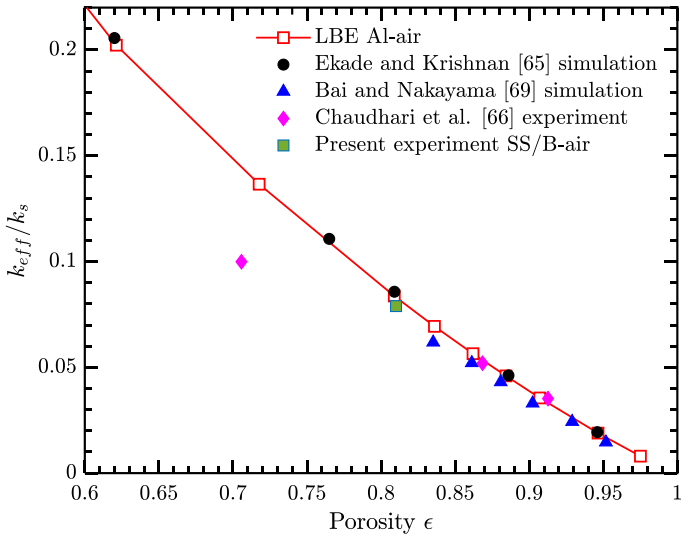

Figure 3.8 Comparison of normalized effective thermal conductivity (k_{eff}/k_s) for the Octet structure.

The LB results are close to both the experimental measurement in [66] and simulation results in [69] at high porosities $\varepsilon > 0.85$. Good agreement is also noticed between the LB results and the present measurement at $\varepsilon = 0.81$ (details in Chapter 3.6.1). More importantly, excellent agreement is observed between the LB results and those by Ekade and Krishnan [65] from direct numerical simulation for the entire range of $0.6 < \varepsilon < 1$. This test further verifies the numerical accuracy of the present LB simulations for predicting the ETC of the AM structures with complex geometry.

3.6 Results and discussion

In this section, we first report the experimental results of the ETC of the TKD and Octet structures. Then detailed computational results are presented, including the interior temperature contours for all four lattice structures, and the ETC results for the TKD and Octet structures validated using present and previously published experimental results. Lastly, the detailed results for the ETC of the four structures (Cube, FD-Cube, TKD and Octet) are presented, and practical correlations for the ETC as a function of porosity are provided. In particular, the results presented in this paper demonstrate that at high porosities ($\varepsilon > 0.9$), the present LB simulation results for the ETC are consistent with all experimental, analytical, and computational results in the literature for metal foams; however, at lower porosities, the effect of the structure on the ETC becomes more obvious, and the additively manufactured structures provide a feasible way to examine the structural effect. The practical and accurate correlations developed in this work based on detailed LB simulations are valuable for future structural design and optimization.

3.6.1 Experimental results

The temperature measurements of the solid sample (k_s determination) is presented in Figure 3.9. The solid thermal conductivity was calculated using $k_s = q"_w/(dT_w/dx)$, where $q"_w$ is the net heat conducted through the solid in one direction (x). Experiments were conducted at three different heat flux values ranging from ~5,400 to 9,600 W/m^2 to ensure that the reported k_s is independent of the thermal boundary condition and is solely a function of material properties. A linear variation in the centerline temperature was observed for all three heat flux values, from where the temperature gradient was determined. The different heat input experiments essentially yielded in similar values of k_s with a mean value of 20.8 W/mK. This value of k_s will be considered in further experimental presentation of k_{eff}.

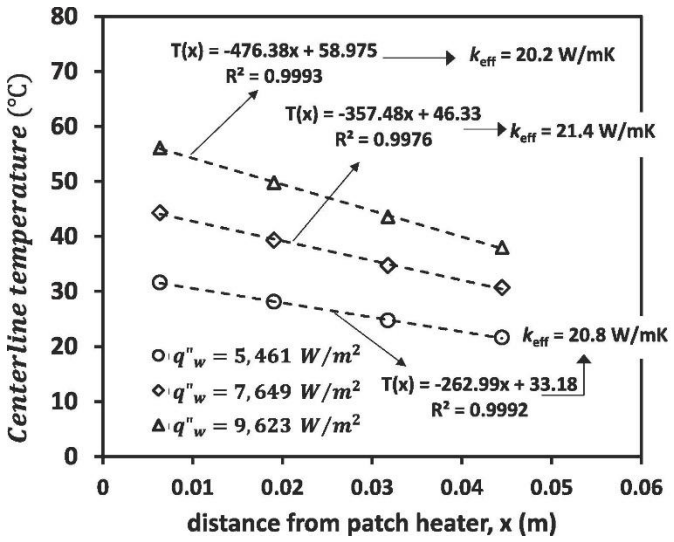

Figure 3.9 Centerline temperature variation along the direction of net heat flow.

The k_{eff} experiments for porous blocks were also conducted at three different inputs such that the reported value is only a function of material property and unit cell topology.

The k_{eff} experimental results for Octet and TKD samples are presented in Figure 3.10 with an uncertainty analysis carried out following the "sequential perturbation method" [130]. The respective porosities of Octet and TKD samples were 0.81 and 0.86.

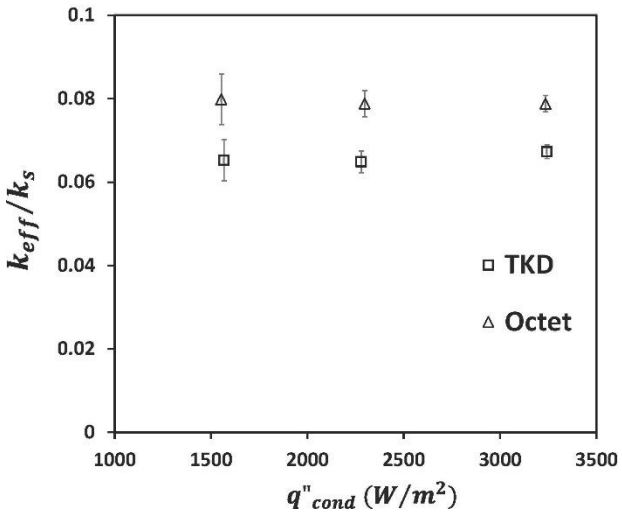

Figure 3.10 k_{eff}/k_s variation with conduction heat flux $q"_{cond}$. Porosities of the TKD and Octet samples were 0.86 and 0.81, respectively.

The results indicate that the k_{eff}/k_s values for both samples were independent of the supplied heat flux and the average values were 0.079 and 0.066 for Octet and TKD samples respectively. The k_{eff}/k_s results of the Octet sample were slightly higher than that of TKD and this difference is primarily attributed to the difference in their porosities. This factor will be further discussed in 3.6.3 Validation of LB simulation results, 3.6.4 Comparison of LBM results with previous models and correlations.

3.6.2 Temperature contours within lattice structures from LB simulations

For illustration purposes, representative steady-state temperature contours in the central *x*-*z* and *x*-*y* planes of all four structures are shown in Figure 3.11 with $L = 180\delta x$, $L/d_{fiber} = 15$, and $k_s/k_f = 8307.9$ (aluminum-air). The temperature distribution demonstrates that the LB model and simulations were able to preserve the fiber structural geometry and symmetry of different structures. The effect of the high thermal conductivity ratio between the solid fiber and air on conjugate heat conduction at the interface is

clearly seen in the temperature contours. For instance, in Figure 3.11 (c, d) it can be observed that the temperature gradient in the gas phase is much higher than that in the solid phase along the normal direction of the fiber interface (see Eq. (3.3)).

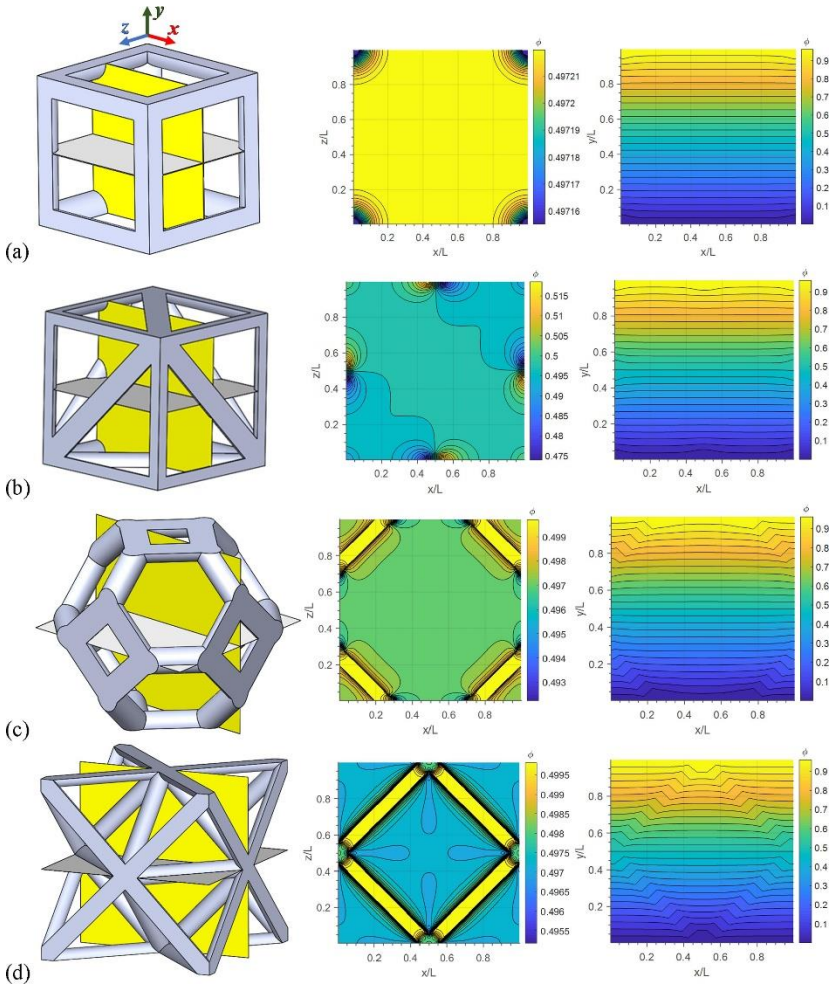

Figure 3.11 Temperature contours for different lattice structures with (a) Cube, (b) FD-Cube, (c) TKD, and (d) Octet unit cells. Simulation parameters are $d_{fiber} = 12\delta_x$, $L/d_{fiber} = 15$, $k_s/k_f = 8307.9$, $\tau_f = 0.525$, and $\lambda = 250$.

In all the results shown here and the remaining sections in 3.5.3 to 3.5.5 for steady LBM simulations for the various porous lattice structures, the main simulation parameters

include $L = 180\delta x$, $(\tau_f, \lambda) = (0.525, 250)$ for aluminum-air ($k_s/k_f = 8307.9$), $(\tau_f, \lambda) = (0.55, 75)$ for aluminum-water ($k_s/k_f = 355.6$), and $(\tau_f, \lambda) = (0.55, 150)$ for the 420 stainless steel with 40% bronze infiltration-air ($k_s/k_f = 792.7$) material pairs. By choosing different fiber diameter d_{fiber} the porosity of the AM structures can be conveniently manipulated.

3.6.3 Validation of LB simulation results

Figure 3.12, Figure 3.13 show the comparison of LBM simulation results for the normalized ETC, k_{eff}/k_s, of the AM TKD and Octet structures with our experimental measurement (averaged from Figure 3.10) as well as the experimental results reported in [49], [52], [53], [56], [66], [131]. It should be noted that in Figure 3.12a, b, all the structures were additively manufactured thus the porosity can be well controlled over a wide range; while in Figure 3.13 the experimental results for conventional metal foams obtained from foaming processes with high porosity ($\varepsilon > 0.88$) were used for comparison. Furthermore, the fluid–solid pairs considered include aluminum-air, aluminum-water, copper-air, copper–water, copper-paraffin, as well as the 420 stainless steel with 40% bronze infiltration-air (denoted as SS/B-air) used in our in-house experiment.

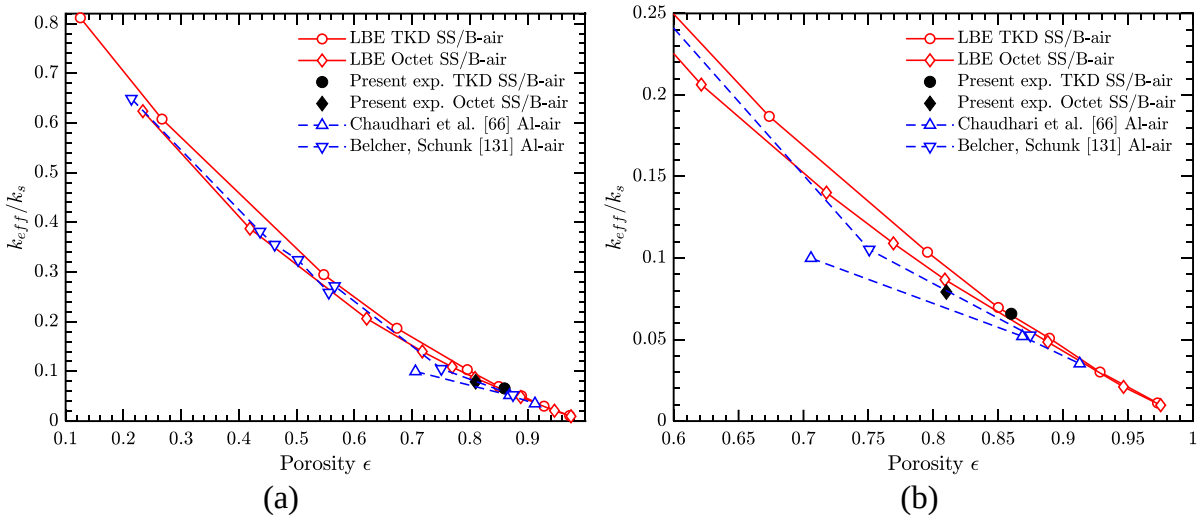

Figure 3.12 Comparison of the simulated results for the normalized effective thermal conductivity, k_{eff}/k_s, of the TKD and Octet structures with present and previous experimental results for additively manufactured structures. (a) Results shown in the wide range of $0.1 < \varepsilon < 1.0$, and (b) results in the range of $0.6 < \varepsilon < 1.0$.

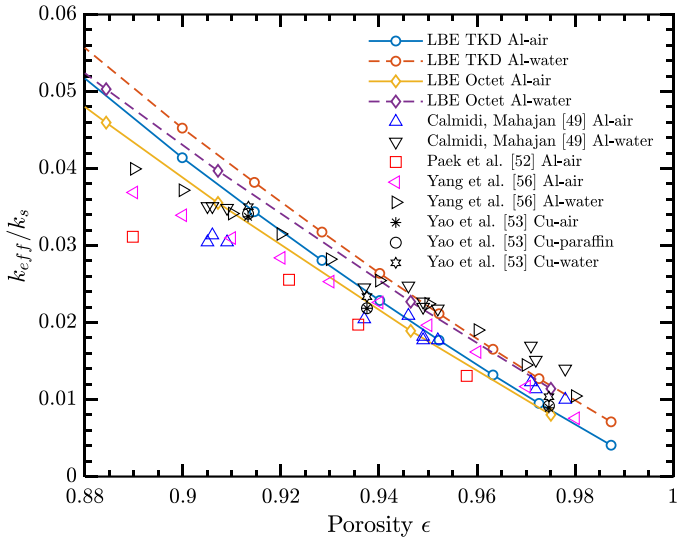

Figure 3.13 Comparison of the simulated results k_{eff}/k_s of the TKD and Octet structures with previous experimental results of conventional high-porosity metal foams.

First of all, the overall agreement between the LBM simulations and all the experimental results confirms the accuracy and reliability of the LB model and the proposed decoupled

interface treatment. Second, it is observed that at high porosities $\varepsilon \geq 0.9$, the ETC of various metal foams, including conventional and AM structures as well as different fluid–solid pairs, can all be well presented in terms of k_{eff}/k_s versus the porosity, i.e., they almost all fall into an overlapped narrow band with porosity as the controlling parameter. Considering the wide ranges of structural variations and k_s/k_f ratios included in those data, this implies that the normalized ETC result can be applied to various metal foams of interest. Third, when the porosity decreases, the effect of the structure on the normalized ETC becomes more obvious from the LB simulations. Specifically, the excellent agreement in Figure 3.12b between our simulation and in-house experimental results for both TKD and Octet structures provides the confidence in the LBM results for AM structures; moreover, the overall agreement between the LBM simulations and the results in [131] for AM structures in the wide range of $0.2 \leq \varepsilon < 1.0$ further confirms the validity of the present simulation results.

3.6.4 Comparison of LBM results with previous models and correlations

The validated LB model and decoupled interface scheme can be used as an effective tool to study the dependence of the ETC on the structural geometry and porosity. It is thus of particular interest to compare the simulation results with the ETC correlations in the literature. As reviewed in [43], a comprehensive comparison of the various models and correlations is clearly out of the scope of this study and thus only a few popular ETC correlations were selected for comparison. It should be noted that most of those correlations were developed to match the available experimental data for conventional metal foams at high porosities.

Based on their experimental data, Calmidi and Mahajan [49] developed an empirical correlation

$$k_{eff} = k_f \varepsilon + A(1-\varepsilon)^n k_s , \tag{3.30}$$

with $A = 0.181$ for air and 0.195 for water, and $n = 0.763$.

Bhattacharya et al. [51] proposed an empirical correlation with weighted contributions from the parallel and series mode limits, and the weighting constant was determined by matching the experimental data

$$k_{eff} = A(\varepsilon k_f + (1-\varepsilon)k_s) + \frac{1-A}{(\frac{\varepsilon}{k_f} + \frac{1-\varepsilon}{k_s})}, \tag{3.31}$$

where $A = 0.35$ was recommended.

Chaudhari et al. [66] also constructed a similar correlation to Eq. (3.30), and by fitting with their aluminum-air experimental data, $A = 0.2781$ and $n = 0.8406$ was proposed.

It is also noted that the Lemlich theory [132] for ETC prediction based on the analogy between electrical and thermal conductivities was widely used due to its simple expression

$$k_{eff} = \frac{1-\varepsilon}{3} k_s, \tag{3.32}$$

Furthermore, Belcher and Schunk [131] proposed a second-order polynomial for the ETC as a function of porosity in the entire range of $0 \le \varepsilon \le 1$:

$$k_{eff} = a_0\varepsilon^2 + a_1\varepsilon + a_2, \tag{3.33}$$

The coefficients were determined by fitting with their experimental results for additively manufactured porous structures. Using the $k_s = 204.90$ W m^{-1} K^{-1} and coefficients given in [57], Eq. (3.23) can be rewritten as

$$\frac{k_{\text{eff}}}{k_s} = 0.7313\varepsilon^2 - 1.7188\varepsilon + 0.9922, \tag{3.34}$$

The comparison in terms of k_{eff}/k_s between the present LBM results and those obtained from the correlations in Eqs. (3.30)–(3.34) proposed in [49], [51], [66], [131], [132] is shown in Figure 3.14 (a, b) where the respective material pairs are Al-air and Al-water. Obviously, good agreement is observed between the present LBM simulations and all the ETC results obtained

from the correlations in Eqs. (3.30)–(3.34) at high porosities ($\varepsilon > 0.9$); however, when extended to lower porosity cases, all the correlations in Eqs. (3.30)–(3.32) developed based on conventional metal foams seem to significantly underestimate the ETC compared to the LBM simulation results. Furthermore, it should be highlighted that the second-order polynomial in Eq. (3.34) yields ETC results very close to the LBM results for the Octet structure. Combining with the agreement also observed in Figure 3.12a, this indicates that the second-order polynomials can be suitable fitting correlations for the normalized ETC. Lastly, the difference in the ETC between the TKD and Octet structures from LBM simulations implies that the effect of topology on the ETC becomes important at lower porosities. Individual second-order polynomials can thus be developed for the various AM structures. The details will be given in the next section.

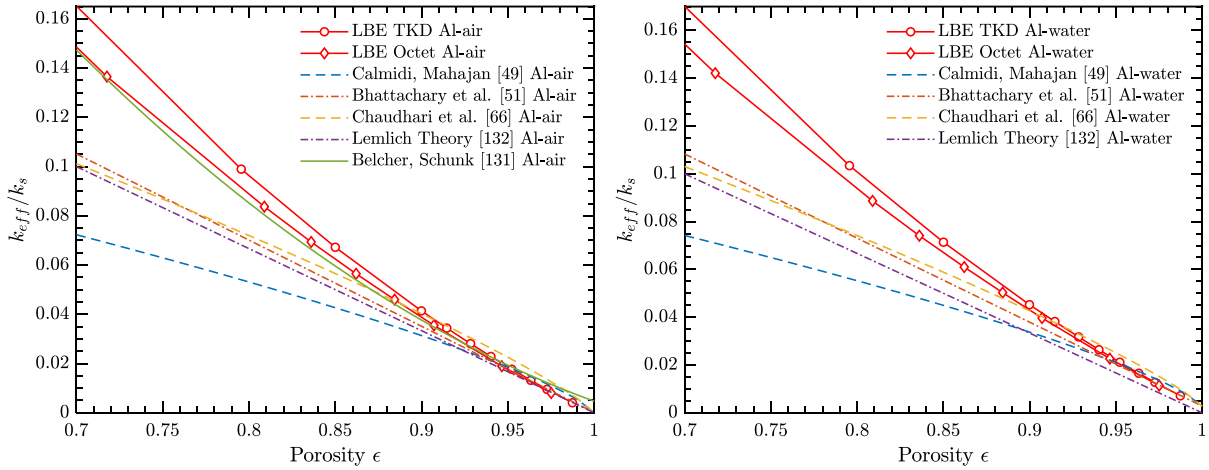

Figure 3.14 Comparison of the effective thermal conductivity, k_{eff}/k_s, between LBM simulations and those from previous correlations for the AM TKD and Octet structures with (a) Al-air, and (b) Al-water material pairs.

3.6.5 Development of ETC correlations for porous lattice structures

A thorough investigation based on systematic LB simulations into the dependence of the ETC on the porosity was conducted for all four structures and for the three material pairs, i.e., aluminum-air, aluminum-water and SS/B-air. When presented in terms of the normalized ETC, k_{eff}/k_s, it was observed that all the data can be well captured using second-order polynomials for the entire range of $0 \le \varepsilon \le 1$. Therefore, the following correlation is proposed for each lattice structure

$$\frac{k_{\text{eff}}}{k_s} = a_{st}\varepsilon^2 + \left(\frac{k_f}{k_s} - 1 - a_{st}\right)\varepsilon + 1, \tag{3.35}$$

where a_{st} is the only constant coefficient and assumed to be structure dependent. The correlation proposed in (3.35) includes the two limits at $\varepsilon = 0$ ($k_{\text{eff}} = k_s$) and $\varepsilon = 1$ ($k_{\text{eff}} = k_f$); it also has the quadratic dependence on ε similar to the polynomial proposed by Belcher and Schunk [131] in Eqs. (3.33) and (3.34). Using all three data sets at different k_s/k_f ratios, a_{st} can determined from the least squares method

$$a_{st} = \frac{-\sum_i \varepsilon_i\left(\varepsilon_i - 1\right)\left[\left(\frac{k_f}{k_s} - 1\right)\varepsilon_i + 1 - \left(\frac{k_{\text{eff}}}{k_s}\right)_{\text{LBE},i}\right]}{\sum_i \varepsilon_i^2\left(\varepsilon_i - 1\right)^2}, \tag{3.36}$$

Based on the LBM simulations, the coefficients for the four lattice structures are

$$a_{\text{Cube}} = 0.6577,\ a_{\text{FD-Cube}} = 0.7231,\ a_{\text{TKD}} = 0.6390,\ a_{\text{Octet}} = 0.7397\ , \tag{3.37}$$

and the normalized ETC can be explicitly rewritten as

$$\frac{k_{\text{eff}}}{k_s}=\begin{cases}0.6577\varepsilon^2+\left(\dfrac{k_f}{k_s}-1.6577\right)\varepsilon+1, & \text{Cube structure}\\ 0.7231\varepsilon^2+\left(\dfrac{k_f}{k_s}-1.7231\right)\varepsilon+1, & \text{FD-Cube structure}\\ 0.6390\varepsilon^2+\left(\dfrac{k_f}{k_s}-1.6390\right)\varepsilon+1, & \text{TKD structure}\\ 0.7397\varepsilon^2+\left(\dfrac{k_f}{k_s}-1.7397\right)\varepsilon+1, & \text{Octet structure}\end{cases}, \tag{3.38}$$

It is also of interest to present an averaged correlation based on the 4 structures examined. Thus a general correlation is also proposed in this work as

$$\frac{k_{\text{eff}}}{k_s}=0.6899\varepsilon^2+\left(\frac{k_f}{k_s}-1.6899\right)\varepsilon+1, \tag{3.39}$$

The deviation of the coefficients for the four specific structures in Eq. (3.38) is within 7.4% of that in the general correlation (3.39).

Figure 3.15 (a-d) shows the respective comparison between the LBM simulations and the correlation results for the normalized ETC of the four structures. The plots clearly show that the correlation results match extremely well with all the direct LBM simulations, and the normalized ETC k_{eff}/k_f is insensitive to the k_s/k_f ratios for the three cases examined with the ratio k_s/k_f up to 8307.9, i.e., the correlations are applicable to various material pairs. Furthermore, Figure 3.16 shows the comparison of the particular correlations in Eq. (3.38) with the general correlation in Eq. (3.39) for the Al-air case. The overall agreement is good and deviation can be noted particularly in the porosity range of $0.3 < \varepsilon < 0.8$. Nevertheless, the general correlation in Eq. (3.39) can serve as a useful and convenient prediction tool for future AM structures design and optimization for specific applications.

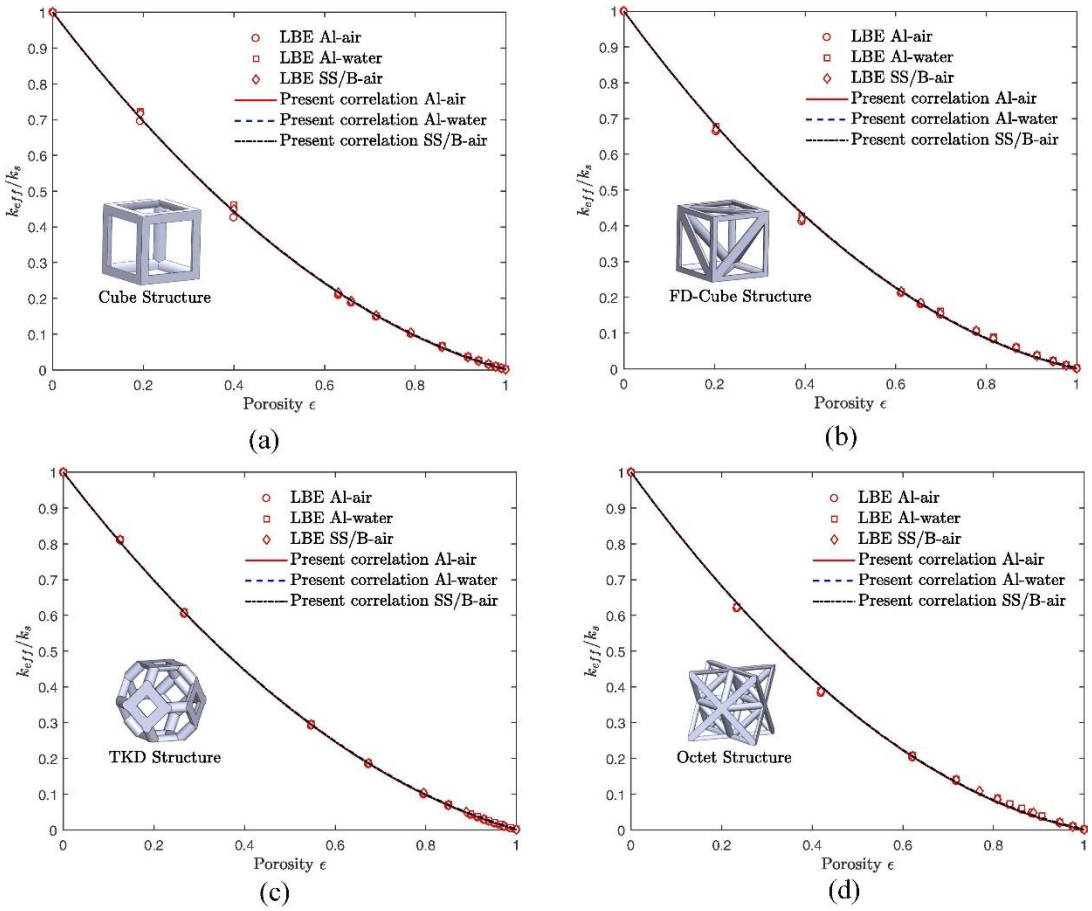

Figure 3.15 Normalized effective thermal conductivity of the (a) Cube, (b) FD-Cube, (c) TKD, and (d) Octet structures obtained from LBM simulations and proposed correlations.

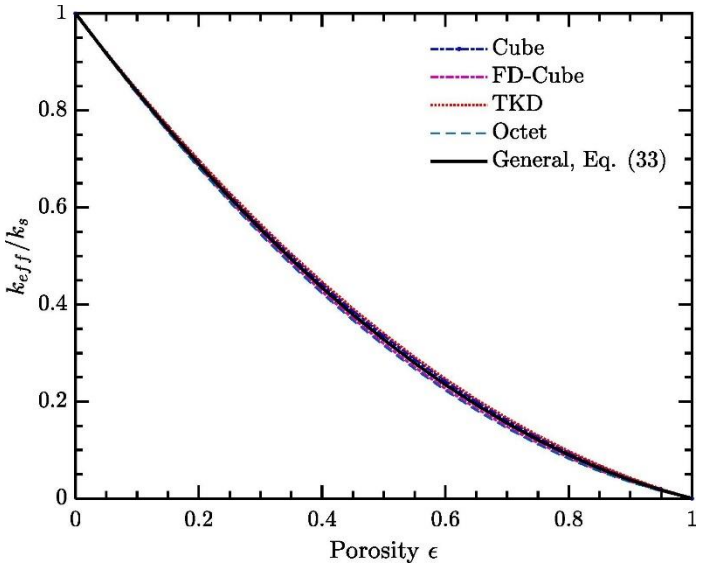

Figure 3.16 Comparison of the specific and general correlations in Eqs. (3.37, 3.38) for the effective thermal conductivity of porous lattice structures (Al-air material pair used for demonstration).

The correlations in Eq. (3.39) can also be used to predict the effective thermal conductivity of those structures when packed with solid particles. However, the correlation is proposed for the entire porosity range of $0 \leq \varepsilon \leq 1$, while the in-house measured porosity range of the metal foam structure is $0.7 \leq \varepsilon \leq 0.9$. Therefore, to improve the accuracy of ETC prediction, here we provide a modified correlation based on the high porosity range and the two metal pairs, i.e., SS420-air and SS316L-air,

$$\frac{k_{\text{eff}}}{k_s} = \begin{cases} 0.6910\varepsilon^2 + \left(\frac{k_f}{k_s} - 1.6910\right)\varepsilon + 1, & \text{SS420-air} \\ 0.6944\varepsilon^2 + \left(\frac{k_f}{k_s} - 1.6944\right)\varepsilon + 1, & \text{SS316L-air} \end{cases} \tag{3.40}$$

The comparison of ETC between the in-house measurement, the correlation proposed by [111] and the modified correlation is shown in Fig. 3.17. It can be seen that the modified correlation

is generally more consistent with in-house measurement. To quantify the comparison with experimental results, Fig. 3.18 shows the relative errors of the two correlations. Obviously, the modified correlation improves the accuracy of ETC prediction, especially at high porosity.

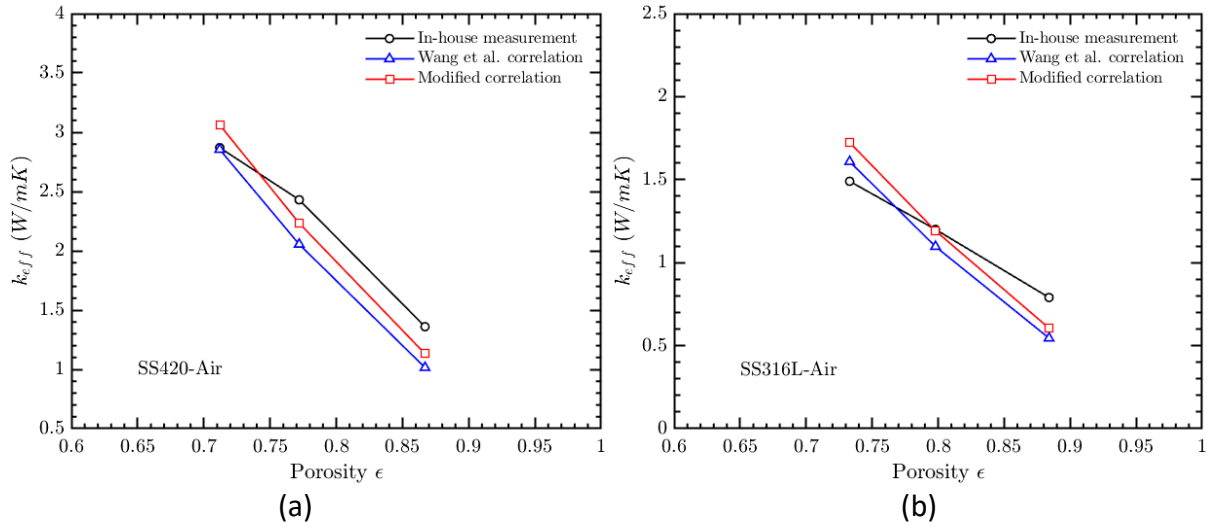

Figure 3.17 Comparison of the effective thermal conductivity between in-house measurement and correlations for the AM Octet structure with (a) SS420-air, and (b) SS316L-air material pairs.

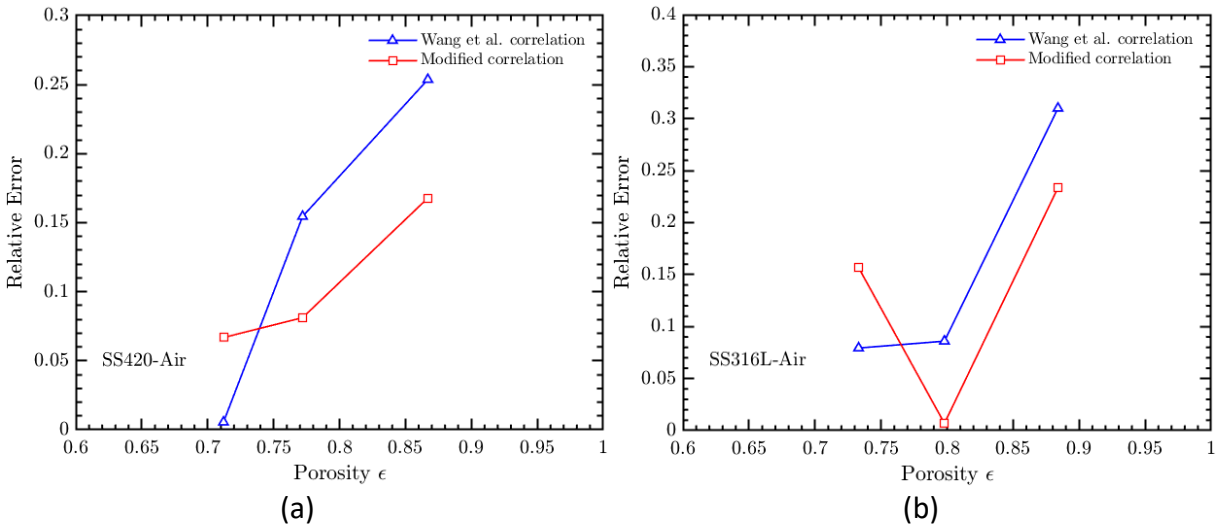

Figure 3.18 Comparison of the relative errors for the k_{eff} correlations for the AM Octet structure with (a) SS420-air, and (b) SS316L-air material pairs.

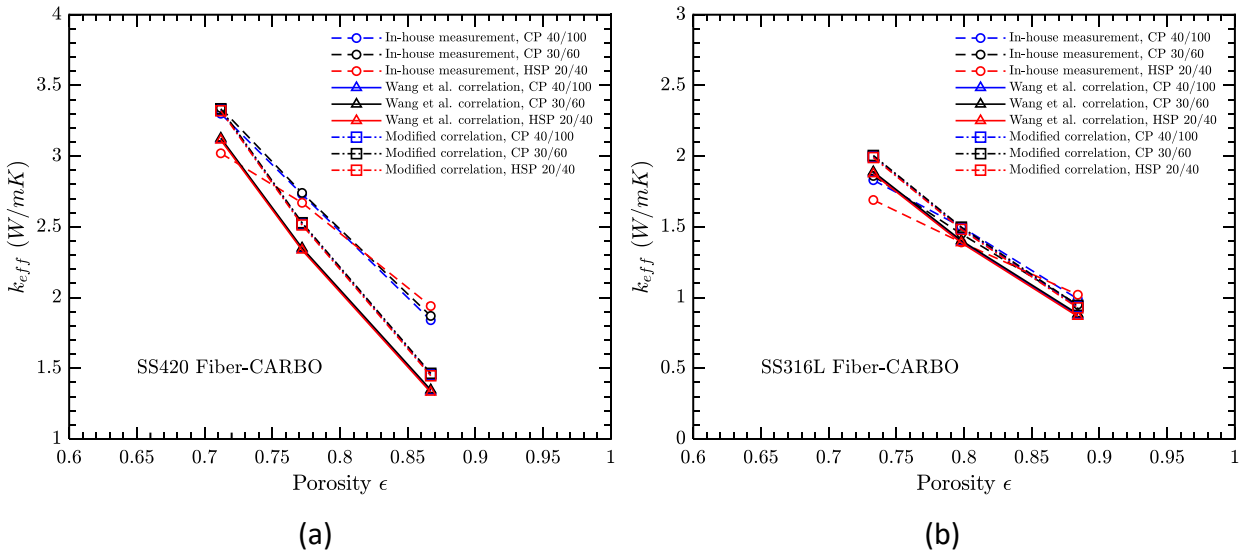

Figure 3.19 Comparison of the predicted k_{eff} with the modified correlations for the AM Octet structure with (a) SS420 Fiber-CARBO packed bed, and (b) SS316L Fiber-CARBO packed bed of particles.

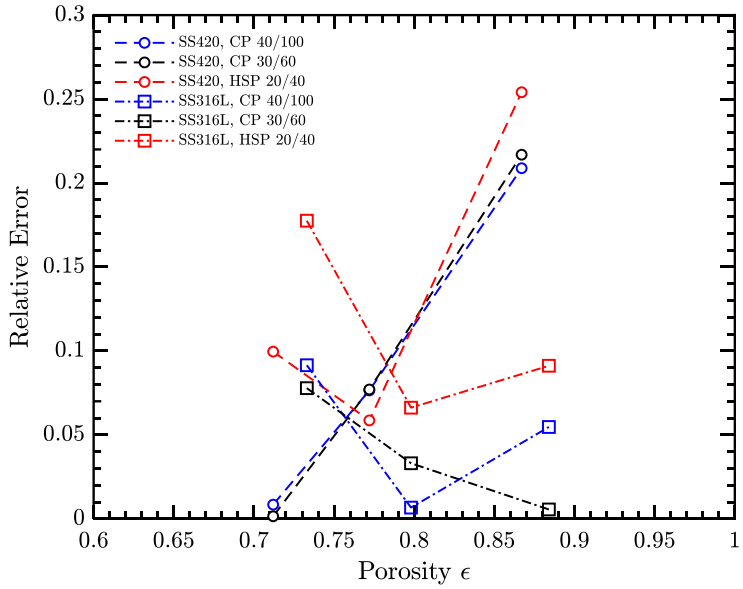

Figure 3.20 Comparison of the relative errors for the k_{eff} correlations for the AM Octet structure with SS420 Fiber-, and SS316L Fiber-CARBO packed bed of particles.

Fig. 3.19 (a, b) shows the predicted k_{eff} of the AM Octet structure when the void space is occupied by packed bed of CARBO particles. The correlation proposed by Wang et al. [111] and

the modified correlation in Eq (3.40) are used to compare with the in-house measurement. It can be observed that those models are able to predict the overall k_{eff} of the whole structure with good agreement with the in-house measurement. The comparison of the relative errors for the k_{eff} correlations for the AM Octet structure with different material and packed solid particles are shown in Fig. 3.20. The results show that a low relative error between the predicted value and the in-house measurement when the porosity is approximately 0.8.

3.7 Conclusions

An effective and accurate lattice Boltzmann method (LBM)-based computational model was developed to predict the effective thermal conductivity (ETC) of lattice structures based on different topologies. The novelty of the model includes a decoupled interface scheme that is particularly attractive to satisfy the conjugate heat transfer conditions between different materials or phases of very high transport property ratios. This model can be conveniently extended to simulate coupled flow and thermal transport in porous structures such as metal foams. The applicability and accuracy of the LBM model and the interface scheme in terms of ETC prediction were numerically verified and experimentally validated with in-house measurement on additively manufactured (AM) metal foam samples with those topologies as well as previously published results. The predicted ETC results of the representative Cube, FD-Cube, TKD and Octet structures show good agreement with both previous experimental and analytical/computational results for conventional high-porosity metal foams with $\varepsilon > 0.9$. At lower porosities, the effects of the structure porosity and topology on the ETC were investigated using the proposed LBM model; and the simulation results demonstrated that the popular

correlations in the literature would substantially underestimate the ETC of those structures. Hence, systematic simulations for all four structures and for different solid–fluid material pairs have been conducted, and analytical correlations as second-order polynomials of the porosity for the entire range of $0 \leqslant \varepsilon \leqslant 1$ were developed. The correlations for the ETC normalized by the solid thermal conductivity k_{eff}/k_s are applicable to various material pairs. The modified correlation based on the high porosity range and the two metal pairs can improve the accuracy of ETC prediction for specific application. They can serve as valuable evaluation and prediction tools for future design and innovation in AM structures as lightweight and compact heat sinks/exchangers. In this chapter, only heat conduction within the unit cells is considered to predict the ETC. With the attractiveness also in simulating fluid flow and handling complex geometry, the coupled LBM model (e.g., with one set of distribution functions for the fluid flow and another for the temperature convection–diffusion) is well poised to be an alternative and powerful computational tool in predicting and characterizing the various flow and thermal transport properties in porous lattice structures. Results from the above investigations will be communicated in future publications.

CHAPTER IV

PHASE-FIELD-LATTICE BOLTZMANN METHOD FOR DENDRITIC GROWTH WITH MELT FLOW AND THERMOSOLUTAL CONVECTION-DIFFUSION*

The previous chapters focused on conjugate heat and mass transfer modeling using the lattice Boltzmann method with sharp interface scheme in theoretical/numerical tests and engineering applications, respectively. In this Chapter a new phase-field model is proposed, which employs the concept of a diffuse interface, formulated within the system of lattice Boltzmann (LB) equation for simulating solidification and dendritic growth with fully coupled melt flow and thermosolutal convection-diffusion. With the evolution of the phase field and the transport phenomena all modeled and integrated within the same LB framework, this method preserves and combines the intrinsic advantages of the phase-field method (PFM) and the lattice Boltzmann method (LBM). Particularly, the present PFM/LBM model has several improved features compared to the existing phase-field models including: (1) a novel multiple-relaxation-time (MRT) LB scheme for the phase-field evolution is proposed to effectively model solidification coupled with melt flow and thermosolutal convection-diffusion with improved numerical stability and accuracy, (2) convenient diffuse interface treatments are implemented for the melt flow and thermosolutal transport which can be applied to the entire domain without tracking the interface, and (3) the evolution of the phase field, flow, concentration, and

* Part of this chapter is based on work published in Computer Method in Applied Mechanics and Engineering in 2021 [133]

temperature fields on the level of microscopic distribution functions in the LB schemes is decoupled with a multiple-time-scaling strategy (despite their full physical coupling), thus solidification at high Lewis numbers (ratios of the liquid thermal to solutal diffusivities) can be conveniently modeled. The applicability and accuracy of the present PFM/LBM model is verified with four numerical tests including isothermal, iso-solutal and thermosolutal convection-diffusion problems, where excellent agreement in terms of phase-field and thermosolutal distributions and dendritic tip growth velocity and radius with those reported in the literature is demonstrated. The proposed PFM/LBM model can be an attractive and powerful tool for large-scale dendritic growth simulations given the high scalability of the LBM.

This rest of this Chapter is organized as follows. The governing equations for the phase field, melt flow, concentration (solute) field, and temperature field and their coupling are described in Section 4.2. The specific LBM-based numerical schemes in the proposed PFM/LBM model for solving those governing equations are presented in Section 4.3. Model verification and discussion are then detailed in Section 4.4. And concluding remarks are provided in Section 4.5. Lastly, the Chapman-Enskog analysis for the MRT-LBM scheme to recover the phase-field evolution equation is presented in Appendix A, and Appendix B briefly explains the algorithms used to compute the dendritic tip growth velocity and radius.

4.1 Introduction

In the CFD and heat and mass transfer communities, the lattice Boltzmann method (LBM) has become a powerful and alternative numerical method for modeling fluid flows and thermal/mass transport problems with complex geometry due to its attractive features including simple algorithm, easy implementation, convenience in boundary and interface treatment, and compatibility with parallel computing [14,23,25,26,83,84,86,87,126]. It is no surprise that a

growing number of publications have focused (e.g., [30–33]) on coupling the PFM and LBM for dendritic growth simulations. Most of those PFM-LBM models can be considered as *hybrid* models in which finite-difference- or finite-volume-based PFM was applied to simulate the phase field evolution, while the LBM was implemented to model the melt flow and heat and solute transfer. In addition, fully coupled PFM models considering all the effects of melt flow and thermosolutal convection-diffusion in the literature are very rare (e.g., [88]) due to the lack of general, convenient, and efficient numerical schemes.

4.2 Phase-field equation and conservation equations

4.2.1 Phase field

In the phase field methods, a continuous dimensionless phase-field variable, ϕ, is defined with $\phi = -1$ in the liquid phase, $\phi = 1$ in the solid phase, and varying smoothly in the diffuse interface ($-1 \le \phi \le 1$). To determine the governing equation for the phase field in thermosolutal convection-diffusion problems, the following dimensionless concentration (also called supersaturation) and temperature (also called undercooling) variables are defined for the entire domain [70,134]

$$U = \frac{\dfrac{2c/c_\infty}{(1+k)-(1-k)\phi} - 1}{1-k}, \tag{4.1}$$

$$\theta = \frac{T - T_m - mc_\infty}{L_h/C_p}, \tag{4.2}$$

where c_∞ is the far-field concentration that equals the initial concentration of the alloy, $k = c_s/c_l$ the partition coefficient that relates the compositions of solid and liquid in contact with each other at the interface, T_m the melting temperature, m the slope of the liquidus line in the phase diagram, L_h the latent heat, and C_p the specific heat. Following the formulations in

[33,70,79,134–136], the governing equation for ϕ during solidification and dendritic growth can be written as

$$\tau(\mathbf{n},U)\partial_t\phi = \nabla\cdot\left[W^2(\mathbf{n})\nabla\phi\right] + W_0^2\nabla\cdot\mathbf{N} - f'(\phi) - \lambda\left(Mc_\infty U + \theta\right)g'(\phi), \tag{4.3}$$

where the relaxation time $\tau(\mathbf{n}, U)$ and the anisotropic interface width $W(\mathbf{n}) = W_0 a_s(\mathbf{n})$ are both functions of the local normal vector $\mathbf{n}$ that can be calculated as $\mathbf{n} = -\nabla\phi/|\nabla\phi|$, W_0 is the characteristic width, λ is a dimensionless parameter that controls the coupling between the phase field and the concentration and temperature fields, $f'(\phi)$ and $g'(\phi)$ are interpolating functions associated with the double-well potential and the free energy of the bulk, respectively, with a popular choice of $f'(\phi) = -\phi + \phi^3$, $g'(\phi) = (1-\phi^2)^2$ [33,134], M is the scaled magnitude of the liquidus slope $M = -m(1-k)/(L_h / C_p)$, and $\mathbf{N}$ is the anisotropic vector defined as

$$\mathbf{N} = |\nabla\phi|^2 a_s(\mathbf{n})\left[\frac{\partial a_s(\mathbf{n})}{\partial(\partial_x\phi)}, \frac{\partial a_s(\mathbf{n})}{\partial(\partial_y\phi)}, \frac{\partial a_s(\mathbf{n})}{\partial(\partial_z\phi)}\right]^{\mathrm{T}}. \tag{4.4}$$

In most previous PFM models, τ is considered as a function of $\mathbf{n}$ only [134–138], and $\tau(\mathbf{n}) = \tau_0 a_s^2(\mathbf{n})$ was applied with τ_0 a constant and $a_s(\mathbf{n})$ defined as the crystalline anisotropy function [134–136]

$$a_s(\mathbf{n}) = 1 - 3\varepsilon_s + 4\varepsilon_s\sum_{\sigma=x,y,z} n_\sigma^4 = 1 - 3\varepsilon_s + 4\varepsilon_s\sum_{\sigma=x,y,z}(\partial_\sigma\phi)^4 \Big/ |\nabla\phi|^4, \tag{4.5}$$

where ε_s is the anisotropic strength. As pointed out by Ramirez et al. [70] and later also implemented in [88,139–141], for coupled thermosolutal transport problems, τ should also be dependent on the concentration field, i.e.,

$$\tau(\mathbf{n},U) = \tau_0 a_s^2(\mathbf{n})F(U), \tag{4.6}$$

and

$$F(U) = \frac{1}{Le} + Mc_\infty\left[1 + (1-k)U\right], \tag{4.7}$$

where $Le = \alpha/D_l$ is the Lewis number denoting the ratio between the thermal diffusivity α and solutal diffusivity D_l in the liquid phase. This work also implements the generic definition of $\tau(\mathbf{n}, U)$ in Eq. (6) for thermosolutal convection-diffusion problems. It should be noted that most of the previous PFM models for solidification and dendritic growth considered only the effect of heat transfer (i.e., ϕ and θ coupled only, see e.g., [32,135,136]) or solute transfer (i.e., ϕ and U coupled only, e.g., [30,31,33,82,137,138,142]); fully coupled thermosolutal diffusion (without convection) problems were studied in [70,134,139–141], while the dependence of τ on U was not taken into account in [134]. The present PFM model (details presented in Chapter 4.3) is applicable to more general solidification processes involving fully coupled thermosoltual convection-diffusion. It is also worth noting that the present general PFM model reduces to that for (1) ϕ and θ coupled thermal/iso-solutal transport problems with the selection of $Le = 1$, $Mc_\infty = 0$, and (2) ϕ and U coupled solutal/iso-thermal transport problems with $Le \to \infty$, $Mc_\infty = 1-(1-k)\Omega$ and $U = \dfrac{\Omega}{1-(1-k)\Omega}$, where Ω is the imposed solutal "undercooling" relating c_∞ to the equilibrium liquidus concentration at the system temperature c_l^0, i.e.,

$$\Omega = \frac{c_l^0 - c_\infty}{(1-k)c_l^0}, \tag{4.8}$$

It is clear that for both simplified versions, $\tau(\mathbf{n}, U)$ in Eq. (4.6, 4.7) reduces to $\tau(\mathbf{n}) = \tau_0 a_s^2(\mathbf{n})$.

With the above expressions, Eq. (3) can be rewritten in the explicit form as

$$\tau_0 a_s^2(\mathbf{n}) F(U) \partial_t \phi = W_0^2 \nabla \cdot \left[a_s^2(\mathbf{n}) \nabla \phi \right] + W_0^2 \nabla \cdot \mathbf{N} + \left(\phi - \phi^3 \right) - \lambda \left(Mc_\infty U + \theta \right) \left(1 - \phi^2 \right)^2. \tag{4.9}$$

4.2.2 Melt flow

The melt is assumed to be incompressible Newtonian fluid and the flow is governed by the continuity and Navier-Stokes equations

$$\nabla \cdot \mathbf{v} = 0\,, \tag{4.10}$$

$$\partial_t \mathbf{v} + \mathbf{v} \cdot \nabla \mathbf{v} = -\nabla p/\rho + \nu \nabla^2 \mathbf{v}\,, \tag{4.11}$$

where **v** is the flow velocity, p the pressure, ρ the density, and ν the viscosity. For sharp interfaces, the no-slip boundary condition should be used. For diffuse interfaces, however, a volume-averaged momentum equation can be formulated, as shown in [79] in the diffuse interface domain; and with the introduction of the phase field, convenient boundary schemes can be implemented at the diffuse interface, such as treating the interfacial flow as a flow in a porous medium [136]. In this work, the latter approach is applied and the specific interface treatment for flow simulation will be presented in the context of the PFM/LBM model (see Chapter 4.3.2 below).

4.2.3 Concentration field

The governing equation for the concentration field can be written as [31,33,70,134,141,143]

$$p_\phi \left(\partial_t U + \mathbf{v} \cdot \nabla U\right) = \nabla \cdot \left(D_\phi \nabla U\right) - \nabla \cdot \mathbf{j}_{at} + \frac{1+(1-k)U}{2}\partial_t \phi - \nabla \cdot \mathbf{J}\,, \tag{4.12}$$

where $p_\phi = \frac{1+k}{2} - \frac{(1-k)}{2}\phi$, the interpolated diffusivity $D_\phi = D_s \frac{1+\phi}{2} + D_l \frac{1-\phi}{2}$, $\mathbf{j}_{at}$ is the phenomenological anti-trapping current term defined as [134]

$$\mathbf{j}_{at} = -\frac{1}{2\sqrt{2}} W_0 \left[1+(1-k)U\right] \frac{\partial \phi}{\partial t} \frac{\nabla \phi}{|\nabla \phi|}\,, \tag{4.13}$$

and **J** is the flux term associated with fluctuation [33]. The third term on the RHS of Eq. (4.12) is due to the rearrangement of $\partial_t U$ as U is related to ϕ (see Eq. (4.1)). In this work, the flux **J** is neglected following the setups in [70,134,136,137,144] for direct quantitative comparison with results reported therein. It should be stressed that in this work, the solute diffusion within the

solid phase is also taken into account as in [31,33]. This is different from the models in [70,134,141,143] where solute diffusion in the solid was neglected with $D_\phi = D_l \dfrac{1-\phi}{2}$.

4.2.4 Temperature field

The governing equation for the dimensionless temperature considering convection is [70,134,136,141,144]

$$\partial_t \theta + \mathbf{v}\cdot\nabla\theta = \alpha\nabla^2\theta + \frac{1}{2}\partial_t \phi\,, \tag{4.14}$$

where α is the thermal diffusivity, the last term in Eq. (4.14) is related to the latent heat of fusion (see Eq. (4.2)) during phase change, and the coefficient ½ shows up in Eq. (4.14) since the bounds for the phase field variable are $\phi = \pm 1$.

4.3 Present phase-field/lattice-Boltzmann model (PFM/LBM)

4.3.1 LB scheme for phase field

By treating the phase-field equation as a transient pseudo-convection-diffusion equation with source terms, and following the idea originally demonstrated in [145] for solute and heat transfer in heterogeneous porous median, an LB scheme was proposed in [134,135] for the phase field with a modified single-relaxation-time (SRT, also called BGK [146]) collision operator:

$$\begin{aligned} a_s^2(\mathbf{n}) g_\alpha\left(\mathbf{x}+\mathbf{e}_\alpha\delta t, t+\delta t\right) = g_\alpha\left(\mathbf{x},t\right) - \left[1-a_s^2(\mathbf{n})\right] g_\alpha\left(\mathbf{x}+\mathbf{e}_\alpha\delta t, t\right) \\ - \frac{1}{\tau_\phi\left(\mathbf{x},t\right)}\left[g_\alpha\left(\mathbf{x},t\right) - g_\alpha^{\mathrm{eq}}\left(\mathbf{x},t\right)\right] + \omega_\alpha \delta_t G_\phi\left(\mathbf{x},t\right)/\tau_0\,, \end{aligned} \tag{4.15}$$

where $g_\alpha(\mathbf{x}, t) \equiv g(\mathbf{x}, \boldsymbol{\xi}_\alpha, t)$, $\boldsymbol{\xi}$ is the microscopic particle velocity vector in the LB model and it is discretized to a small set of discrete velocities $\{\boldsymbol{\xi}_\alpha | \alpha = 0, 1, \ldots, m-1\}$, $\mathbf{e}_\alpha$ the αth discrete velocity vector, δt the time step, and ω_α the weight coefficient. The distribution function $g_\alpha\left(\mathbf{x}+\mathbf{e}_\alpha\delta t, t\right)$

evaluated at the adjacent nodes is necessary to recover the correct governing equation for ϕ [134,135]. The macroscopic phase-field variable can be obtained from

$$\phi(\mathbf{x},t)=\sum_{\alpha=0}^{m-1} g_\alpha(\mathbf{x},t), \tag{4.16}$$

and the equilibrium distribution was defined as [134,135]

$$g_\alpha^{\mathrm{eq}}(\mathbf{x},t)=\omega_\alpha\left[\phi(\mathbf{x},t)-\frac{1}{\xi}\mathbf{e}_\alpha\cdot\mathbf{N}\frac{W_0^2}{\tau_0}\frac{\delta t}{\delta x}\right], \tag{4.17}$$

with ξ a constant related to the lattice structure (ξ = 1/3 in D2Q5 and ξ = 1/4 in D3Q7 LB models), and the relaxation time coefficient needs to satisfy

$$\tau_\phi(\mathbf{x},t)=\frac{1}{\xi}a_s^2(\mathbf{n})\frac{W_0^2}{\tau_0}\frac{\delta t}{\delta x^2}+\frac{1}{2}. \tag{4.18}$$

The BGK-LB scheme in Eq. (4.15) was also implemented in [136,137], where the authors introduced an "interface advancing velocity" evoked by the interfacial surface energy and it can be expressed as

$$\mathbf{v}_n\equiv-\mathbf{N}\frac{W_0^2}{\tau_0}\frac{\delta t}{\delta x}. \tag{4.19}$$

It is noted that the 2nd-order terms of $O(\mathbf{v}_n^2)$ were also included in the equilibrium distribution in [136,137] – a practice generally considered necessary for modeling fluid flow but not for scalar convection-diffusion [85,87].

Based on the modified BGK scheme in Eq. (4.15) and the discussion in [145] regarding the numerical stability of the modified LB scheme, we present an improved PFM/LBM model in this work for the phase field coupled with thermosolutal convection-diffusion.

First, the phase-field governing equation in (8) is rewritten as

$$\tau_0 a_s^2(\mathbf{n})\partial_t\phi = W_0^2\nabla\cdot\left[\frac{a_s^2(\mathbf{n})}{F(U)}\nabla\phi\right] + W_0^2\nabla\cdot\frac{\mathbf{N}}{F(U)} + \frac{G_\phi}{F(U)}, \tag{4.20}$$

where $G_\phi = \left(\phi-\phi^3\right) - \lambda\left(Mc_\infty U+\theta\right)\left(1-\phi^2\right)^2$. Clearly, in obtaining Eq. (4.20), the assumption of "semi-explicit" coupling was applied, i.e., the coupling of U into the phase-field is mainly through the last source term in Eq. (8), while its coupling in the remaining transient, diffusion and pseudo-convection terms in Eq. (8) is assumed to be weak so that $1/F(U)$ was directly moved into the divergence terms. Such an assumption is acceptable for LB simulations with small enough time steps as demonstrated in Section 4 with numerical examples. For problems with strong coupling between U and ϕ, the present model can still be applicable, one just needs to add those originally neglected terms (related to ∇U) to the combined source term.

The present LB evolution scheme is written as

$$\begin{aligned} a_s^2(\mathbf{n})g_\alpha\left(\mathbf{x}+\mathbf{e}_\alpha\delta t, t+\delta t\right) = g_\alpha\left(\mathbf{x},t\right) - \left[1-a_s^2(\mathbf{n})\right]g_\alpha\left(\mathbf{x}+\mathbf{e}_\alpha\delta t,t\right) \\ -\mathbf{M}^{-1}\mathbf{S}\left[\mathbf{m}\left(\mathbf{x},t\right)-\mathbf{m}^{\mathrm{eq}}\left(\mathbf{x},t\right)\right]_\alpha + \omega_\alpha\delta t\frac{G_\phi\left(\mathbf{x},t\right)}{F(U)\tau_0}, \end{aligned} \tag{4.21}$$

where $\mathbf{M}$ is a transformation matrix to map the distribution functions to the moment space through $\mathbf{m} = \mathbf{M}\cdot\mathbf{g}$ and $\mathbf{m}^{\mathrm{eq}} = \mathbf{M}\cdot\mathbf{g}^{\mathrm{eq}}$, and $\mathbf{S}$ is related to the matrix of relaxation time coefficients with the multiple-relaxation-time (MRT) collision operator applied in Eq. (4.21). We choose the matrices as in [85] and the equilibrium moments can be explicitly obtained as in [86,87]. Specifically, for the D2Q5 MRT-LB model

$$\mathbf{M} = \begin{bmatrix} 1 & 1 & 1 & 1 & 1 \\ 0 & 1 & -1 & 0 & 0 \\ 0 & 0 & 0 & 1 & -1 \\ 4 & -1 & -1 & -1 & -1 \\ 0 & 1 & 1 & -1 & -1 \end{bmatrix}, \ \mathbf{S}^{-1} = \mathrm{diag}\left(\tau_{00}, \tau_\phi, \tau_\phi, \tau_p, \tau_p\right), \quad \text{and} \tag{4.22}$$

$$\mathbf{m}^{\mathrm{eq}} = \left(\phi, u_{nx}, u_{ny}, \frac{2}{3}\phi, 0 \right)^{\mathrm{T}} = \left(\phi, \frac{v_{nx}}{F(U)}, \frac{v_{ny}}{F(U)}, \frac{2}{3}\phi, 0 \right)^{\mathrm{T}}, \text{ in D2Q5,} \tag{4.23}$$

while for the D3Q7 MRT-LB model, the following can be similarly obtained

$$\mathbf{M} = \begin{bmatrix} 1 & 1 & 1 & 1 & 1 & 1 & 1 \\ 0 & 1 & -1 & 0 & 0 & 0 & 0 \\ 0 & 0 & 0 & 1 & -1 & 0 & 0 \\ 0 & 0 & 0 & 0 & 0 & 1 & -1 \\ 6 & -1 & -1 & -1 & -1 & -1 & -1 \\ 0 & 2 & 2 & -1 & -1 & -1 & -1 \\ 0 & 0 & 0 & 1 & 1 & -1 & -1 \end{bmatrix}, \mathbf{S}^{-1} = \mathrm{diag}\left(\tau_{00}, \tau_{\phi}, \tau_{\phi}, \tau_{\phi}, \tau_{p}, \tau_{p}, \tau_{p} \right), \text{ and} \tag{4.24}$$

$$\mathbf{m}^{\mathrm{eq}} = \left(\phi, u_{nx}, u_{ny}, u_{nz}, \frac{3}{4}\phi, 0, 0 \right)^{\mathrm{T}} = \left(\phi, \frac{v_{nx}}{F(U)}, \frac{v_{ny}}{F(U)}, \frac{v_{nz}}{F(U)}, \frac{3}{4}\phi, 0, 0 \right)^{\mathrm{T}}, \text{ in D3Q7.} \tag{4.25}$$

Remark 1. It should be emphasized that in deriving $\mathbf{m}^{\mathrm{eq}}$ in Eqs. (4.23, 4.25), the equilibrium distribution function is rescaled in the present model as

$$\begin{aligned} g_{\alpha}^{\mathrm{eq}}(\mathbf{x},t) &= \omega_{\alpha}\left[\phi(\mathbf{x},t) + \frac{1}{\xi}\mathbf{e}_{\alpha}\cdot\mathbf{u}_{n} \right] = \omega_{\alpha}\left[\phi(\mathbf{x},t) + \frac{1}{\xi}\mathbf{e}_{\alpha}\cdot\frac{\mathbf{v}_{n}}{F(U)} \right] \\ &= \omega_{\alpha}\left[\phi(\mathbf{x},t) - \frac{1}{\xi}\mathbf{e}_{\alpha}\cdot\mathbf{N}\frac{W_0^2}{F(U)\tau_0}\frac{\delta t}{\delta x} \right], \end{aligned} \tag{4.26}$$

where $\mathbf{u}_n \equiv \dfrac{\mathbf{v}_n}{F(U)}$ with $\mathbf{v}_n$ defined in Eq. (4.19). Additionally, in the relaxation matrices in Eqs. (4.22, 4.24), the relaxation coefficient τ_ϕ related to the diffusion coefficient also needs rescaling to satisfy the following

$$\tau_{\phi}(\mathbf{x},t) = \frac{1}{\xi}\frac{a_s^2(\mathbf{n})}{F(U)}\frac{W_0^2}{\tau_0}\frac{\delta t}{\delta x^2} + \frac{1}{2}. \tag{4.27}$$

The other relaxation coefficients do not affect the leading-order numerical solutions and thus τ_{00} = τ_P = 1 is used for consistency [14,86,87].

Remark 2. The proposed MRT-LB model for the phase field evolution is able to significantly improve the numerical stability with two combined features. First, it is well known that the LB models with an MRT collision operator generally have better numerical accuracy and stability compared to those with the BGK operator in both fluid flow and scalar transport simulations [25,85,87,147,148]. Therefore, the present MRT-LB scheme in Eq. (4.21) is considered an improvement from the BGK-LB scheme in Eq. (4.15). Second, the rearrangement of the governing equation in Eq. (4.20) and the rescaling of the corresponding equilibria, relaxation coefficients and source term (see Eqs. (4.21, 4.23, 4.25, 4.26, 4.27)) are crucial in ensuring the numerical stability especially for high Lewis number (*Le*) problems. While one could keep the original governing equation in (4.9), combine $F(U)$ with $a_s^2(\mathbf{n})$, and construct similar LB scheme as in Eq. (4.15) such as

$$a_s^2(\mathbf{n})F(U)g_\alpha\left(\mathbf{x}+\mathbf{e}_\alpha\delta_t,t+\delta_t\right)=g_\alpha\left(\mathbf{x},t\right)-\left[1-a_s^2(\mathbf{n})F(U)\right]g_\alpha\left(\mathbf{x}+\mathbf{e}_\alpha\delta_t,t\right)$$
$$-\frac{1}{\tau_\phi\left(\mathbf{x},t\right)}\left[g_\alpha\left(\mathbf{x},t\right)-g_\alpha^{\mathrm{eq}}\left(\mathbf{x},t\right)\right]+\omega_\alpha\delta_t G_\phi\left(\mathbf{x},t\right)/\tau_0, \quad (4.28)$$

in Eq. (4.28) no rescaling is needed for g_α^{eq}, τ_ϕ or G_ϕ, and it can be verified to recover Eq. (4.9) up to 2nd-order accuracy; the LB scheme in Eq. (4.28) would become unstable when the magnitude of $F(U)$ is small (noting that $a_s^2(\mathbf{n})$ is of $O(1)$ and $F(U) \sim 1/Le$ in Eq. (4.7)) since the RHS of Eq. (4.28) will be divided by $a_s^2(\mathbf{n})F(U)$ when updating $g_\alpha\left(\mathbf{x}+\mathbf{e}_\alpha\delta_t,t+\delta_t\right)$. This phenomenon was also reported in detail in [145] for low-porosity simulations. Furthermore, it should be noted that as pointed out in [70], in typical solidification of alloys the solutal diffusivity in the liquid state is generally much smaller than the thermal diffusivity (i.e., $Le = \alpha/D >> 1$). Thus small $F(U)$ is encountered in typical alloy solidification processes. Overall, the present PFM/LBM model is well-poised to simulate solidification and dendritic growth with both

high- and low-Lewis numbers with improved numerical stability compared to those previous PFM-LBM models.

Remark 3. Accurate and efficient computation of the gradient $\nabla\phi$ is essential in the PFM as it shows up in several different terms (e.g., the normal vector $\mathbf{n} = -\nabla\phi/|\nabla\phi|$, the anisotropy function $a_s(\mathbf{n})$ in Eq. (4.5), and the anisotropic vector $\mathbf{N}$ in Eq. (4.4)). As demonstrated in [87,110], in the LB framework, the scalar gradient can be conveniently computed from the distribution functions. Using the notations in this work, the scheme becomes

$$\frac{\partial\phi}{\partial x_i} = -\frac{1}{\xi\tau_\phi\delta x}\sum_{\alpha=1}^{m-1} e_{\alpha i} g_\alpha^{\text{neq}}, \tag{4.29}$$

where $g_\alpha^{\text{neq}} = g_\alpha - g_\alpha^{\text{eq}}$ is the non-equilibrium component of the distribution function. It is emphasized that Eq. (4.29) is a local scheme, i.e., it requires only the populations at the local lattice node and is thus more efficient than using finite-difference schemes that were used in previous PFM models. The second-order accuracy of the scheme in Eq. (4.29) has been verified in [87,110].

The Chapman-Enskog analysis for the LB evolution equation (4.21) to recover the phase-field governing equation (4.20) is presented in Appendix A.

For efficient computation and storage, the LB evolution equation (4.21) is solved in two steps:

collision step:

$$\hat{g}_\alpha(\mathbf{x},t) = \frac{1}{a_s^2(\mathbf{n})}\left\{\begin{array}{l} g_\alpha(\mathbf{x},t) - \left[1 - a_s^2(\mathbf{n})\right] g_\alpha(\mathbf{x}+\mathbf{e}_\alpha\delta t, t) \\ -\left[\mathbf{M}^{-1}\mathbf{S}\cdot\left(\mathbf{m}-\mathbf{m}^{\text{eq}}\right)(\mathbf{x},t)\right]_\alpha + \omega_\alpha\delta t\dfrac{G_\phi(\mathbf{x},t)}{F(U)\tau_0} \end{array}\right\}, \text{ and} \tag{4.30}$$

streaming step:

$$g_\alpha\left(\mathbf{x}+\mathbf{e}_\alpha\delta t, t+\delta t\right)=\hat{g}_\alpha\left(\mathbf{x},t\right), \tag{4.31}$$

where $\hat{g}_\alpha$ represents the post-collision state.

4.3.2 LB scheme for melt flow

The incompressible melt flow in the liquid phase can be simulated with the widely used D3Q19 and D2Q9 MRT-LB models [147,148]. In the diffuse interface, the flow can be considered as porous medium flow. To avoid tracking the sharp interface with no-slip boundary condition, we adopt the gray LB scheme [149–151] for porous medium flows to handle the diffuse interface. The collision-streaming procedure for melt flow becomes

collision step:

$$\hat{f}_\alpha\left(\mathbf{x},t\right)=f_\alpha\left(\mathbf{x},t\right)-\left[\mathbf{M}^{-1}\mathbf{S}\cdot\left(\mathbf{m}-\mathbf{m}^{\mathrm{eq}}\right)\left(\mathbf{x},t\right)\right]_\alpha, \text{ and} \tag{4.32}$$

streaming step:

$$f_\alpha\left(\mathbf{x}+\mathbf{e}_\alpha\delta_t, t+\delta_t\right)=\hat{f}_\alpha\left(\mathbf{x},t\right)+\theta_f\left(\mathbf{x}+\frac{1}{2}\mathbf{e}_\alpha\delta_t,t\right)\left[\hat{f}_{\bar{\alpha}}\left(\mathbf{x}+\mathbf{e}_\alpha\delta_t,t\right)-\hat{f}_\alpha\left(\mathbf{x},t\right)\right], \tag{4.33}$$

where the details of the matrices **M**, **S** and the equilibrium moments $\mathbf{m}^{\mathrm{eq}}$ can be found in [147,148] and are not shown here for brevity, and the subscript $\bar{\alpha}$ denotes the opposite direction of α (i.e., $\mathbf{e}_{\bar{\alpha}}=-\mathbf{e}_\alpha$). The fraction coefficient θ_f is related to the solid fraction that can be calculated from the phase-field variable ($\theta_f=(\phi+1)/2$) and is evaluated at the midpoint of the link in Eq. (4.33), i.e.,

$$\theta_f\left(\mathbf{x}+\frac{1}{2}\mathbf{e}_\alpha\delta_t,t\right)=\frac{\theta_f\left(\mathbf{x},t\right)+\theta_f\left(\mathbf{x}+\mathbf{e}_\alpha\delta_t,t\right)}{2}=\frac{\phi\left(\mathbf{x},t\right)+\phi\left(\mathbf{x}+\mathbf{e}_\alpha\delta_t,t\right)+2}{4}. \tag{4.34}$$

The LB scheme for melt flow in Eq. (4.32, 4.33) and the calculation of the macroscopic variables including density and velocity are applicable to the entire computational domain under

the PFM/LBM framework. Specifically, all the terms in Eq. (4.33) are considered within the diffuse interface region; additionally, it reduces to the standard LB scheme for fluid flow within the melt at $\theta_f = (\phi+1)/2 = 0$, and to the bounce-back scheme which represents the no-slip condition within the solid phase at $\theta_f = 1$. Similar discussion was also presented by Sun et al. [136], however, it should be noted that in [136] the pre-collision distribution functions $f_{\bar{\alpha}}(\mathbf{x}+\mathbf{e}_\alpha\delta_t,t)$ and $f_\alpha(\mathbf{x},t)$ were used in the last term in Eq. (4.33). To correctly recover the governing equations for flow in porous media, post-collision terms as shown in Eq. (4.33) should be used. One can refer to [149] for a detailed comparison of the various LB schemes for porous media flow and their Chapman-Enskog analyses.

For dendritic growth modeling with melt flow and dendrite movement under external forces (e.g., gravity or buoyance forces as in [33,142,152]), the body forces can be conveniently added in the LB scheme in Eq. (4.32, 4.33) using standard body force treatments in the LB model. Thus the PFM/LBM model is an attractive and powerful tool for large scale simulations of solidification processes with motion of multiple dendrites [142,152].

4.3.3 LB scheme for concentration field

To apply the LB method to solve for the concentration (supersaturation) field, the governing equation (4.12) is reorganized to an anisotropic convection-diffusion equation (CDE) with a general source term

$$\partial_t U + \mathbf{v}\cdot\nabla U = \nabla\cdot\left(D_{eff}\nabla U\right) + G_U\,, \tag{4.35}$$

where $D_{eff} = \dfrac{D_\phi}{p_\phi} = \dfrac{(1+\phi)D_s + (1-\phi)D_l}{(1+k)-(1-k)\phi}$, and the combined source term becomes

$$G_U = -\frac{(1-k)\left[(1+\phi)D_s + (1-\phi)D_l\right]}{\left[(1+k)-(1-k)\phi\right]^2}\nabla U\cdot\nabla\phi + \frac{\left[1+(1-k)U\right]\partial_t\phi - 2\nabla\cdot\mathbf{j}_{at}}{(1+k)-(1-k)\phi}\,. \tag{4.36}$$

It is noted that $\nabla\left(p_\phi^{-1}\right)=\dfrac{2(1-k)}{\left[(1+k)-(1-k)\phi\right]^2}\nabla\phi$ was used in deriving Eq. (4.36). In this work, the CDE in (4.35) will be solved with the D2Q5/D3Q7 MRT-LB models [85,87]. By introducing the set of distribution functions $h_\alpha(\mathbf{x}, t)$, the dimensionless concentration is obtained from $U(\mathbf{x},t)=\sum_{\alpha=0}^{m-1}h_\alpha(\mathbf{x},t)$, and the collision-streaming procedure for the LB evolution equation includes

collision step:

$$\hat{h}_\alpha(\mathbf{x},t)=h_\alpha(\mathbf{x},t)-\left[\mathbf{M}^{-1}\mathbf{S}\cdot\left(\mathbf{m}-\mathbf{m}^{\mathrm{eq}}\right)(\mathbf{x},t)\right]_\alpha+\omega_\alpha\delta t G_U(\mathbf{x},t), \text{ and} \tag{4.37}$$

streaming step:

$$h_\alpha\left(\mathbf{x}+\mathbf{e}_\alpha\delta t,t+\delta t\right)=\hat{h}_\alpha(\mathbf{x},t). \tag{4.38}$$

The matrices **M** and **S** are the same as those in Section 3.1 and the details of equilibrium moment $\mathbf{m}^{\mathrm{eq}}$ can be found in [85,87]. It is worth noting that the principal relaxation time coefficients are related to the effective diffusion coefficient through $\tau_U=3D_{eff}+0.5$. With the MRT collision operator implemented, the present LB model is stable in handling solutal convection-diffusion with very large diffusivity ratios. Numerical verification with $D_l/D_s = 10^4$ will be presented in Section 4.3. Some additional remarks are given below.

First, the present LB model for solute convection-diffusion is considered much more convenient and easier to implement than the LB model proposed in [134], where $D_{eff}=\dfrac{(1-\phi)D_l}{(1+k)-(1-k)\phi}$ was assumed neglecting diffusion in the solid phase. As a consequence, in order to apply the LB model to the entire domain for U evolution, the relaxation coefficient τ_U was chosen to be related to the D_l even within the solid phase; and additional rearrangement of

the governing equation for U as well as redefinition of the equilibrium distribution function were used in [134]. The present LB model avoids those complex steps and is able to model diffusion within the solid as well.

Second, similar to computing $\nabla\phi$ in the LB model, the gradient ∇U is also conveniently obtained from a local scheme similar to that in Eq. (4.29) based on the distribution functions in the LB model. It is also noted that, however, for computing $\nabla\cdot\mathbf{j}_{at}$ in Eq. (4.36), one has to adopt conventional schemes (the central-difference scheme is applied in this work) as in all previous PFM models. And the simple forward Euler method, $\partial_t\phi=\dfrac{\phi(\mathbf{x},t)-\phi(\mathbf{x},t-\delta t)}{\delta t}$, is used for computing $\partial_t\phi$ in the combined source term in Eq. (4.36).

4.3.4 LB scheme for temperature field

The energy equation (4.14) can also be considered as a standard CDE with a source term ($G_\theta=\dfrac{1}{2}\partial_t\phi$) and the above D2Q5/D3Q7 MRT-LB models [85,87] will also be implemented for the temperature field evolution. For completeness, the collision-streaming procedure is also shown below where $n_\alpha(\mathbf{x}, t)$ is the last set of distribution function defined to yield

$$\theta(\mathbf{x},t)=\sum_{\alpha=0}^{m-1}n_\alpha(\mathbf{x},t)$$

collision step:

$$\hat{n}_\alpha(\mathbf{x},t)=n_\alpha(\mathbf{x},t)-\left[\mathbf{M}^{-1}\mathbf{S}\cdot\left(\mathbf{m}-\mathbf{m}^{\mathrm{eq}}\right)(\mathbf{x},t)\right]_\alpha+\omega_\alpha\delta t G_\theta(\mathbf{x},t),\ \text{and} \tag{4.39}$$

streaming step:

$$n_\alpha\left(\mathbf{x}+\mathbf{e}_\alpha\delta t,t+\delta t\right)=\hat{n}_\alpha(\mathbf{x},t). \tag{4.40}$$

The flow chart for the present PFM/LBM model for solidification and dendritic growth simulation with fully coupled melt flow and thermosolutal convection-diffusion is depicted in Figure 4.1.

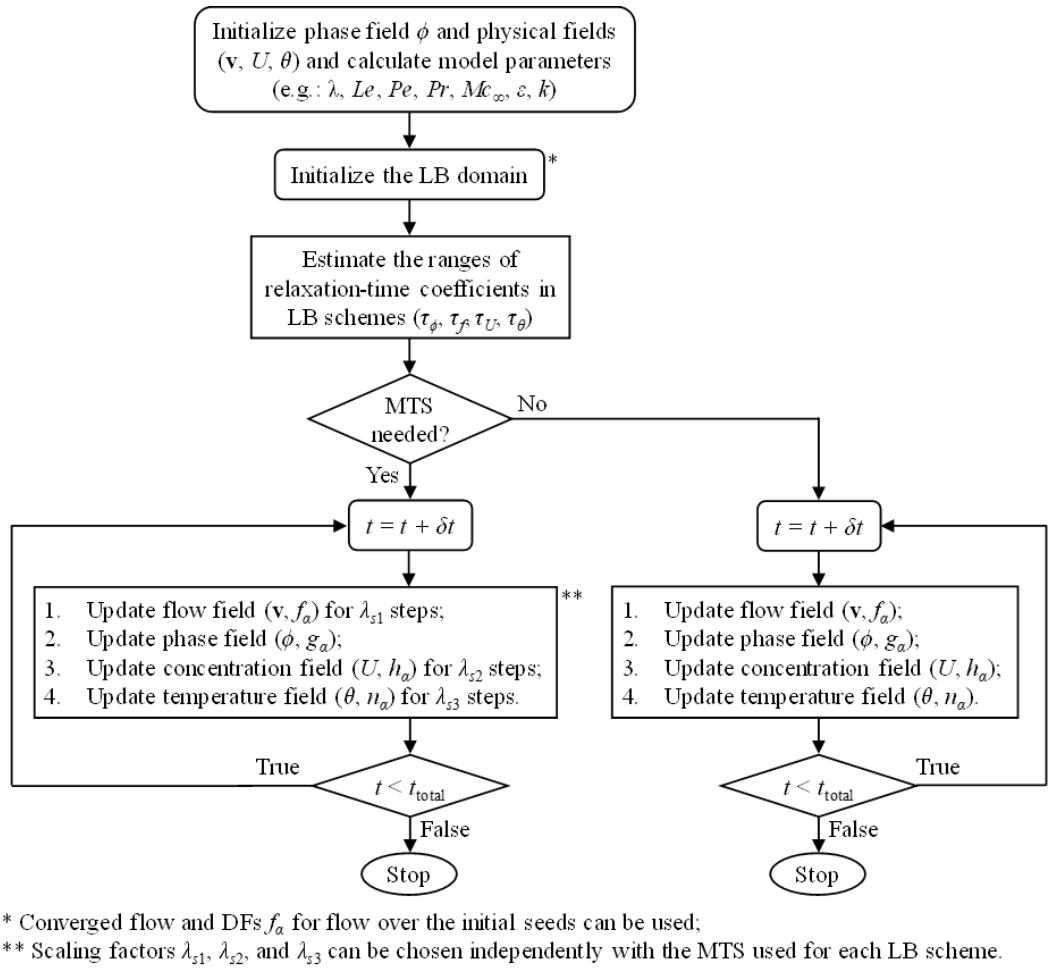

Figure 4.1 Flow chart for the proposed fully coupled PFM/LBM model. Here MTS represents the multiple-time-scaling (MTS) strategy developed in [40].

4.4 Numerical verification and discussion

In this section, we implement the present PFM/LBM model to simulate four representative solidification problems with coupled melt flow and thermosolutal convection-

diffusion. The applicability and accuracy of the proposed model is verified through detailed comparison of the simulated results with published data in the literature. In each test, a single circular/spherical solid seed of radius R_s is initially placed in the center of a 2D/3D domain with an initial phase-field distribution $\phi_0 = \tanh\left[\left(R_s - d_s\right)/\sqrt{2W_o}\right]$, where d_s is the distance from the seed center; solidification and dendritic grow under various melt flow, heat, and solute transport conditions are simulated. Specifically, the first test focuses on iso-solutal solidification in 2D with the coupled melt flow, phase field, and temperature field evolution simulated; the second test is for isothermal solidification in 2D; fully coupled thermosolutal convection-diffusion in 2D is simulated in the third test; and 3D simulations are presented in the fourth test. The evolution of the phase field, melt flow, concentration (supersaturation) and temperature fields is checked for each case, and quantitative verification of the simulated results in terms of tip velocity and radius, and selected concentration/temperature profiles is presented. The details for accurate computation of the tip velocity and radius based on the solved phase field are given in Appendix B.

4.4.1 Thermal/iso-solutal dendritic solidification in 2D

The 2D computational domain is shown in Figure 4.2, where the domain size is set as a square with $512\delta x \times 512\delta x$ grid resolution and the initial seed radius is $R_s = 10\delta x$. The characteristic parameters for convection-diffusion are $Pe_\alpha = \frac{W_0^2}{\alpha\tau_0} = 0.25$ and $Pr = \nu/\alpha = 23.1$, and the inlet velocity is set as $u_{in} = W_0/\tau_0$ for convection and $u_{in} = 0$ for pure diffusion problems. The length and time scales are controlled by selected interface thickness $W_0 = 2.5\delta x$ and reference time $\tau_0 = 125\delta t$ with unit spatial and time steps ($\delta x = \delta t = 1$) in the LB framework. To simulate the coupled thermal/iso-solutal solidification and be consistent with reported simulations in the

literature, the parameters in the PFM model are chosen as $Le = 1$, $Mc_\infty = 0$, $\varepsilon_s = 0.05$ and $\lambda = a_1 W_0/d_0 = 6.3826$ with constant $a_1 = 0.8839$. Under the above parameter settings, the relaxation coefficient in the thermal LB model is $\tau_g = 1.1$ which results in $\tau_{f,original} = 14.36$ in the hydrodynamic LB model if the same time scaling is utilized. Such a large relaxation coefficient would lead to instability of the model and/or large numerical error. Therefore, we implement the multiple-time-scaling (MTS) strategy in [153] and decouple the time steps in the LB models. The effect of this scaling factor, $\lambda_s = \dfrac{\tau_{f,\text{original}} - 0.5}{\tau_{f,\text{scaled}} - 0.5}$, is studied in Figure 4.2 below, and for all the other results presented $\lambda_s = 15$ was used, which would render $\tau_{f,scaled} = 1.424$.

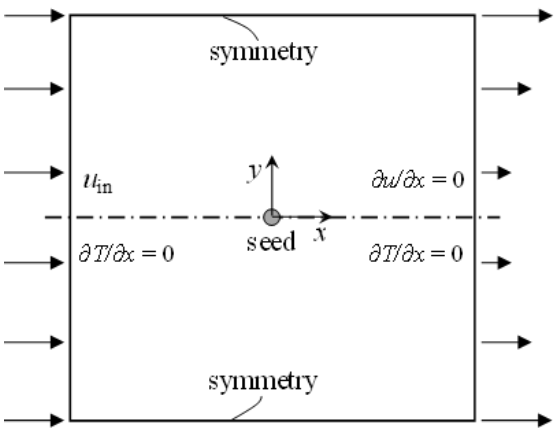

Figure 4.2 Schematic depiction of the square computational domain for dendritic growth with melt convection with boundary conditions specified on all four walls and a circular seed located at the center.

Place all detailed caption, notes, reference, legend information, etc here

Dendritic solidification under pure diffusion is considered first. Figure 4.3 shows the phase field interface ($\phi = 0$) at different times with both the BGK- and MRT-LB models for the phase-field evolution implemented (see Chapter. 4.2.1). Excellent agreement between the results from the two LB models in Fig. 4.3 and also between the present results and those in previous

studies [134,136] is observed, confirming the accuracy of the proposed MRT-LB model for the phase field in this work. The results from the MRT-LB model are thus shown throughout this paper. Furthermore, the dimensionless temperature contours and the phase-field "advancing velocity" (see Eq. (4.19)) components in *x*- and *y*-directions are shown in Figures 4.4 and 4.5, respectively, at the time of $t/\tau_0 = 128$.

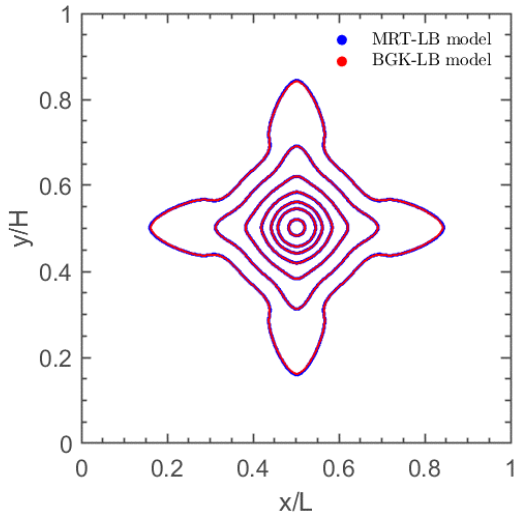

Figure 4.3 Interface evolution comparison between the MRT- and BGK-LB models for the phase field for 2D dendritic growth with pure diffusion at $t/\tau_0 = 0$, 4, 8, 16, 32, 64, 128.

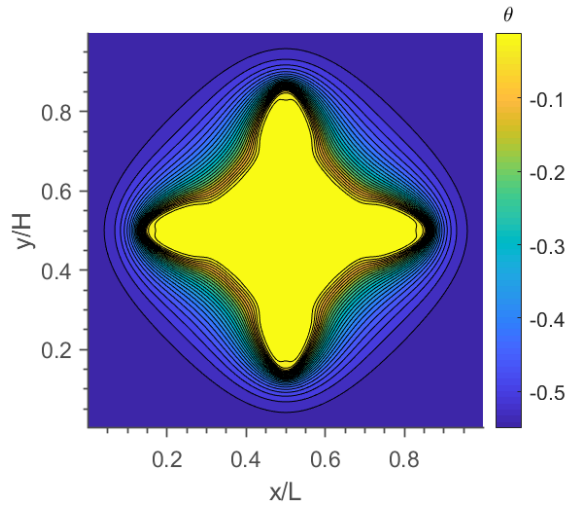

Figure 4.4 Contours of the temperature field for 2D dendritic growth with pure diffusion at $t/\tau_0 = 128$.

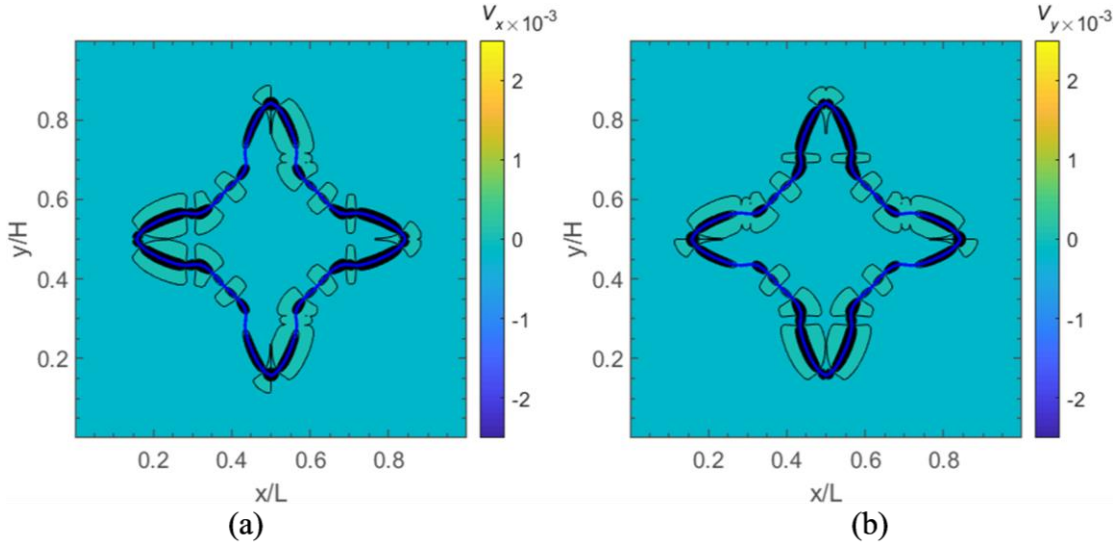

Figure 4.5 Interface advancing velocity contours in (a) *x*-direction and (b) *y*-direction for 2D dendritic growth with pure diffusion at $t/\tau_0 = 128$.

The velocity contours in Figure 4.5 clearly show that the advancing velocities are much more significant in the diffuse interface region compared to the rest of the domain. It should be noted that the velocity components are evaluated at the LBM nodes with the convenient local

scheme in the LBM framework (see Eq. (4.29)); this allows direct and quantitative investigation of the diffuse interface growth at different locations of interest in addition to the tip velocities that were studied in previous publications. To further verify the present model, Figure 4.6 compares the tip velocity and radius results with those reported in [134,136].

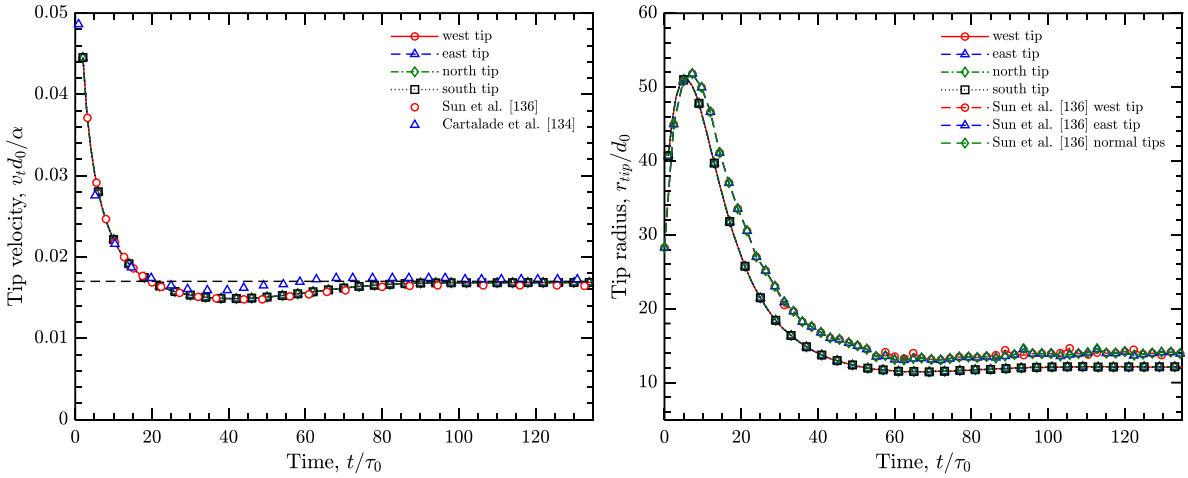

Figure 4.6 Evolution of (a) tip velocities, and (b) tip radii for 2D dendritic growth with pure diffusion.

The computed values at the four tips are the same for pure diffusion case, confirming the self-consistence of the model and simulation results. Good agreement for the tip velocity with those in [134,136] and the steady-state analytical value (dashed line) is observed in Figure 4.6a; and our simulation shows smoother and more consistent tip radius data in Figure 4.6b compared to Sun et al.'s [136], where the tips showed fluctuating results.

Next, we report the simulation results for the 2D dendritic solidification with both thermal convection and diffusion. Figure 4.7 shows the interface comparison at the same times as in Figure 4.3. It is clearly observed that convection plays a significant role on the dendrite

growth, with the west (upstream) tip becoming much larger than the other tips. Consistent results are obtained from both BGK- and MRT-LB models with some discrepancy noticed at the west tip at t/τ_0 = 128. The respective contours of the temperature field and the phase-field advancing velocity components under convection at t/τ_0 = 128 are shown in Figures 4.8 and 4.9, where the effect of thermal convection is obvious compared to those in Figures 4 and 5. In addition, the evolution of the tip velocities and radii is presented in Figure 10. The tip velocity comparison further illustrates the significant influence of the fluid flow and thermal convection on the dendrite growth: the upstream west tip has much higher growth velocity and the downstream east tip lower velocity compared to the symmetric north and south tips perpendicular to the inlet flow; and excellent agreement with those reported in [136] is observed. The evolution of the radii of the four tips is close to each other, and also in good agreement with that in [136]. Consistent with the comparison in Figure 4.6b, our model and tip radius evaluation scheme (see Appendix B) yield improved results compared to those in [136].

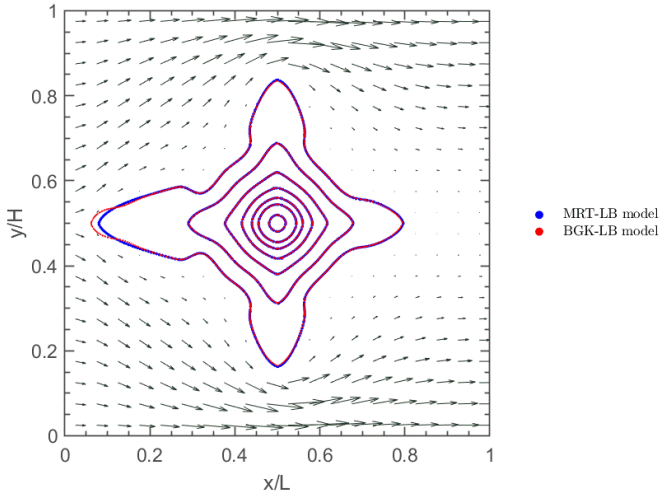

Figure 4.7 Interface evolution comparison between the MRT- and BGK-LB models for the phase field for 2D dendritic growth with convection-diffusion at t/τ_0 = 0, 4, 8, 16, 32, 64, 128. The melt flow velocity vectors are shown at t/τ_0 = 128.

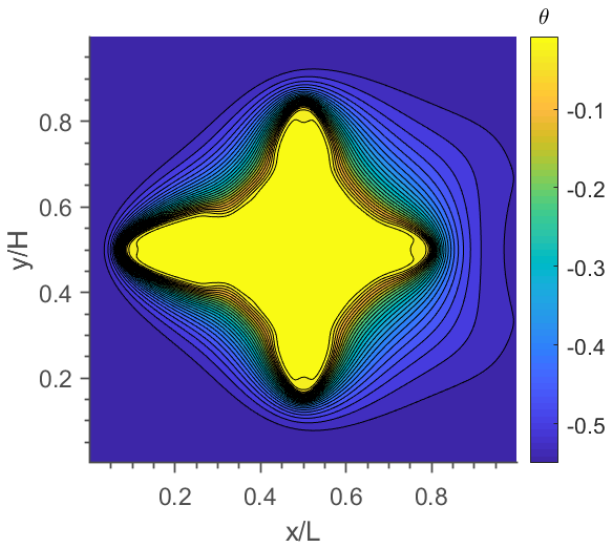

Figure 4.8 Contours of temperature field for 2D dendritic growth with convection-diffusion at $t/\tau_0 = 128$.

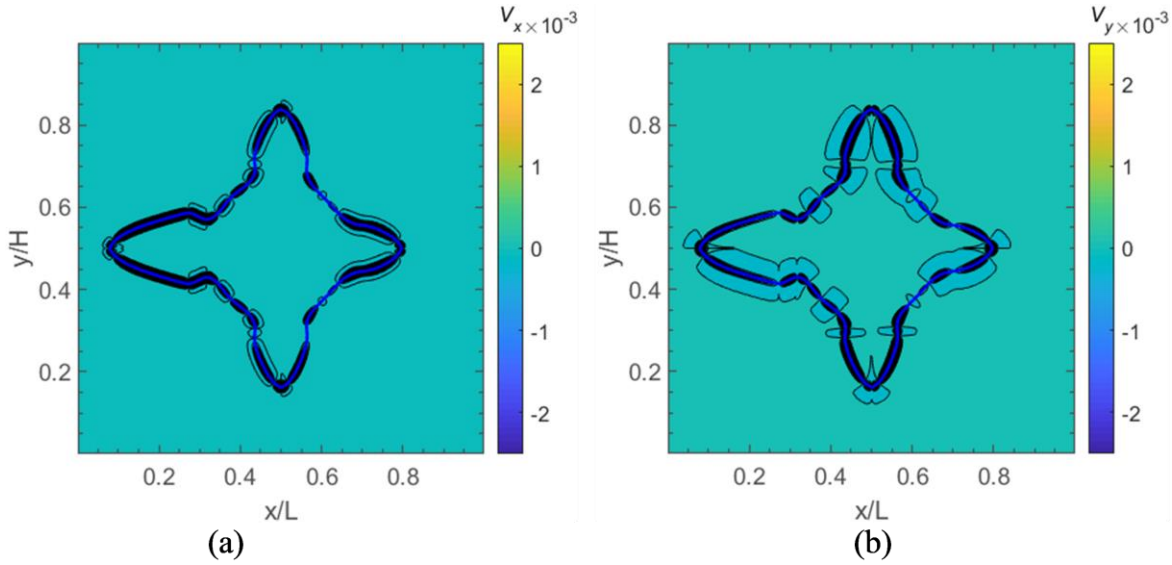

Figure 4.9 Interface advancing velocity contours for 2D dendritic growth with convection-diffusion at $t/\tau_0 = 128$.

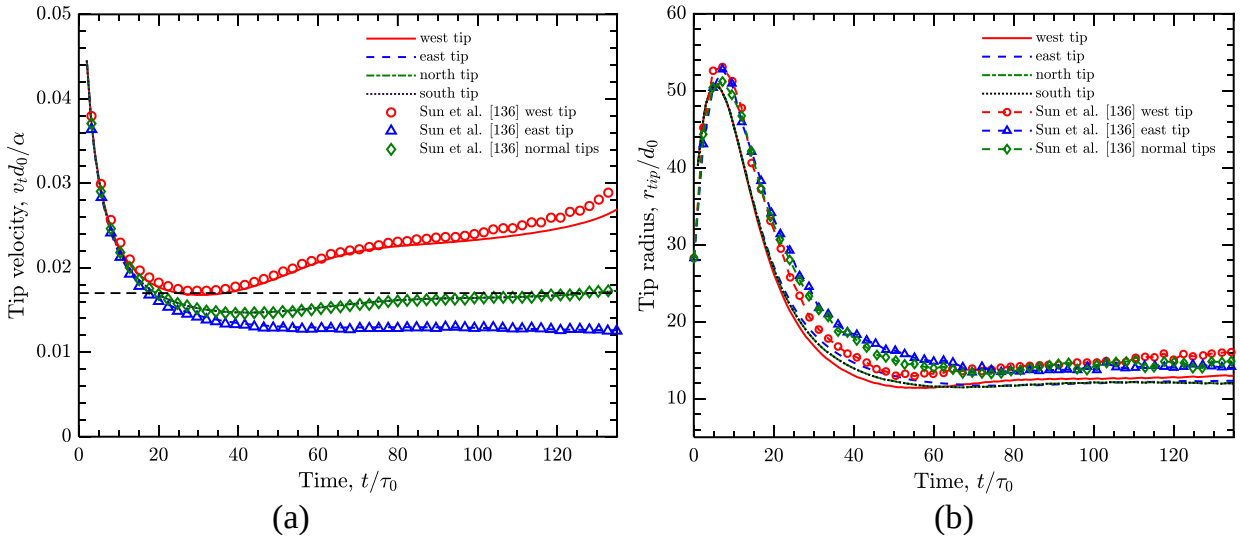

Figure 4.10 Evolution of (a) tip velocities and (b) tip radii for 2D dendritic growth with convection-diffusion.

Furthermore, the efficacy of the multiple-time-scaling (MTS) strategy, which is critical in decoupling the time steps in the different LB schemes in the coupled PFM/LBM model, is demonstrated in Figure 4.11, where the comparison of the tip growth velocities and radii at different scaling factor λ_s values is shown. With the selected Prandtl number Pr = 23.1, the rescaled relaxation-time coefficients for the melt flow are $\tau_{f,scaled}$ = 1.424, 0.962, and 0.731 at λ_s = 15, 30, and 60, respectively. In general, very good agreement can be observed in both tip velocity and radius results in Figure 4.11, confirming the applicability and accuracy of the MTS scheme.

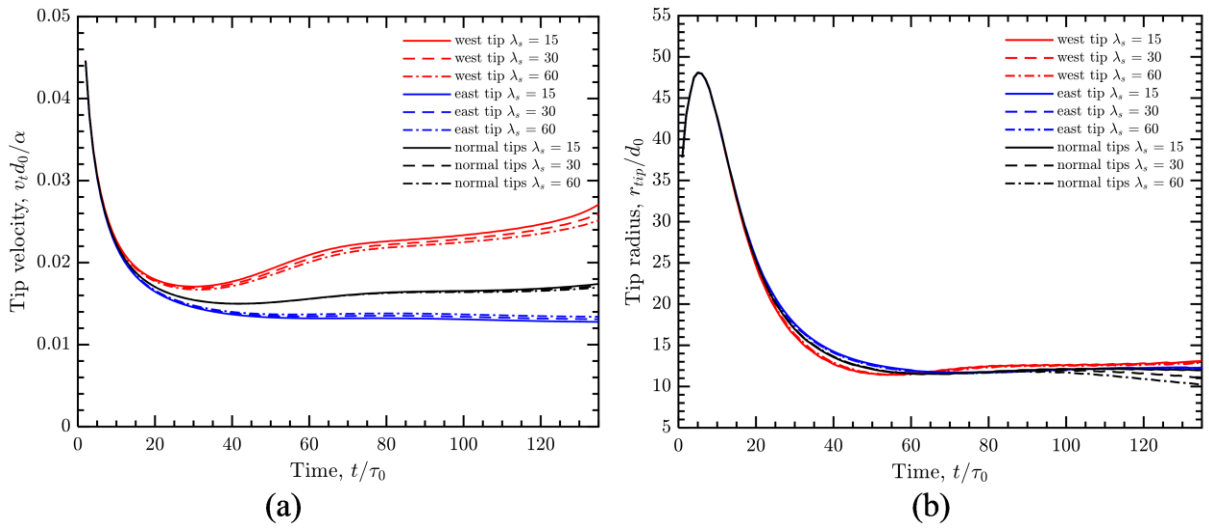

Figure 4.11 Comparison of the (a) tip velocities and (b) tip radii with the multiple-time-scaling (MTS) strategy implemented using various λ_s values for 2D dendritic growth with convection-diffusion.

4.4.2 Solutal/iso-thermal dendritic solidification in 2D

The 2D MRT-LB schemes for the phase field coupled with the concentration field is verified in this section with the 2D isothermal solidification problem with pure diffusion that has been studied by various authors such as Karma [138] with the finite-difference Euler method, Cartalade et al. [134] using the BGK-LB schemes for both fields, and Wang et al. [137] with a hybrid BGK-LB/finite-volume method for the respective phase field and concentration field. In present simulations, the scaled solute mass diffusivity is selected as $\tilde{D}_l = D_l \tau_0 / W_0^2 = 2$ with interface thickness $W_0 = 2.5\delta x$ and constant time scale $\tau_0 = 50\delta t$. The ratio of the solutal diffusivity in solid to liquid is $D_s/D_l = 10^{-4}$ in all cases considered including the following Chapter 4.4.3. Other model parameters include $\lambda = 3.1913$, intial dimensionless cocentration $\Omega_0 = -0.55$ (see Eq. (6)), $\theta = 0$, $k = 0.15$, $\varepsilon_s = 0.02$, and $Mc_\infty = 0.5325$. The computation domian has a $1000\delta x \times 1000\delta x$ uniform mesh and with an initial seed radius $R_s = 10\delta x$.

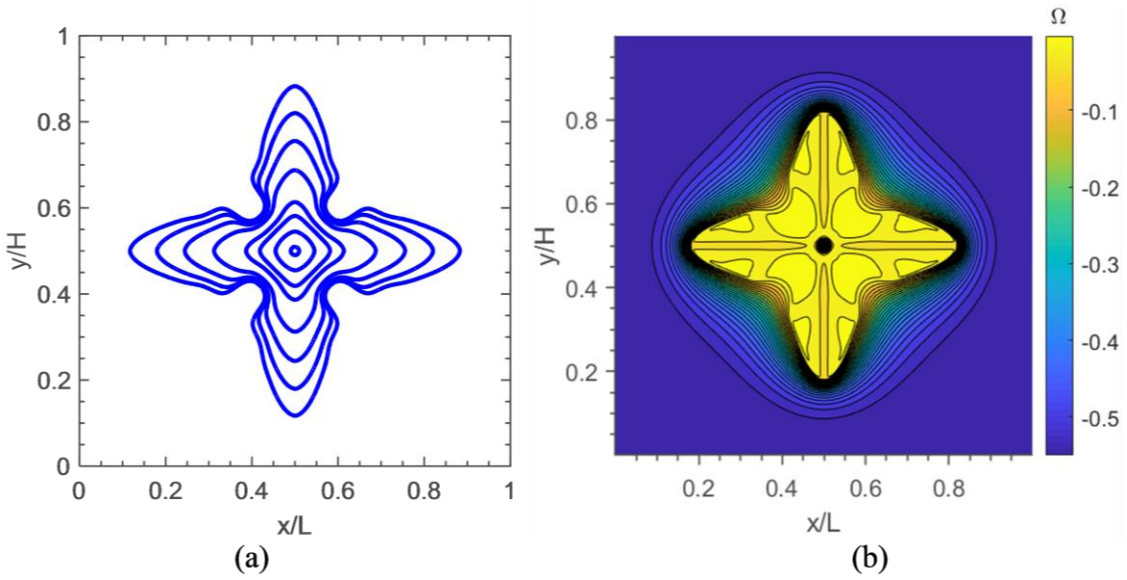

Figure 4.12 (a) Phase-field interface evolution at t/τ_0 = 0, 40, 120, 200, 400, 600, 800, and 1000, and (b) concentration field at t/τ_0 = 800 for the 2D dendritic growth with pure diffusion.

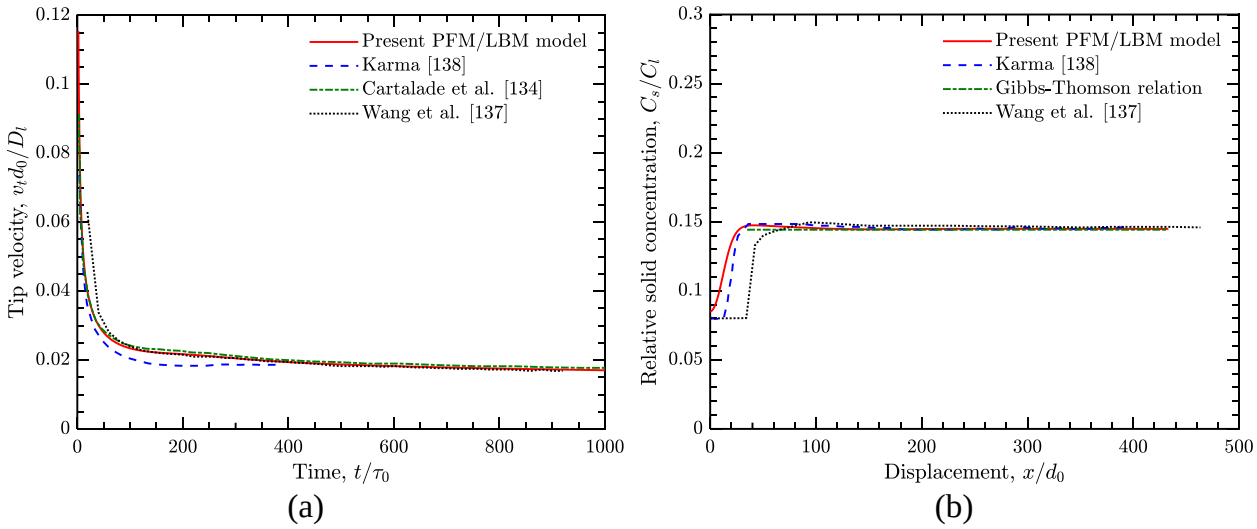

Figure 4.13 (a) Dendritic tip velocity variation and (b) concentration profile in the solid phase for the 2D isothermal dendritic growth with solute diffusion.

The interface morphology of ϕ at different times and the distribution of Ω at t/τ_0 = 800 are shown in Figure 4.12. The results are consistent with those reported in [70,134,137]. It should be noted that different from the previous models [70,134,137] where D_l = 0 was assumed, the

present model also considers the solutal transfer within the solid phase ($D_s/D_l = 10^{-4}$), therefore the concentration gradient on the solid side can be clearly observed in Figure 12b. To quantify the comparison with published results, Figure 4.13a shows the variation of simulated tip velocity and Figure 4.13b the central solute profiles along the *y*-axis in the solid at $t/\tau_0 = 800$. Due to the symmetry of the pure diffusion case, we only present the results of the north tip in Fig. 4.13; and the solute profile obtained from the Gibbs-Thomson relation $C_s / C_l = k[1-(1-k)d_0 / r_{tip}]$, where r_{tip} is the dendritic tip radius ($r_{tip} = 21.996\delta x$ with the present bi-cubic interpolation used), is also included in Figure 4.13b. Good agreement with published results is observed for both the tip velocity and solute profile in Figure 4.13, confirming the accuracy of the present PFM/LBM model for isothermal solidification simulations. The discrepancies in the solute profiles near the dendrite center might be caused by (1) different initial seed radii used in the various simulations (e.g., $R_s = 10\delta x = 14.4d_0$ in present simulation, $R_s = 22d_0$ in [138], and R_s not specified in [137]), and (2) slightly higher relative concentration at the center ($C_s/C_l = 0.085$ in present) than the reference value $C_s/C_l = 0.08$ in [137,138] since the present model considers non-zero diffusity D_s in the solid phase.

4.4.3 Thermosolutal solidification and dendritic growth in 2D

In this section, the PFM/LBM model is implemented to simulate the 2D dendritic growth of a binary alloy into an undercooled melt with coupled melt flow and thermosolutal convection-diffusion. The diffusion cases at $Le = 1$ and 50 studied in [70] are used for model verification; and we also report our simulation results under convection at $Le = 50$.

First, for the diffusion case with $Le = 1$, the same parameters as in [70] are used including $\lambda = 3.1913$, $Mc_\infty = 0.5325$, $U_0 = 0$, $\theta_0 = -0.55$, $k = 0.15$, $\varepsilon_s = 0.02$, and $\tilde{D}_l = D_l\tau_0 / W_0^2 = 2$;

addtionally, we choose the reference length and time scales $W_0 = 2.5\delta x$ and $\tau_0 = 55\delta t$, respectively, which yield a domain size of $2395\delta x \times 2395\delta x$ to maintain the same resolution as in [70]. And the same initial seed radius is also used ($R_s = 65d_0 = 45\delta x$). The evolution of the tip velocity and radius (results are symmetric for the four tips) is presented in Figure 4.14, where it is clear that the tip velocity matches extremely well with the reference data, and although persistent discrepancy in the tip radius results is noticed at small times, they both converge to close steady results. It is speculated that the initial phase field, $\phi(\mathbf{x},0) = \tanh\left[\left(R_s - d_s\right)/\sqrt{2W_o}\right]$ with d_s the distance to the seed center used in the present simulation following [134] could be responsible for the early deviation in Figure 4.14b. To further verify the accuracy of the present model, Figure 4.15 shows the comparison of the profiles of ϕ, U, and θ along the central dendrite axis with those in [70] at $tD_l/d_0^2 = 470{,}000$. The present results match very well with the published data in general, and the discrepancy in the U profiles near the dendrite center is due to the non-zero solid solute diffusivity ($D_s/D_l = 10^{-4}$) used, as a similar behavior is also noted in Figure 4.13b.

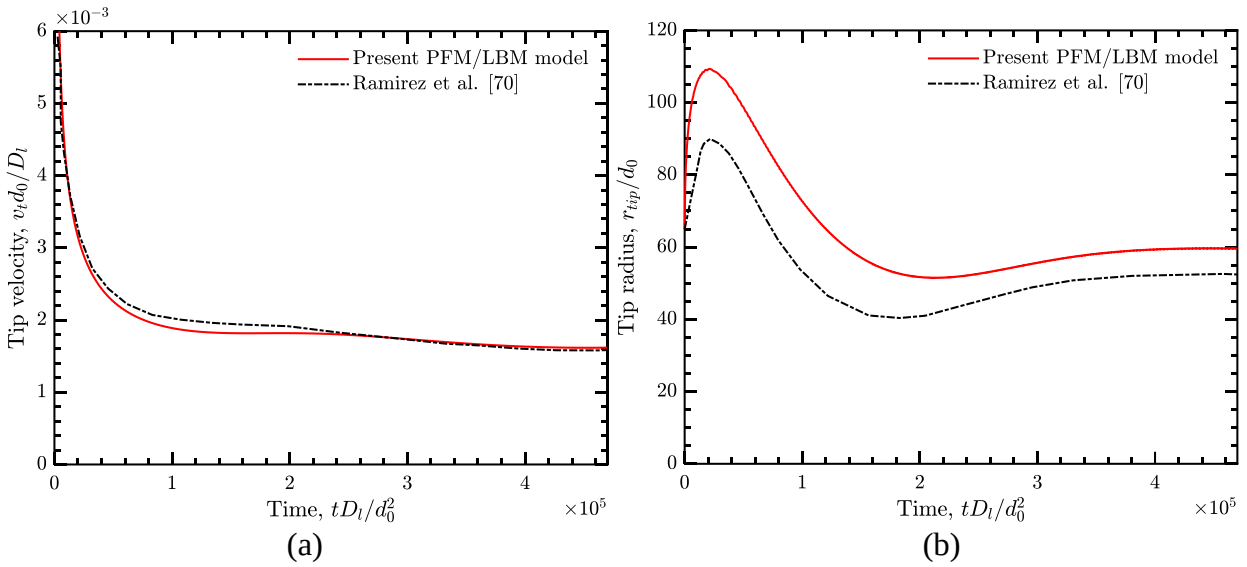

Figure 4.14 Evolution of (a) tip velocity and (b) tip radius for the 2D thermosolutal dendritic growth with pure-diffusion at Le = 1.

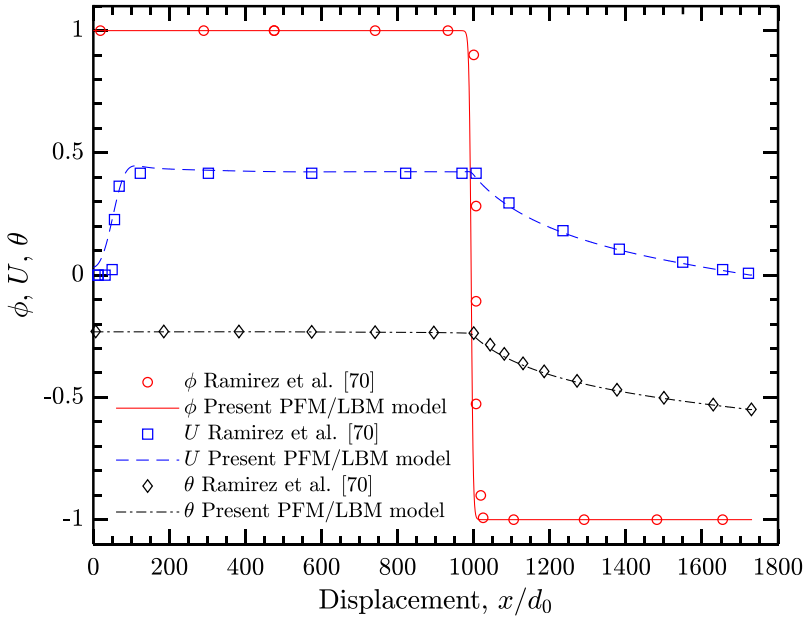

Figure 4.15 Simulated ϕ, U, and θ profiles along the central dendrite axis at tD_l / d_0^2 = 470,000.

Next, thermosolutal dendritic growth at higher Lewis numbers is simulated. As emphasized in Chapter 4.2.1, the present PFM/LBM model is particularly stable in simulating high *Le* cases. For illustration purposes, Figure 4.16 a-f presents the phase field, concentration, and temperature fields at tD_l/d_0^2= 3500 for both the diffusion-only and convection-diffusion cases. The simulation parameters include *Le* = 50, λ = 1.5957, $\tilde{D}_l$ = 1, Mc_∞ = 0.1, k = 0.15, ε_s = 0.02, $W_0 = 2\delta x$, and $\tau_0 = 1000\delta t$; initial distributions $\phi_0 = \tanh\left[\left(R_s - d_s\right)/\sqrt{2W_o}\right]$, U_0 = 0, and θ_0 = -0.55 and far-field Dirichlet boundary conditions ϕ = -1, U = 0, and θ = -0.55 are employed; and the computational domian size is $1751\delta x \times 1751\delta x$ with two initial seed radii $R_s = 20\delta x$ and $R_s = 44\delta x$ tested. Similar to the convection test in Section 4.3.1, constant inlet flow condition ($u_{in} = W_0/\tau_0$) and the converged flow field over the circular seed as initial condition are implemented for the convection-diffusion case with $Pe_\alpha = \frac{W_0^2}{\alpha\tau_0} = \frac{1}{\tilde{D}_l Le} = 0.02$ and Pr = 23.1. The distributions in Figure 4.16 are very similar to those reported in [70] for pure diffusion and [88] for convection-diffusion dendritic growth. In particular, the complex microsegregation pattern in the solid is fully captured; the thermal boundary layer thickness is much larger than that of the solutal boundary layer due to the high *Le* simulated; the concentration variations are mainly confined within the solid phase with more complex contours obtained compared to those in [70] as a non-zero solid solutal diffusivity is used in the present model; noticeable temperature variations in a much larger domain are observed including those in the solid; and the effects of the melt flow and convection on the field distributions are also clearly seen in Figure 4.16 b, d, f with the upstream primary and secondary tips growing much faster and with significantly higher tip temperature compared to the pure diffusion case in Figure 4.16 a, c, e.

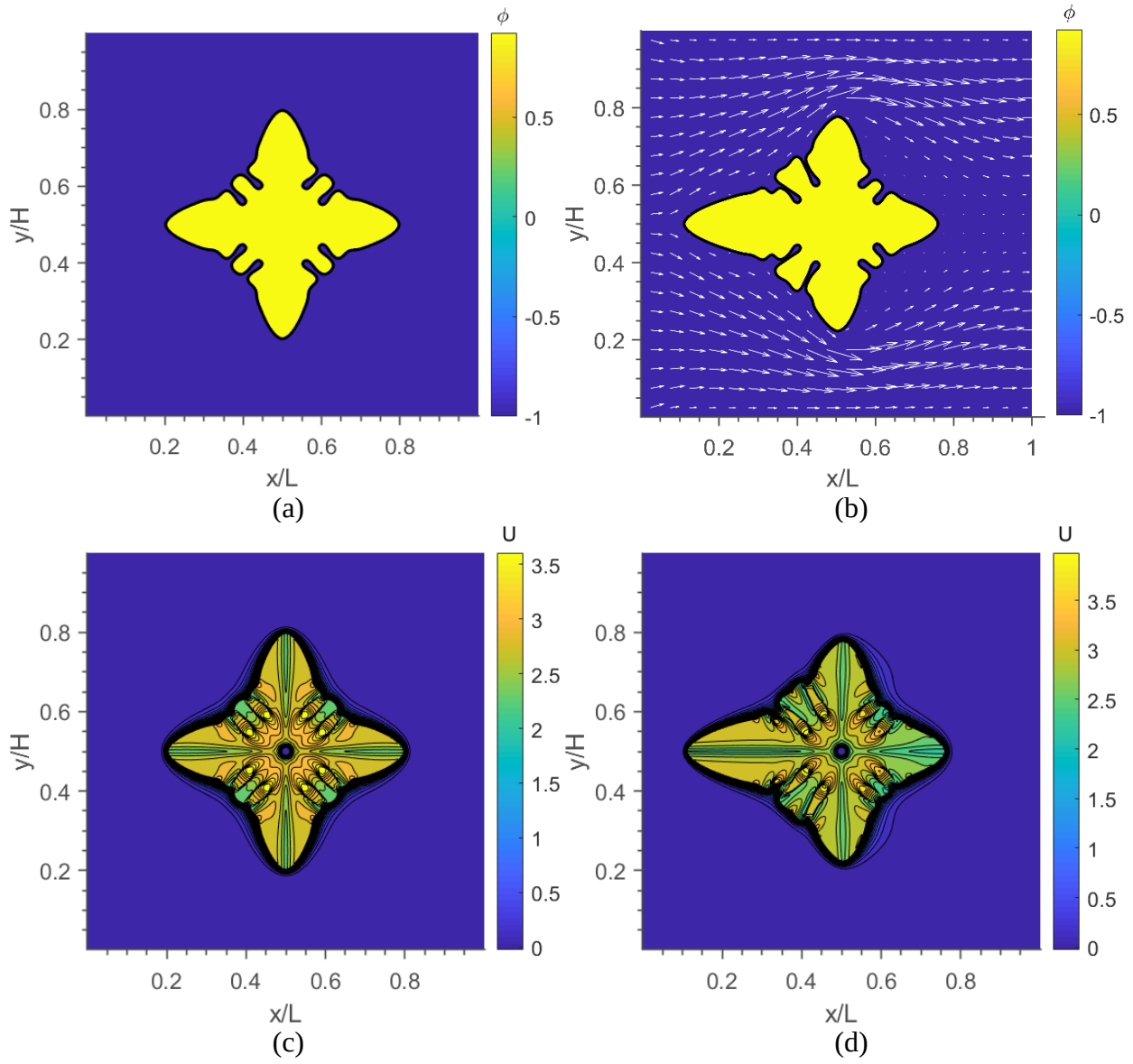

Figure 4.16 Distributions of (a, b) the phase fields, (c, d) concentration fields, and (e, f) temperature fields at tD_l / d_0^2 = 3500 for the 2D fully coupled thermosolutal dendritic growth. (a, c, e) are simulations for the pure diffusion case and (b, d, f) for the convection-diffusion case both at Le = 50.

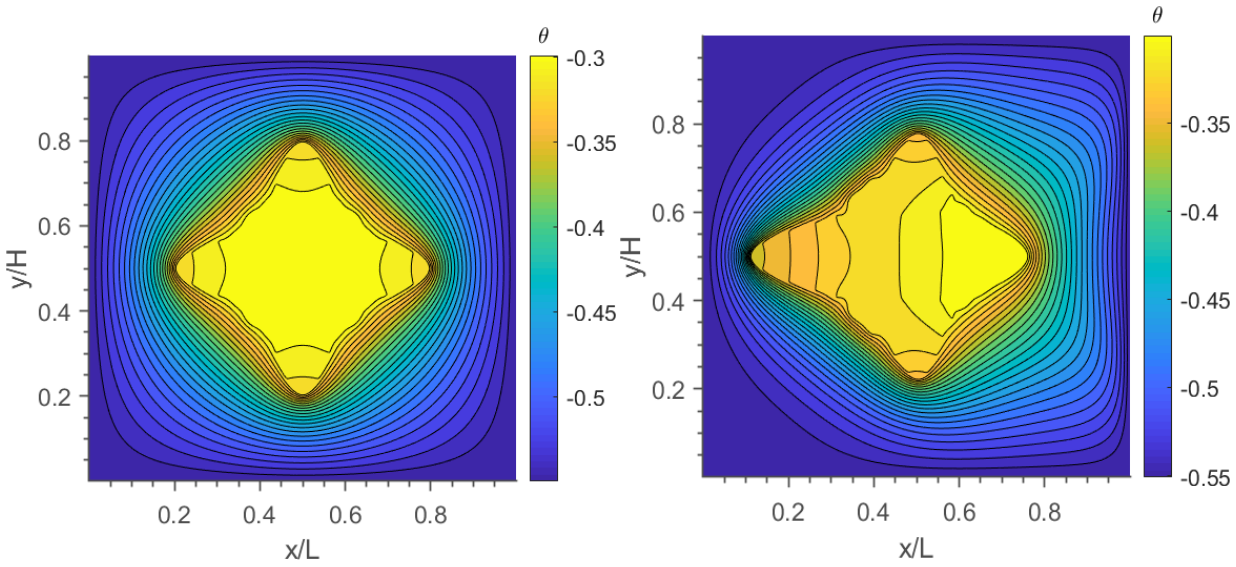

(e) (f)

Figure 4.16 (continued)

To further verify the temporal accuracy of the present model, Figures 4.17 and 4.18 show the evolution of the primary tip velocity and tip radius results for the respective diffusion and convection-diffusion cases at Le = 50 and with the same parameters described above. The results from [70] are also included in Figure 4.17 as references. First, the overall agreement in Figure 4.17 is encouraging, especially for the excellent agreement of tip velocity at small times and the close steady tip radius results. It should be noted that the present work represents the first quantitative comparison with the published data in [70] for the dendritic growth with coupled thermosolutal transport. Second, the present simulation results with two different R_s values confirm the sensitivity of the tip evolution with the initial seed size, which was also examined in detail in [140] in terms of interface morphology. Moreover, the results in Figure 4.17 demonstrate that even though obvious discrepancies are noticed with different initial seed sizes, their steady-state (when domain size is large enough) results are almost identical for both tip velocity and radius. Compared to the large fluctuations in the data from [70] in Figure 4.17 a, b,

it is believed that the present simulation results are more reliable. Lastly, the effect of the melt flow and convection on the evolution of the four primary tips is clearly seen in Figure 4.18 a, b. In summary, the present results in Figures 4.17 and 4.18 can serve as benchmark data for verification of phase-field models for dendritic growth with fully coupled thermosolutal transport.

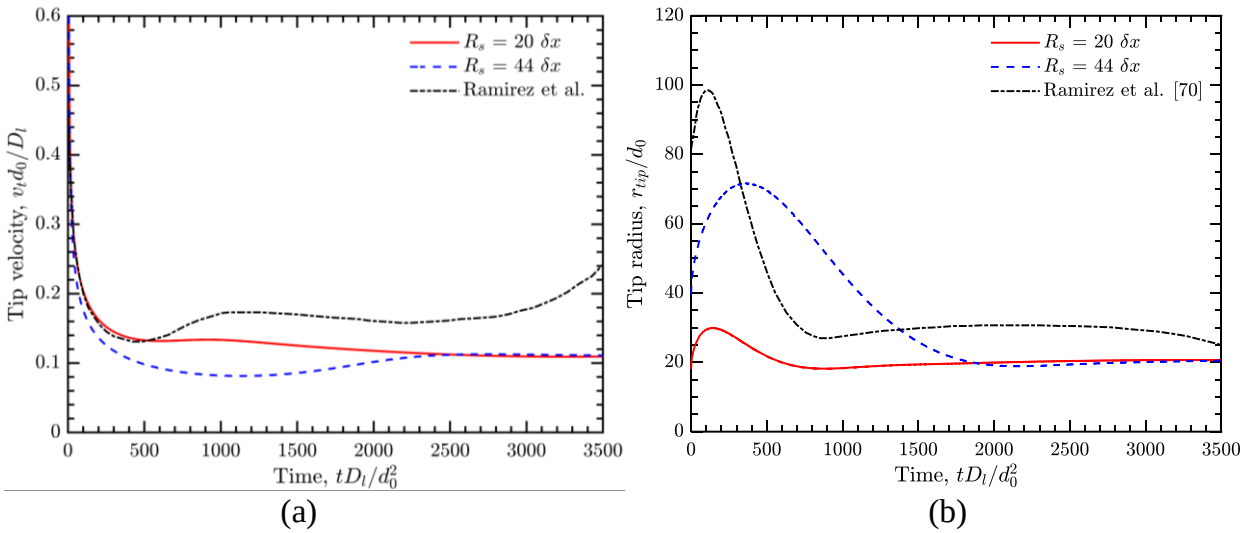

Figure 4.17 Evolution of (a) the primary tip velocities and (b) tip radii for 2D dendritic growth with thermosolutal diffusion at Le = 50.

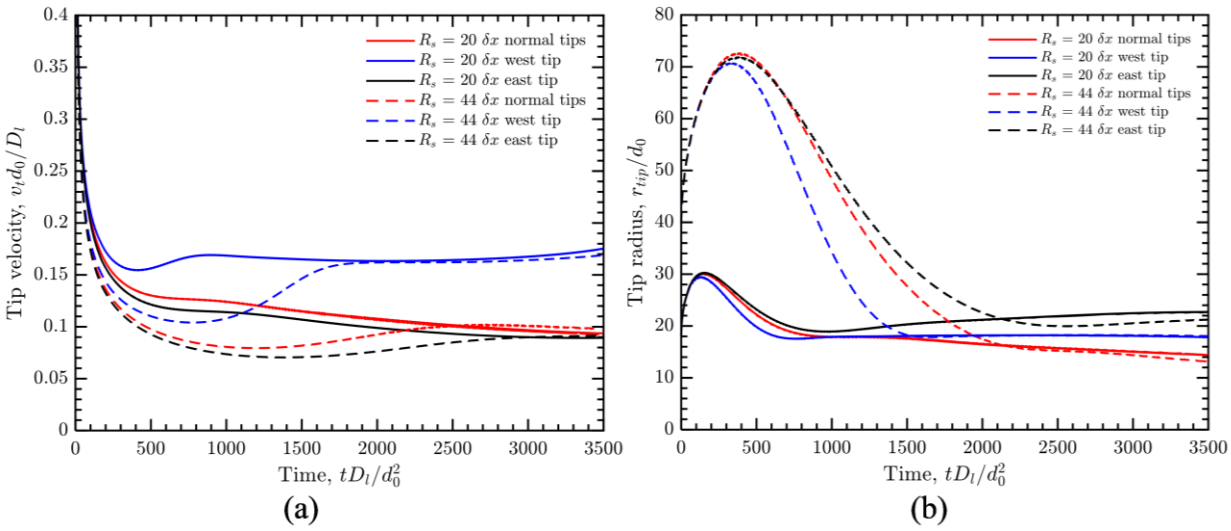

Figure 4.18 Evolution of (a) the primary tip velocities and (b) tip radii for the 2D dendritic growth with thermosolutal convection-diffusion at Le = 50.

4.4.4 Thermal/iso-solutal dendritic solidification in 3D

In this section, dendritic growth in 3D with pure diffusion is simulated to verify the present PFM/LBM model when extended to 3D. The thermal/iso-sloutal diffusion problem in Chapter 4.3.1 is directly extended to 3D with the same characteristic parameters Le = 1, Mc_∞ = 0, ε_s = 0.05 and λ = 6.3826. A computational domain with $385\delta x \times 385\delta x \times 385\delta x$ grid sizes and a spherical seed of initial radius $R_s = 10\delta x$ are used, and the interface thickness and reference time are selected as $W_0 = 2.5\delta x$ and $\tau_0 = 125\delta t$. Figure 4.19 shows the representative phase-field and temperature distributions at t/τ_0 = 60. The 3D contours in Figure 4.19 a, b can be observed to be symmetric across the three central coordinate planes; and the 2D phase-field contours in Figure 4.19c are similar to those presented in Section 4.3.1. Furthermore, Figure 4.20 compares the computed tip growth velocity and radius results with those reported by Jeong et al [144], where excellent agreement for the tip velocities are observed in Fig. 4.20a, and similar trends in tip radii are shown in Figure 4.20b with slight discrepancies in magnitude. It should be noted that

similar phenomena are observed and discussed in Chapter 4.3.3, the tip radius results are very sensitive to the initial seed size, the initial phase-field distribution and the evaluation schemes used.

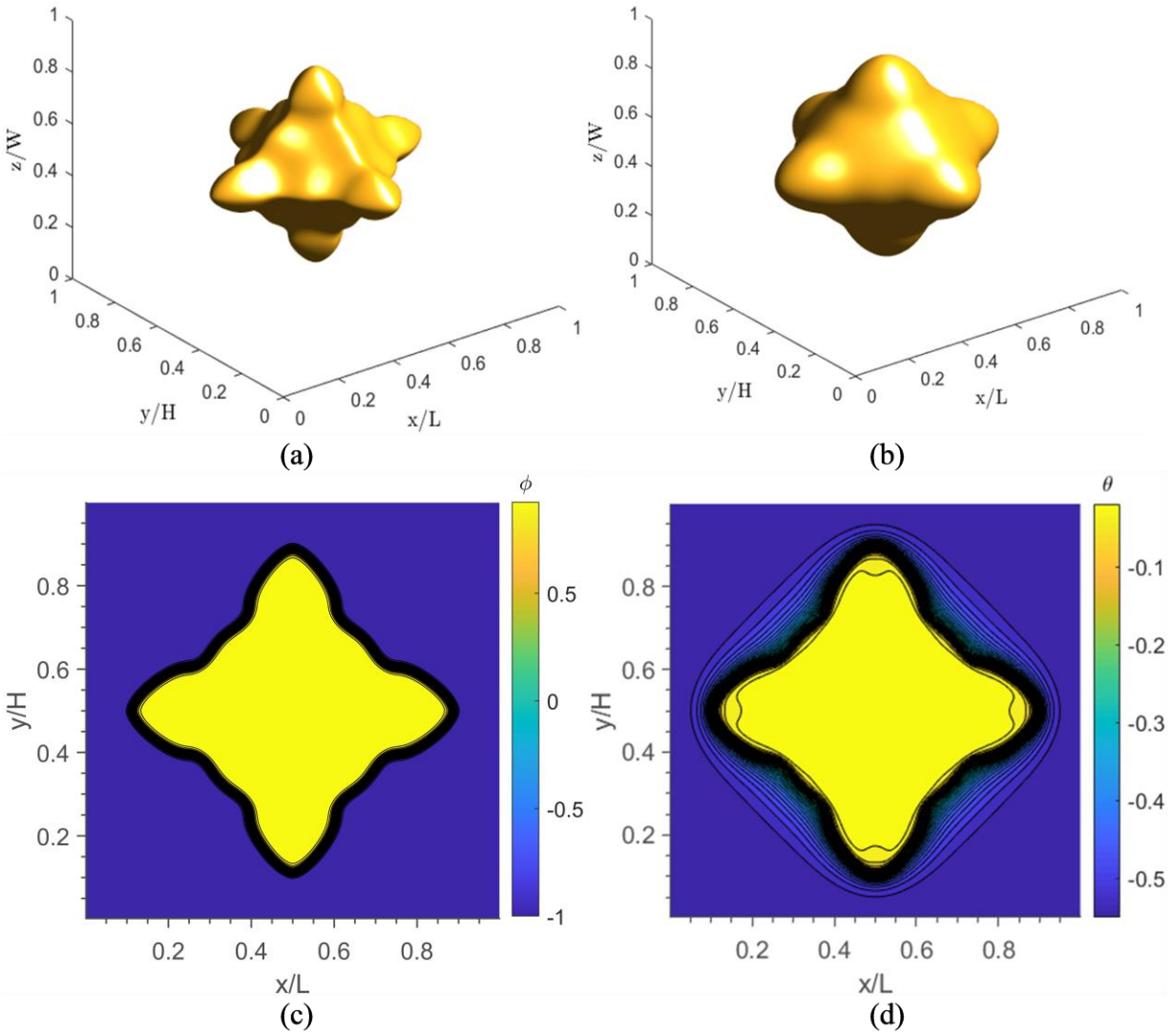

Figure 4.19 (a) Dendritic shape at ϕ = 0 and (b) isothermal shape at θ = -0.25 in 3D, and (c) phase-field and (d) temperature contours in 2D on the central *x*-*y* plane for the 3D thermal/iso-solutal dendritic growth problem with pure diffusion. All results are at t/τ_0 = 60.

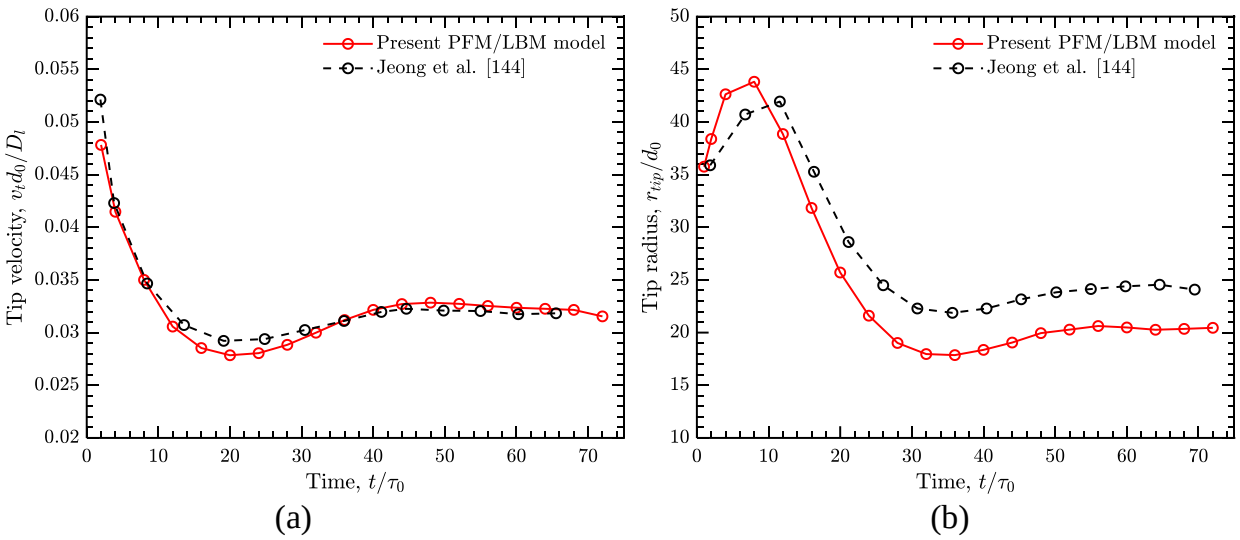

Figure 4.20 Evolution of (a) tip velocities and (b) tip radii on the central *x*-*y* plane for 3D dendritic growth with pure diffusion.

4.4.5 Effect of natural convection on multiple crystals growth

The effect of buoyancy force caused by solute concentration and temperature gradient on multiple dendritic growth is studied in this Section. According to the Boussinesq approximation [31,154], the total buoyance force can be expressed by $\mathbf{F} = -\mathbf{g}\rho_0[\beta_C(C - C_0) + \beta_T(T - T_0)]$. Here, **g** is the gravitational accerlation, ρ_0 the reference density at the reference concentration C_0 and reference temperature T_0, β_C the solutal expansion coefficient, and β_T the thermal expansion coefficient. In order to simplify model, β_T is set as 0 for all test cases. In this study, Al-3wt%Cu binary alloy was selected as the test material. The 2D computational domian is set as a rectangle with 1024 × 2048 grid points, ten seeds with $R_s = 10\delta x$ are placed on the bottom. The initial supersaturation is set to be θ_0 = -0.7. The material and simulation parameters are summarized in Table 4.1.

Table 4.1 Material and simulation parameters for simulation dendritic growth of Al-3wt%Cu binary alloy.

Parameters	Symbol	Value	Unit
Thermal diffusivity	α	0.013	m^2/s
Fluid kinematic viscosity	v	1×10^{-8}	m^2/s
Partition coefficient	k	0.15	-
Anisotropic strength	ε_s	0.01	-
Gravitational acceleration	g_0	9.80665	m/s^2
Interface thickness	W_0	0.9375	μm
Lattice size	δx	0.75	μm
Time increment	δt	9.375	μs

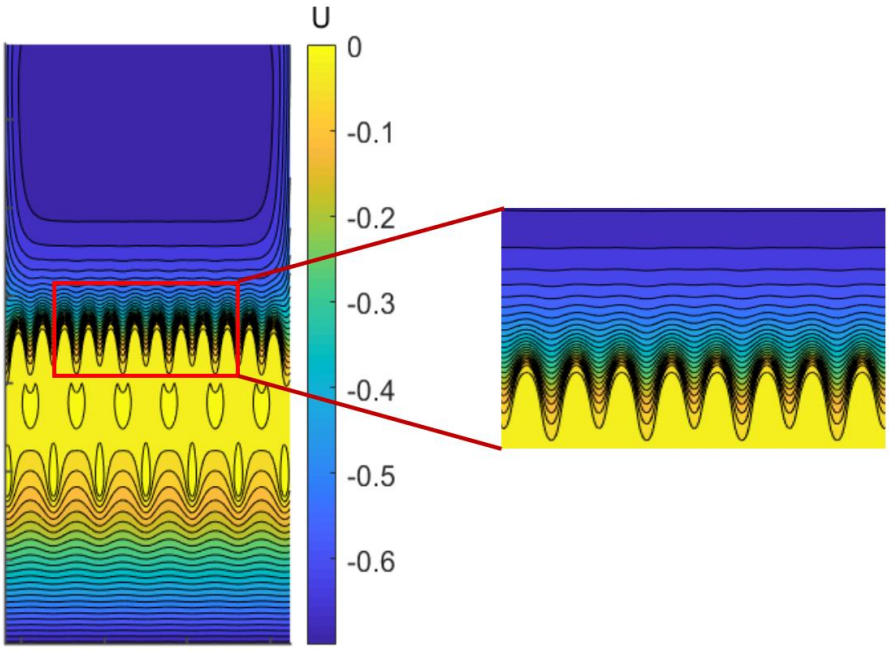

Figure 4.21 Dendrite morphology and temperature field at 1.5×10^6 time step with g = g_0/50.

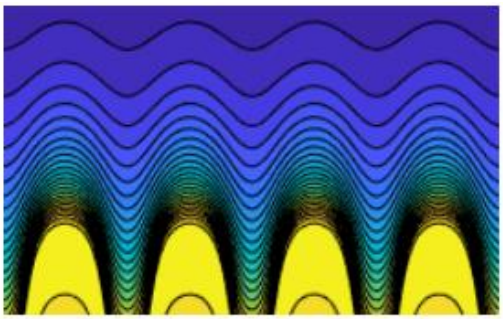

(a)

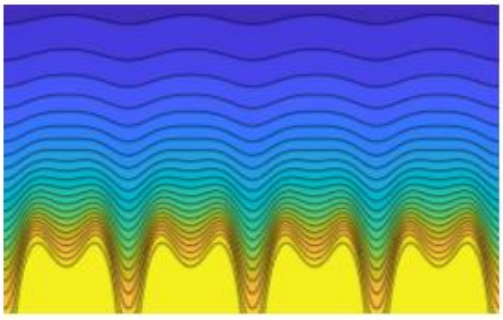

(b)

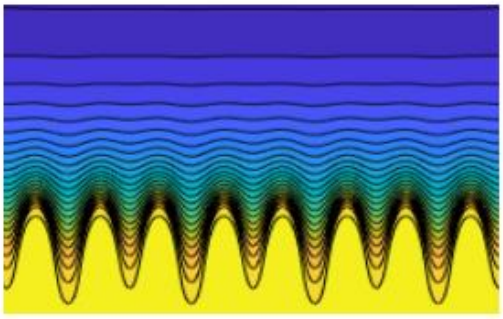

(c)

Figure 4.22 Enlarged views around dendrite tips for g = (a) $-g_0/50$, (b) 0, and (c) $g_0/50$, are shown in Fig. 4.22.

Figure 4.21 shows the dendrite morphology and temperature field at 1.5×10^6 time step for the 2D simulations, where the gravitational acceleration g was changed as g = $g_0/50$. The enlarged views around dendrite tips for g = (a) $-g_0/50$, (b) 0, and (c) $g_0/50$, are shown in Fig.

4.22. It can be observed that the number of primary tips of three test cases with different gravity acceleration values are (a) 4, (b) 6, (c) 8, respectively. The number of primary dendrite branches increases with the increase of gravitational acceleration value (from negative to positive), meanwhile, the primary dendrite spacing is decreasing. This observation is consistent with the results pointed out in the published study [31].

4.5 Conclusions

A new PFM/LBM model for solidification and dendritic growth simulation with fully coupled melt flow and thermosolutal convection-diffusion was developed in this chapter based on a synergy of the phase-field method (PFM) and the lattice Boltzmann method (LBM). The attractive feature of the diffuse interface in the PFM was maintained to effectively simulate the complex dendritic morphology evolution; and different from previous *hybrid* PFM-LBM models where the LBM was mainly applied to simulate the flow field, the present *coupled* PFM/LBM model inherits the intrinsic benefits of the LBM (e.g., simple and explicit algorithms, convenient boundary/interface treatment, and compatibility with parallelization), and all the evolution of the phase field, flow field, solute and thermal fields is simulated in the LB framework with a single Cartesian grid system. In addition, effective diffuse interface treatments are proposed in the LB schemes, which are directly implemented to the entire computational domain. Moreover, to improve the model stability and accuracy, multiple-relaxation-time (MRT) LB schemes are applied for all. Furthermore, in order to simulate various dendritic growth problems with wide ranges of characteristic parameters, a multiple-time-scaling strategy is employed in the LB framework that effectively decouples the times steps in the four LB schemes.

The efficacy of each of those unique features and the overall accuracy of the coupled PFM/LBM model were verified with representative numerical tests involving melt flow and

thermosolutal convection-diffusion in 2D and pure diffusion in 3D. It was demonstrated that with comparable spatial and temporal resolution, the present model showed more robust and consistent results than those in the literature in terms of the dendrite tip growth velocity and radius. The reported simulation results for thermosolutal dendritic solidification with and without convection can serve as reliable benchmark data. The coupled PFM/LBM model are capable of simulating large-scale dendritic growth with natural convection effects.

CHAPTER V

SUMMARY AND FUTURE WORK

5.1 Summary

In this dissertation, the heat and mass transfer between different materials and phases with different interface schemes were computationally studied in the following aspects: conjugate heat and mass transfer modeling with the LBM, novel interface scheme in the LBM for conjugate heat and mass transfer between materials/phases with very high transport property ratios, and PFM/LBM for dendritic growth and solidification modeling.

CHAPTER I showed the background of conjugate heat and mass transfer at sharp interfaces and diffuse interface schemes for dendritic growth in the solidification of pure materials and alloys.

CHAPTER II compared the accuracy and convergence order of various sharp interface schemes for conjugate heat and mass transfer modeling using lattice Boltzmann method (LBM). The interface schemes studied were divided into three groups, and numerical experiments were carried out through both straight interface and curved interface. For general cases, the accuracy of LB results was up to the first order with the schemes by adding source terms (Group 1), reformulating the transport problem with an alternative governing equation for an enthalpy-like quantity (Group 2), and using modified equilibrium distribution functions in the LB model (Group 3). Groups 1 and 2 always yielded zeroth-order accuracy at moderate to high resolution due to the discontinuity effect in the heat capacitance gradient approximation, while the Group 3

scheme can be improved to preserve second-order accuracy by also including the interpolation-based interface scheme. The influence of curved interface geometry on the accuracy of LB results became more obvious. In particular, the interpolation-based interface schemes, including that proposed in [14] and the improved Group 3, were capable of retaining first-order accuracy; and their error magnitude was also much smaller than that obtained from using the basic Group 3 scheme; however, the schemes in Groups 1 and 2 always yielded zeroth-order accurate results with large error magnitude.

CHAPTER III investigated the effective thermal conductivity of porous lattice structures. A computational model based on lattice Boltzmann method (LBM) was proposed to predict the effective thermal conductivity (ETC) of lattice structures based on different topologies. The applicability and accuracy of the LBM model and the interface scheme in ETC prediction was verified by numerical tests and validated with in-house measurements of the additively manufactured (AM) metal foam samples with these topologies as well as previously published results. Systematic simulations was performed for all four structures and different solid-liquid material pairs, and analytical correlations was developed as second-order polynomials of porosity over the entire range of $0 \leqslant \varepsilon \leqslant 1$. The correlations for the ETC normalized by the solid thermal conductivity k_{eff}/k_s are applicable to various material pairs. The modified correlation based on the high porosity range and the two metal pairs can improve the accuracy of ETC prediction for specific application. They can serve as valuable evaluation and prediction tools for future design and innovation in AM structures as lightweight and compact heat sinks/exchangers.

CHAPTER IV developed a phase-field model (PFM) formulated within the system of lattice Boltzmann (LB) equation for simulating solidification and dendritic growth with fully

coupled melt flow and thermosolutal convection–diffusion. The efficacy of those unique features and the overall accuracy of the coupled PFM/LBM model were verified with representative numerical tests involving melt flow and thermosolutal convection–diffusion in 2D and pure diffusion in 3D. The results showed that, with comparable spatial and temporal resolution, the present model showed more robust and consistent results than in the literature in terms of dendrite tip growth velocity and radius. The reported simulation results of thermal dendritic solidification with and without convection can serve as reliable benchmark data.

5.2 Future work

Future studies will focus on applications of the verified PFM/LBM model to simulate large-scale dendritic growth such as those with natural and forced convection effects and involving dendrite motion driven by melt flow, and model validation with experimental measurements available in the literature. The research on the flow and thermal transport characteristics of high-porosity metal foams, such as permeability (K), inertial coefficient (c_f), interstitial heat transfer coefficient (h_{sf}), will be completed in the future work. The interstitial heat transfer coefficient in porous structures will be predicted by an effective numerical model based on the lattice Boltzmann method. The conjugate heat and mass transfer computational study will be carried out in the control volume. A constant temperature and heat flux will be applied on the fiber interface to determine the h_{sf} around the fibers. The accuracy of the numerical model will be verified by comparing with the experimental data.

REFERENCES

[1] B. Roe, R. Jaiman, A. Haselbacher, P.H. Geubelle, Combined interface boundary condition method for coupled thermal simulations, Int. J. Numer. Methods Fluids. 57 (2008) 329–354. https://doi.org/10.1002/fld.1637.

[2] A. Dorfman, Z. Renner, Conjugate Problems in Convective Heat Transfer: Review, Math. Probl. Eng. (2009) 27. https://doi.org/10.1155/2009/927350.

[3] F. Favre, O. Antepara, C. Oliet, O. Lehmkuhl, C.D. Perez-Segarra, An immersed boundary method to conjugate heat transfer problems in complex geometries. Application to an automotive antenna, Appl. Therm. Eng. 148 (2019) 907–928. https://doi.org/10.1016/J.APPLTHERMALENG.2018.11.099.

[4] L. Li, R. Mei, J.F. Klausner, D.W. Hahn, Heat Transfer Between Colliding Surfaces and Particles, J. Heat Transfer. 134 (2011) 011301. https://doi.org/10.1115/1.4004874.

[5] J. Zhang, C. Yang, Z.-S. Mao, Unsteady conjugate mass transfer from a spherical drop in simple extensional creeping flow, Chem. Eng. Sci. 79 (2012) 29–40. https://doi.org/10.1016/J.CES.2012.05.038.

[6] M.-P. Errera, S. Chemin, Optimal solutions of numerical interface conditions in fluid–structure thermal analysis, J. Comput. Phys. 245 (2013) 431–455. https://doi.org/10.1016/J.JCP.2013.03.004.

[7] A.J. Chamkha, M.A. Ismael, Conjugate heat transfer in a porous cavity filled with nanofluids and heated by a triangular thick wall, Int. J. Therm. Sci. 67 (2013) 135–151. https://doi.org/10.1016/J.IJTHERMALSCI.2012.12.002.

[8] A. Mensch, K.A. Thole, Conjugate heat transfer analysis of the effects of impingement channel height for a turbine blade endwall, Int. J. Heat Mass Transf. 82 (2015) 66–77. https://doi.org/10.1016/J.IJHEATMASSTRANSFER.2014.10.076.

[9] P. Caccavale, M.V. De Bonis, G. Ruocco, Conjugate heat and mass transfer in drying: A modeling review, J. Food Eng. 176 (2016) 28–35. https://doi.org/10.1016/J.JFOODENG.2015.08.031.

[10] R. Qi, D. Li, H. Li, H. Wang, L.-Z. Zhang, Heat and mass transfer in a polymeric electrolyte membrane-based electrochemical air dehumidification system: Model development and performance analysis, Int. J. Heat Mass Transf. 126 (2018) 888–898. https://doi.org/10.1016/J.IJHEATMASSTRANSFER.2018.06.010.

[11] L. Chai, L. Wang, X. Bai, Thermohydraulic performance of microchannel heat sinks with triangular ribs on sidewalls – Part 2: Average fluid flow and heat transfer characteristics, Int. J. Heat Mass Transf. (2019). https://doi.org/10.1016/j.ijheatmasstransfer.2018.09.027.

[12] D. Chiappini, M. Sbragaglia, X. Xue, G. Falcucci, Hydrodynamic behavior of the pseudopotential lattice Boltzmann method for interfacial flows, Phys. Rev. E. (2019). https://doi.org/10.1103/PhysRevE.99.053305.

[13] J. Wang, M. Wang, Z. Li, A lattice Boltzmann algorithm for fluid-solid conjugate heat transfer{star, open}{star, open}The present work was supported by the National Natural Science Foundation of China (Grant No. 59995550-2)., Int. J. Therm. Sci. 46 (2007) 228–234. https://doi.org/10.1016/j.ijthermalsci.2006.04.012.

[14] L. Li, C. Chen, R. Mei, J.F. Klausner, Conjugate heat and mass transfer in the lattice Boltzmann equation method, Phys. Rev. E - Stat. Nonlinear, Soft Matter Phys. (2014). https://doi.org/10.1103/PhysRevE.89.043308.

[15] M. Wang, J. Wang, N. Pan, S. Chen, Mesoscopic predictions of the effective thermal conductivity for microscale random porous media, Phys. Rev. E - Stat. Nonlinear, Soft Matter Phys. (2007). https://doi.org/10.1103/PhysRevE.75.036702.

[16] H. Yoshida, T. Kobayashi, H. Hayashi, T. Kinjo, H. Washizu, K. Fukuzawa, Boundary condition at a two-phase interface in the lattice Boltzmann method for the convection-diffusion equation, Phys. Rev. E - Stat. Nonlinear, Soft Matter Phys. 90 (2014). https://doi.org/10.1103/PhysRevE.90.013303.

[17] J.A. Sethian, J. Straint, Crystal growth and dendritic solidification, J. Comput. Phys. (1992). https://doi.org/10.1016/0021-9991(92)90140-T.

[18] T. Ihle, H. Müller-Krumbhaar, Fractal and compact growth morphologies in phase transitions with diffusion transport, Phys. Rev. E. (1994). https://doi.org/10.1103/PhysRevE.49.2972.

[19] R. Almgren, Variational algorithms and pattern formation in dendritic solidification, J. Comput. Phys. (1993). https://doi.org/10.1016/S0021-9991(83)71112-5.

[20] J.E. Taylor, Modeling crystal growth in a diffusion field using fully faceted interfaces, J. Comput. Phys. (1994). https://doi.org/10.1006/jcph.1994.1153.

[21] A. Karma, W.J. Rappel, Phase-field method for computationally efficient modeling of solidification with arbitrary interface kinetics, Phys. Rev. E - Stat. Physics, Plasmas, Fluids, Relat. Interdiscip. Top. (1996). https://doi.org/10.1103/PhysRevE.53.R3017.

[22] Y. Sun, C. Beckermann, Sharp interface tracking using the phase-field equation, J. Comput. Phys. (2007). https://doi.org/10.1016/j.jcp.2006.05.025.

[23] S. Chen, G.D. Doolen, Lattice boltzmann method for fluid flows, Annu. Rev. Fluid Mech. (1998). https://doi.org/10.1146/annurev.fluid.30.1.329.

[24] S. Succi, The Lattice Boltzmann Equation for Fluid Dynamics and Beyond, Oxford Univ. Press. New York. (2001). https://doi.org/10.1016/s0997-7546(02)00005-5.

[25] D. Yu, R. Mei, L.S. Luo, W. Shyy, Viscous flow computations with the method of lattice Boltzmann equation, Prog. Aerosp. Sci. (2003). https://doi.org/10.1016/S0376-0421(03)00003-4.

[26] C.K. Aidun, J.R. Clausen, Lattice-boltzmann method for complex flows, Annu. Rev. Fluid Mech. (2010). https://doi.org/10.1146/annurev-fluid-121108-145519.

[27] W.J. Boettinger, J.A. Warren, C. Beckermann, A. Karma, PHASE-FIELD SIMULATION OF SOLIDIFICATION 1, Annu. Rev. Mater. Res. 32 (2002) 163–94. https://doi.org/10.1146/annurev.matsci.32.101901.155803.

[28] M. Asta, C. Beckermann, A. Karma, W. Kurz, R. Napolitano, M. Plapp, G. Purdy, M. Rappaz, R. Trivedi, Solidification microstructures and solid-state parallels: Recent developments, future directions, Acta Mater. (2009). https://doi.org/10.1016/j.actamat.2008.10.020.

[29] I. Steinbach, Why solidification? Why phase-field?, JOM. (2013). https://doi.org/10.1007/s11837-013-0681-5.

[30] T. Takaki, R. Rojas, S. Sakane, M. Ohno, Y. Shibuta, T. Shimokawabe, T. Aoki, Phase-field-lattice Boltzmann studies for dendritic growth with natural convection, J. Cryst. Growth. (2017). https://doi.org/10.1016/j.jcrysgro.2016.11.099.

[31] T. Takaki, S. Sakane, M. Ohno, Y. Shibuta, T. Aoki, Large–scale phase–field lattice Boltzmann study on the effects of natural convection on dendrite morphology formed during directional solidification of a binary alloy, Comput. Mater. Sci. (2020). https://doi.org/10.1016/j.commatsci.2019.109209.

[32] D. Medvedev, K. Kassner, Lattice Boltzmann scheme for crystal growth in external flows, Phys. Rev. E - Stat. Nonlinear, Soft Matter Phys. (2005). https://doi.org/10.1103/PhysRevE.72.056703.

[33] R. Rojas, T. Takaki, M. Ohno, A phase-field-lattice Boltzmann method for modeling motion and growth of a dendrite for binary alloy solidification in the presence of melt convection, J. Comput. Phys. (2015). https://doi.org/10.1016/j.jcp.2015.05.045.

[34] K. Guo, L. Li, G. Xiao, N. Auyeung, R. Mei, Lattice Boltzmann method for conjugate heat and mass transfer with interfacial jump conditions, Int. J. Heat Mass Transf. 88 (2015) 306–322. https://doi.org/10.1016/j.ijheatmasstransfer.2015.04.064.

[35] Z. Hu, J. Huang, W.A. Yong, Lattice Boltzmann method for convection-diffusion equations with general interfacial conditions, Phys. Rev. E. 93 (2016) 1–16. https://doi.org/10.1103/PhysRevE.93.043320.

[36] Y.-T. Mu, Z.-L. Gu, P. He, W.-Q. Tao, Lattice Boltzmann method for conjugated heat and mass transfer with general interfacial conditions, Phys. Rev. E. 98 (2018) 43309. https://doi.org/10.1103/PhysRevE.98.043309.

[37] J.H. Lu, H.Y. Lei, C.S. Dai, Analysis of Henry's law and a unified lattice Boltzmann equation for conjugate mass transfer problem, Chem. Eng. Sci. 199 (2019) 319–331. https://doi.org/10.1016/J.CES.2019.01.021.

[38] K. Han, Y.T. Feng, D.R.J. Owen, Modelling of thermal contact resistance within the framework of the thermal lattice Boltzmann method, Int. J. Therm. Sci. 47 (2008) 1276–1283. https://doi.org/10.1016/J.IJTHERMALSCI.2007.11.007.

[39] R.P. Fedkiw, T. Aslam, B. Merriman, S. Osher, A Non-oscillatory Eulerian Approach to Interfaces in Multimaterial Flows (the Ghost Fluid Method), J. Comput. Phys. 152 (1999) 457–492. https://doi.org/10.1006/JCPH.1999.6236.

[40] X.-D. Liu, R.P. Fedkiw, M. Kang, A Boundary Condition Capturing Method for Poisson's Equation on Irregular Domains, J. Comput. Phys. 160 (2000) 151–178. https://doi.org/10.1006/JCPH.2000.6444.

[41] H.S. Udaykumar, R. Mittal, P. Rampunggoon, A. Khanna, A Sharp Interface Cartesian Grid Method for Simulating Flows with Complex Moving Boundaries, J. Comput. Phys. 174 (2001) 345–380. https://doi.org/10.1006/JCPH.2001.6916.

[42] S. Marella, S. Krishnan, H. Liu, H.S. Udaykumar, Sharp interface Cartesian grid method I: An easily implemented technique for 3D moving boundary computations, J. Comput. Phys. 210 (2005) 1–31. https://doi.org/10.1016/J.JCP.2005.03.031.

[43] P. Ranut, On the effective thermal conductivity of aluminum metal foams: Review and improvement of the available empirical and analytical models, Appl. Therm. Eng. (2016). https://doi.org/10.1016/j.applthermaleng.2015.09.094.

[44] S. Mahjoob, K. Vafai, A synthesis of fluid and thermal transport models for metal foam heat exchangers, Int. J. Heat Mass Transf. (2008). https://doi.org/10.1016/j.ijheatmasstransfer.2007.12.012.

[45] P. Kumar, F. Topin, State-of-the-Art of Pressure Drop in Open-Cell Porous Foams: Review of Experiments and Correlations, J. Fluids Eng. Trans. ASME. (2017). https://doi.org/10.1115/1.4037034.

[46] G.R. Hadley, Thermal conductivity of packed metal powders, Int. J. Heat Mass Transf. (1986). https://doi.org/10.1016/0017-9310(86)90186-9.

[47] M.N. Miller, Bounds for effective electrical, thermal, and magnetic properties of heterogeneous materials, J. Math. Phys. (1969). https://doi.org/10.1063/1.1664794.

[48] S. Ackermann, J.R. Scheffe, J. Duss, A. Steinfeld, Morphological characterization and effective thermal conductivity of dual-scale reticulated porous structures, Materials (Basel). (2014). https://doi.org/10.3390/ma7117173.

[49] V. V. Calmidi, R.L. Mahajan, The effective thermal conductivity of high porosity fibrous metal foams, J. Heat Transfer. (1999). https://doi.org/10.1115/1.2826001.

[50] R. Singh, H.S. Kasana, Computational aspects of effective thermal conductivity of highly porous metal foams, Appl. Therm. Eng. (2004). https://doi.org/10.1016/j.applthermaleng.2003.12.011.

[51] A. Bhattacharya, V. V. Calmidi, R.L. Mahajan, Thermophysical properties of high porosity metal foams, Int. J. Heat Mass Transf. (2002). https://doi.org/10.1016/S0017-9310(01)00220-4.

[52] J.W. Paek, B.H. Kang, S.Y. Kim, J.M. Hyun, Effective thermal conductivity and permeability of aluminum foam materials, Int. J. Thermophys. (2000). https://doi.org/10.1023/A:1006643815323.

[53] Y. Yao, H. Wu, Z. Liu, A new prediction model for the effective thermal conductivity of high porosity open-cell metal foams, Int. J. Therm. Sci. (2015). https://doi.org/10.1016/j.ijthermalsci.2015.06.008.

[54] X. Xiao, P. Zhang, M. Li, Preparation and thermal characterization of paraffin/metal foam composite phase change material, Appl. Energy. (2013). https://doi.org/10.1016/j.apenergy.2013.04.050.

[55] D. Edouard, The effective thermal conductivity for “slim” and “fat” foams, AIChE J. (2011). https://doi.org/10.1002/aic.12372.

[56] H. Yang, Y. Li, Y. Yang, D. Chen, Y. Zhu, Effective thermal conductivity of high porosity open-cell metal foams, Int. J. Heat Mass Transf. (2020). https://doi.org/10.1016/j.ijheatmasstransfer.2019.118974.

[57] K. Boomsma, D. Poulikakos, On the effective thermal conductivity of a three-dimensionally structured fluid-saturated metal foam, Int. J. Heat Mass Transf. (2001). https://doi.org/10.1016/S0017-9310(00)00123-X.

[58] Z. Dai, K. Nawaz, Y.G. Park, J. Bock, A.M. Jacobi, Correcting and extending the Boomsma-Poulikakos effective thermal conductivity model for three-dimensional, fluid-saturated metal foams, Int. Commun. Heat Mass Transf. (2010). https://doi.org/10.1016/j.icheatmasstransfer.2010.01.015.

[59] X. Fu, R. Viskanta, J.P. Gore, Prediction of effective thermal conductivity of cellular ceramics, Int. Commun. Heat Mass Transf. (1998). https://doi.org/10.1016/S0735-1933(98)00002-5.

[60] S. Krishnan, J.Y. Murthy, S. V. Garimella, Direct simulation of transport in open-cell metal foam, in: J. Heat Transfer, 2006. https://doi.org/10.1115/1.2227038.

[61] K.K. Bodla, J.Y. Murthy, S. V. Garimella, Microtomography-based simulation of transport through open-cell metal foams, Numer. Heat Transf. Part A Appl. (2010). https://doi.org/10.1080/10407782.2010.511987.

[62] M. Zafari, M. Panjepour, M.D. Emami, M. Meratian, Microtomography-based numerical simulation of fluid flow and heat transfer in open cell metal foams, Appl. Therm. Eng. (2015). https://doi.org/10.1016/j.applthermaleng.2015.01.045.

[63] P. Ranut, E. Nobile, L. Mancini, High resolution microtomography-based CFD simulation of flow and heat transfer in aluminum metal foams, Appl. Therm. Eng. (2014). https://doi.org/10.1016/j.applthermaleng.2013.11.056.

[64] Z.G. Qu, T.S. Wang, W.Q. Tao, T.J. Lu, A theoretical octet-truss lattice unit cell model for effective thermal conductivity of consolidated porous materials saturated with fluid, Heat Mass Transf. Und Stoffuebertragung. (2012). https://doi.org/10.1007/s00231-012-0985-y.

[65] P. Ekade, S. Krishnan, Fluid flow and heat transfer characteristics of octet truss lattice geometry, Int. J. Therm. Sci. (2019). https://doi.org/10.1016/j.ijthermalsci.2018.11.031.

[66] A. Chaudhari, P. Ekade, S. Krishnan, Experimental investigation of heat transfer and fluid flow in octet-truss lattice geometry, Int. J. Therm. Sci. (2019). https://doi.org/10.1016/j.ijthermalsci.2019.05.003.

[67] S. Gu, T.J. Lu, A.G. Evans, On the design of two-dimensional cellular metals for combined heat dissipation and structural load capacity, Int. J. Heat Mass Transf. (2001). https://doi.org/10.1016/S0017-9310(00)00234-9.

[68] X. Bai, C. Hasan, M. Mobedi, A. Nakayama, A General Expression for the Stagnant Thermal Conductivity of Stochastic and Periodic Structures, J. Heat Transfer. (2018). https://doi.org/10.1115/1.4038449.

[69] X. Bai, A. Nakayama, Quick estimate of effective thermal conductivity for fluid-saturated metal frame and prismatic cellular structures, Appl. Therm. Eng. (2019). https://doi.org/10.1016/j.applthermaleng.2019.114011.

[70] J.C. Ramirez, C. Beckermann, A. Karma, H.J. Diepers, Phase-field modeling of binary alloy solidification with coupled heat and solute diffusion, Phys. Rev. E - Stat. Physics, Plasmas, Fluids, Relat. Interdiscip. Top. (2004). https://doi.org/10.1103/PhysRevE.69.051607.

[71] L.-Q. Chen, PHASE-FIELD MODELS FOR MICROSTRUCTURE EVOLUTION, Annu. Rev. Mater. Res. 32 (2002) 113–153. https://doi.org/10.1146/annurev.matsci.32.112001.132041.

[72] N. Valizadeh, T. Rabczuk, Isogeometric analysis for phase-field models of geometric PDEs and high-order PDEs on stationary and evolving surfaces, Comput. Methods Appl. Mech. Eng. 351 (2019) 599–642. https://doi.org/10.1016/j.cma.2019.03.043.

[73] D. Medina, N. Valizadeh, E. Samaniego, A.X. Jerves, T. Rabczuk, Isogeometric analysis of insoluble surfactant spreading on a thin film, Comput. Methods Appl. Mech. Eng. 370 (2020) 113272. https://doi.org/10.1016/j.cma.2020.113272.

[74] M. Ashour, N. Valizadeh, T. Rabczuk, Isogeometric analysis for a phase-field constrained optimization problem of morphological evolution of vesicles in electrical fields, Comput. Methods Appl. Mech. Eng. 377 (2021) 113669. https://doi.org/10.1016/j.cma.2021.113669.

[75] S.R. Coriell, W.J. Boettinger, M.R. Cordes, R.F. Sekerka, Effect of gravity on coupled convective and interfacial instabilities during directional solidification, Adv. Sp. Res. (1981). https://doi.org/10.1016/0273-1177(81)90142-3.

[76] S.H. Davis, Hydrodynamic interactions in directional solidification, J. Fluid Mech. (1990). https://doi.org/10.1017/S002211209000194X.

[77] R. Ananth, W.N. Gill, Dendritic growth of an elliptical paraboloid with forced convection in the melt, J. Fluid Mech. (1989). https://doi.org/10.1017/S0022112089002946.

[78] J.J. Xu, Dendritic Growth from a Melt in an External Flow: Uniformly Valid Asymptotic Solution for the Steady State, J. Fluid Mech. (1994). https://doi.org/10.1017/S002211209400409X.

[79] C. Beckermann, H.J. Diepers, I. Steinbach, A. Karma, X. Tong, Modeling Melt Convection in Phase-Field Simulations of Solidification, J. Comput. Phys. (1999). https://doi.org/10.1006/jcph.1999.6323.

[80] L. Yuan, P.D. Lee, Dendritic solidification under natural and forced convection in binary alloys: 2D versus 3D simulation, Model. Simul. Mater. Sci. Eng. (2010). https://doi.org/10.1088/0965-0393/18/5/055008.

[81] T. Takaki, Phase-field modeling and simulations of dendrite growth, in: ISIJ Int., 2014. https://doi.org/10.2355/isijinternational.54.437.

[82] T.Z. Gong, Y. Chen, D.Z. Li, Y.F. Cao, P.X. Fu, Quantitative comparison of dendritic growth under forced flow between 2D and 3D phase-field simulation, Int. J. Heat Mass Transf. (2019). https://doi.org/10.1016/j.ijheatmasstransfer.2019.01.104.

[83] R. Benzi, S. Succi, M. Vergassola, The lattice Boltzmann equation: theory and applications, Phys. Rep. (1992). https://doi.org/10.1016/0370-1573(92)90090-M.

[84] X. He, L.S. Luo, Lattice Boltzmann model for the incompressible Navier-Stokes equation, J. Stat. Phys. (1997). https://doi.org/10.1023/b:joss.0000015179.12689.e4.

[85] H. Yoshida, M. Nagaoka, Multiple-relaxation-time lattice Boltzmann model for the convection and anisotropic diffusion equation, J. Comput. Phys. (2010). https://doi.org/10.1016/j.jcp.2010.06.037.

[86] L. Li, R. Mei, J.F. Klausner, Boundary conditions for thermal lattice Boltzmann equation method, J. Comput. Phys. (2013). https://doi.org/10.1016/j.jcp.2012.11.027.

[87] L. Li, R. Mei, J.F. Klausner, Lattice Boltzmann models for the convection-diffusion equation: D2Q5 vs D2Q9, Int. J. Heat Mass Transf. 108 (2017) 41–62. https://doi.org/10.1016/j.ijheatmasstransfer.2016.11.092.

[88] Z. Guo, J. Mi, S. Xiong, P.S. Grant, Phase field study of the tip operating state of a freely growing dendrite against convection using a novel parallel multigrid approach, J. Comput. Phys. 257 (2014) 278–297. https://doi.org/10.1016/j.jcp.2013.10.004.

[89] D. Korba, N. Wang, L. Li, Accuracy of interface schemes for conjugate heat and mass transfer in the lattice Boltzmann method, Int. J. Heat Mass Transf. (2020). https://doi.org/10.1016/j.ijheatmasstransfer.2020.119694.

[90] P. Lallemand, L.S. Luo, Theory of the lattice Boltzmann method: Acoustic and thermal properties in two and three dimensions, Phys. Rev. E - Stat. Physics, Plasmas, Fluids, Relat. Interdiscip. Top. 68 (2003) 25. https://doi.org/10.1103/PhysRevE.68.036706.

[91] Z. Guo, C. Zheng, B. Shi, T.S. Zhao, Thermal lattice Boltzmann equation for low Mach number flows: Decoupling model, Phys. Rev. E - Stat. Nonlinear, Soft Matter Phys. 75 (2007) 1–15. https://doi.org/10.1103/PhysRevE.75.036704.

[92] B. Shi, Z. Guo, Lattice Boltzmann model for nonlinear convection-diffusion equations, Phys. Rev. E - Stat. Nonlinear, Soft Matter Phys. 79 (2009) 1–13. https://doi.org/10.1103/PhysRevE.79.016701.

[93] L. Li, R. Mei, J.F. Klausner, Heat Transfer Evaluation on Curved Boundaries in Thermal Lattice Boltzmann Equation Method, J. Heat Transfer. 136 (2014) 012403. https://doi.org/10.1115/1.4025046.

[94] G. Le, O. Oulaid, J. Zhang, Counter-extrapolation method for conjugate interfaces in computational heat and mass transfer, Phys. Rev. E. 91 (2015) 33306. https://doi.org/10.1103/PhysRevE.91.033306.

[95] J. Huang, W.-A. Yong, Boundary conditions of the lattice Boltzmann method for convection–diffusion equations, J. Comput. Phys. 300 (2015) 70–91. https://doi.org/10.1016/J.JCP.2015.07.045.

[96] H. Karani, C. Huber, Lattice Boltzmann formulation for conjugate heat transfer in heterogeneous media, Phys. Rev. E - Stat. Nonlinear, Soft Matter Phys. (2015). https://doi.org/10.1103/PhysRevE.91.023304.

[97] J.H. Lu, H.Y. Lei, C.S. Dai, A unified thermal lattice Boltzmann equation for conjugate heat transfer problem, Int. J. Heat Mass Transf. 126 (2018) 1275–1286. https://doi.org/10.1016/J.IJHEATMASSTRANSFER.2018.06.031.

[98] R. Huang, H. Wu, P. Cheng, A new lattice Boltzmann model for solid-liquid phase change, Int. J. Heat Mass Transf. 59 (2013) 295–301. https://doi.org/10.1016/j.ijheatmasstransfer.2012.12.027.

[99] R. Huang, H. Wu, Phase interface effects in the total enthalpy-based lattice Boltzmann model for solid-liquid phase change, J. Comput. Phys. 294 (2015) 346–362. https://doi.org/10.1016/j.jcp.2015.03.064.

[100] Y. Hu, D. Li, S. Shu, X. Niu, Full Eulerian lattice Boltzmann model for conjugate heat transfer, Phys. Rev. E - Stat. Nonlinear, Soft Matter Phys. 92 (2015). https://doi.org/10.1103/PhysRevE.92.063305.

[101] Y. Hu, D. Li, S. Shu, X. Niu, Simulation of steady fluid-solid conjugate heat transfer problems via immersed boundary-lattice Boltzmann method, Comput. Math. with Appl. 70 (2015) 2227–2237. https://doi.org/10.1016/j.camwa.2015.08.024.

[102] S. Chen, Y.Y. Yan, W. Gong, A simple lattice Boltzmann model for conjugate heat transfer research, Int. J. Heat Mass Transf. 107 (2017) 862–870. https://doi.org/10.1016/j.ijheatmasstransfer.2016.10.120.

[103] H. Rihab, N. Moudhaffar, B.N. Sassi, P. Patrick, Enthalpic lattice Boltzmann formulation for unsteady heat conduction in heterogeneous media, Int. J. Heat Mass Transf. 100 (2016) 728–736. https://doi.org/10.1016/j.ijheatmasstransfer.2016.05.001.

[104] S. Chen, Simulation of conjugate heat transfer between fluid-saturated porous media and solid wall, Int. J. Therm. Sci. 124 (2018) 477–483. https://doi.org/10.1016/j.ijthermalsci.2017.10.039.

[105] S. Chen, B. Yang, C. Zheng, A lattice Boltzmann model for heat transfer in heterogeneous media, Int. J. Heat Mass Transf. 102 (2016) 637–644. https://doi.org/10.1016/j.ijheatmasstransfer.2016.06.082.

[106] D. Gao, Z. Chen, L. Chen, D. Zhang, A modified lattice Boltzmann model for conjugate heat transfer in porous media, Int. J. Heat Mass Transf. 105 (2017) 673–683. https://doi.org/10.1016/j.ijheatmasstransfer.2016.10.023.

[107] J.H. Lu, H.Y. Lei, C.S. Dai, A lattice Boltzmann algorithm for simulating conjugate heat transfer through virtual heat capacity correction, Int. J. Therm. Sci. 116 (2017) 22–31. https://doi.org/10.1016/j.ijthermalsci.2017.02.006.

[108] H. Chen, S. Chen, W.H. Matthaeus, Recovery of the Navier-Stokes equations using a lattice-gas Boltzmann method, Phys. Rev. A. 45 (1992) 5339–5342. https://doi.org/10.1103/PhysRevA.45.R5339.

[109] I. Ginzburg, Equilibrium-type and link-type lattice Boltzmann models for generic advection and anisotropic-dispersion equation, Adv. Water Resour. 28 (2005) 1171–1195. https://doi.org/10.1016/j.advwatres.2005.03.004.

[110] L. Li, R. Mei, J.F. Klausner, Heat transfer evaluation on curved boundaries in thermal lattice boltzmann equation method, J. Heat Transfer. (2014). https://doi.org/10.1115/1.4025046.

[111] N. Wang, I. Kaur, P. Singh, L. Li, Prediction of effective thermal conductivity of porous lattice structures and validation with additively manufactured metal foams, Appl. Therm. Eng. (2021). https://doi.org/10.1016/j.applthermaleng.2021.116558.

[112] J. Wang, M. Wang, Z. Li, A lattice Boltzmann algorithm for fluid-solid conjugate heat transferstar, Int. J. Therm. Sci. 46 (2007) 228–234. https://doi.org/10.1016/j.ijthermalsci.2006.04.012.

[113] M. Wang, N. Pan, Modeling and prediction of the effective thermal conductivity of random open-cell porous foams, Int. J. Heat Mass Transf. (2008). https://doi.org/10.1016/j.ijheatmasstransfer.2007.11.031.

[114] K. Boomsma, D. Poulikakos, Y. Ventikos, Simulations of flow through open cell metal foams using an idealized periodic cell structure, Int. J. Heat Fluid Flow. (2003). https://doi.org/10.1016/j.ijheatfluidflow.2003.08.002.

[115] M. Iasiello, S. Cunsolo, M. Oliviero, W.M. Harris, N. Bianco, W.K.S. Chiu, V. Naso, Numerical analysis of heat transfer and pressure drop in metal foams for different morphological models, J. Heat Transfer. (2014). https://doi.org/10.1115/1.4028113.

[116] X. Yang, X. Meng, Z. Wang, L. Jin, Q. Zhang, Q. Zhang, T.J. Lu, Direct Numerical Simulation on Melting Phase Change Behavior in Open-cell Metal Foam, in: Energy Procedia, 2017. https://doi.org/10.1016/j.egypro.2017.03.915.

[117] X. Zheng, H. Lee, T.H. Weisgraber, M. Shusteff, J. DeOtte, E.B. Duoss, J.D. Kuntz, M.M. Biener, Q. Ge, J.A. Jackson, S.O. Kucheyev, N.X. Fang, C.M. Spadaccini, Ultralight, ultrastiff mechanical metamaterials, Science (80-.). 344 (2014) 1373–1377. https://doi.org/10.1126/science.1252291.

[118] R.M. Hensleigh, H. Cui, J.S. Oakdale, J.C. Ye, P.G. Campbell, E.B. Duoss, C.M. Spadaccini, X. Zheng, M.A. Worsley, Additive manufacturing of complex micro-architected graphene aerogels, Mater. Horizons. 5 (2018) 1035–1041. https://doi.org/10.1039/c8mh00668g.

[119] Z. Xu, C.S. Ha, R. Kadam, J. Lindahl, S. Kim, H.F. Wu, V. Kunc, X. Zheng, Additive manufacturing of two-phase lightweight, stiff and high damping carbon fiber reinforced polymer microlattices, Addit. Manuf. 32 (2020) 101106. https://doi.org/10.1016/j.addma.2020.101106.

[120] V.S. Deshpande, N.A. Fleck, M.F. Ashby, Effective properties of the octet-truss lattice material, J. Mech. Phys. Solids. (2001). https://doi.org/10.1016/S0022-5096(01)00010-2.

[121] L. Dong, V. Deshpande, H. Wadley, Mechanical response of Ti-6Al-4V octet-truss lattice structures, Int. J. Solids Struct. (2015). https://doi.org/10.1016/j.ijsolstr.2015.02.020.

[122] I. Kaur, P. Singh, Flow and Thermal Transport Through Unit Cell Topologies of Cubic and Octahedron Families, Int. J. Heat Mass Transf. (2020). https://doi.org/10.1016/j.ijheatmasstransfer.2020.119784.

[123] M. Bai, J.N. Chung, Analytical and numerical prediction of heat transfer and pressure drop in open-cell metal foams, Int. J. Therm. Sci. (2011). https://doi.org/10.1016/j.ijthermalsci.2011.01.007.

[124] S. Krishnan, S. V. Garimella, J.Y. Murthy, Simulation of thermal transport in open-cell metal foams: Effect of periodic unit-cell structure, J. Heat Transfer. (2008). https://doi.org/10.1115/1.2789718.

[125] X. Yang, Q. Bai, Z. Guo, Z. Niu, C. Yang, L. Jin, T.J. Lu, J. Yan, Comparison of direct numerical simulation with volume-averaged method on composite phase change materials for thermal energy storage, Appl. Energy. (2018). https://doi.org/10.1016/j.apenergy.2018.08.012.

[126] H. Yoshida, M. Nagaoka, Multiple-relaxation-time lattice Boltzmann model for the convection and anisotropic diffusion equation, J. Comput. Phys. 229 (2010) 7774–7795. https://doi.org/10.1016/j.jcp.2010.06.037.

[127] Y. Yao, H. Wu, Z. Liu, Pore Scale Investigation of Heat Conduction of High Porosity Open-Cell Metal Foam/Paraffin Composite, J. Heat Transfer. (2017). https://doi.org/10.1115/1.4036526.

[128] M. Iasiello, N. Bianco, W.K.S. Chiu, V. Naso, Thermal conduction in open-cell metal foams: Anisotropy and Representative Volume Element, Int. J. Therm. Sci. (2019). https://doi.org/10.1016/j.ijthermalsci.2018.12.002.

[129] G.N. Dul'nev, Heat transfer through solid disperse systems, J. Eng. Phys. (1965). https://doi.org/10.1007/BF00828349.

[130] R.J. Moffat, Describing the uncertainties in experimental results, Exp. Therm. Fluid Sci. (1988). https://doi.org/10.1016/0894-1777(88)90043-X.

[131] T. Belcher, G. Schunk, Thermal Characterization of 3D Printed Lattice Structures, Therm. Fluids Anal. Work. TFAWS 2019, Hampt. VA. (2019).

[132] R. Lemlich, A theory for the limiting conductivity of polyhedral foam at low density, J. Colloid Interface Sci. (1978). https://doi.org/10.1016/0021-9797(78)90339-9.

[133] N. Wang, D. Korba, Z. Liu, R. Prabhu, M.W. Priddy, S. Yang, L. Chen, L. Li, Phase-field-lattice Boltzmann method for dendritic growth with melt flow and thermosolutal convection–diffusion, Comput. Methods Appl. Mech. Eng. (2021). https://doi.org/10.1016/j.cma.2021.114026.

[134] A. Cartalade, A. Younsi, M. Plapp, Lattice Boltzmann simulations of 3D crystal growth: Numerical schemes for a phase-field model with anti-trapping current, Comput. Math. with Appl. (2016). https://doi.org/10.1016/j.camwa.2016.02.029.

[135] A. Younsi, A. Cartalade, On anisotropy function in crystal growth simulations using Lattice Boltzmann equation, J. Comput. Phys. (2016). https://doi.org/10.1016/j.jcp.2016.08.014.

[136] D. Sun, H. Xing, X. Dong, Y. Han, An anisotropic lattice Boltzmann – Phase field scheme for numerical simulations of dendritic growth with melt convection, Int. J. Heat Mass Transf. (2019). https://doi.org/10.1016/j.ijheatmasstransfer.2018.12.095.

[137] X. Wang, D. Sun, H. Xing, Y. Han, Y. Liu, J. Wang, Numerical modeling of equiaxed crystal growth in solidification of binary alloys using a lattice Boltzmann-finite volume scheme, Comput. Mater. Sci. 184 (2020) 109855. https://doi.org/10.1016/j.commatsci.2020.109855.

[138] A. Karma, Phase-field formulation for quantitative modeling of alloy solidification, Phys. Rev. Lett. (2001). https://doi.org/10.1103/PhysRevLett.87.115701.

[139] A. Zhang, J. Du, J. Yang, Z. Guo, Q. Wang, B. Jiang, F. Pan, S. Xiong, General hierarchical structure to solve transport phenomena with dissimilar time scales: Application in large-scale three-dimensional thermosolutal phase-field problems, Phys. Rev. E. 102 (2020) 43313. https://doi.org/10.1103/PhysRevE.102.043313.

[140] Z. Guo, J. Mi, P.S. Grant, An implicit parallel multigrid computing scheme to solve coupled thermal-solute phase-field equations for dendrite evolution, J. Comput. Phys. 231 (2012) 1781–1796. https://doi.org/10.1016/j.jcp.2011.11.006.

[141] Z. Guo, S.M. Xiong, On solving the 3-D phase field equations by employing a parallel-adaptive mesh refinement (Para-AMR) algorithm, Comput. Phys. Commun. 190 (2015) 89–97. https://doi.org/10.1016/j.cpc.2015.01.016.

[142] L. Rátkai, T. Pusztai, L. Gránásy, Phase-field lattice Boltzmann model for dendrites growing and moving in melt flow, Npj Comput. Mater. 5 (2019). https://doi.org/10.1038/s41524-019-0250-8.

[143] S. Meng, A. Zhang, Z. Guo, Q. Wang, Phase-field-lattice Boltzmann simulation of dendrite motion using an immersed boundary method, Comput. Mater. Sci. 184 (2020) 109784. https://doi.org/10.1016/j.commatsci.2020.109784.

[144] J.H. Jeong, N. Goldenfeld, J.A. Dantzig, Phase field model for three-dimensional dendritic growth with fluid flow, Phys. Rev. E - Stat. Physics, Plasmas, Fluids, Relat. Interdiscip. Top. (2001). https://doi.org/10.1103/PhysRevE.64.041602.

[145] S.D.C. Walsh, M.O. Saar, Macroscale lattice-Boltzmann methods for low Peclet number solute and heat transport in heterogeneous porous media, Water Resour. Res. (2010). https://doi.org/10.1029/2009wr007895.

[146] P.L. Bhatnagarp, E.P. Gross, A.M. Krook, A Model for Collision Processes in Gases. I. Small Amplitude Processes in Charged and Neutral One-Component Systems, Phys. Rev. 94 (1954) 511–525.

[147] I. D'Humieres, Dominique Ginzburg, M. Krafczyk, P. Lallemand, L.-S. Luo, Multiple-relaxation-time lattice Boltzmann models in three dimensions, Philos. Trans. A. Math. Phys. Eng. Sci. 360 (2011) 437–451.

[148] P. Lallemand, L.-S. Luo, Theory of the lattice Boltzmann method: Dispersion, dissipation, isotropy, Galilean invariance, and stability, Phys. Rev. E. 61 (2000) 6546–6562. https://doi.org/10.1103/PhysRevE.61.6546.

[149] C. Chen, L. Li, R. Mei, J.F. Klausner, Chapman–Enskog Analyses on the Gray Lattice Boltzmann Equation Method for Fluid Flow in Porous Media, J. Stat. Phys. (2018). https://doi.org/10.1007/s10955-018-2005-1.

[150] H. Yoshida, H. Hayashi, Transmission-Reflection Coefficient in the Lattice Boltzmann Method, J. Stat. Phys. (2014). https://doi.org/10.1007/s10955-014-0953-7.

[151] I. Ginzburg, Comment on "An improved gray Lattice Boltzmann model for simulating fluid flow in multi-scale porous media": Intrinsic links between LBE Brinkman schemes, Adv. Water Resour. 88 (2016) 241–249. https://doi.org/10.1016/j.advwatres.2014.05.007.

[152] S. Sakane, T. Takaki, M. Ohno, Y. Shibuta, T. Aoki, Two-dimensional large-scale phase-field lattice Boltzmann simulation of polycrystalline equiaxed solidification with motion of a massive number of dendrites, Comput. Mater. Sci. 178 (2020) 109639. https://doi.org/10.1016/j.commatsci.2020.109639.

[153] L. Li, Multiple-time-scaling lattice Boltzmann method for the convection diffusion equation, Phys. Rev. E. 99 (2019) 1–13. https://doi.org/10.1103/PhysRevE.99.063301.

[154] M. Zhu, D. Sun, S. Pan, Q. Zhang, D. Raabe, Modelling of dendritic growth during alloy solidification under natural convection, Model. Simul. Mater. Sci. Eng. (2014). https://doi.org/10.1088/0965-0393/22/3/034006.

[155] Z. Chai, B. Shi, Multiple-relaxation-time lattice Boltzmann method for the Navier-Stokes and nonlinear convection-diffusion equations: Modeling, analysis, and elements, Phys. Rev. E. 102 (2020). https://doi.org/10.1103/PhysRevE.102.023306.

I

CHAPMAN-ENSKOG ANALYSIS OF THE MRT-LBM FOR THE PHASE-FIELD EQUATION

For the Chapman-Enskog expansion analysis, a "small" perturbation parameter ϵ, which is defined as the ratio of the lattice spacing δx to a characteristic macroscopic length L, i.e., $\epsilon \equiv \delta x/L$, is applied. The standard spatial scale $\mathbf{x}_1 = \epsilon \mathbf{x}$ and two time scales $t_1 = \epsilon\, t$ and $t_2 = \epsilon^2 t$ (hence $\nabla = \grave{o}\nabla_1$, $\partial_t = \grave{o}\partial_{t_1} + \grave{o}^2\partial_{t_2}$) are considered for the analysis, with also the following expansions introduced

$$g_\alpha = \sum_{n=0}^{\infty} \grave{o}^n g_\alpha^{(n)}, \tag{A.1}$$

$$g_\alpha\left(\mathbf{x}+\mathbf{e}_\alpha\delta t, t\right) = \sum_{n=0}^{\infty} \frac{\grave{o}^n}{n!}\mathbf{d}^n g_\alpha^{(n)}\left(\mathbf{x}, t\right), \tag{A.2}$$

$$g_\alpha\left(\mathbf{x}+\mathbf{e}_\alpha\delta t, t+\delta t\right) = \sum_{n=0}^{\infty} \frac{\grave{o}^n}{n!}\mathbf{D}^n g_\alpha^{(n)}\left(\mathbf{x}, t\right), \tag{A.3}$$

where $\mathbf{d} = \mathbf{e}_\alpha \cdot \nabla$, and $\mathbf{D} = \dfrac{\partial}{\partial t} + \mathbf{e}_\alpha \cdot \nabla$ is the convective derivative.

Following the similar steps in [134,145,149,155], one can insert the above expansions and rewrite the MRT-LB scheme in Eq. (4.21) in the consecutive orders of the parameter ϵ as follows

$$\mathrm{O}\left(\grave{o}^0\right): \mathbf{\Lambda}_{\alpha\beta}\left[g_\beta^{(0)} - g_\beta^{\mathrm{eq}}\right] = 0, \tag{A.4}$$

$$\mathrm{O}\left(\grave{o}^1\right): -\frac{1}{\delta t}\mathbf{\Lambda}_{\alpha\beta} g_\beta^{(1)} = \tilde{\mathbf{D}}_{1\alpha} g_\alpha^{(0)}, \tag{A.5}$$

$$\mathrm{O}\left(\grave{o}^2\right): -\frac{1}{\delta t}\mathbf{\Lambda}_{\alpha\beta} g_\beta^{(2)} = a_s^2\partial_{t_2} g_\alpha^{(0)} + \tilde{\mathbf{D}}_{1\alpha} g_\alpha^{(1)} + \frac{\delta t}{2}\tilde{\mathbf{D}}_{1\alpha}^2 g_\alpha^{(0)}, \tag{A.6}$$

where $\mathbf{\Lambda} \equiv \mathbf{M}^{-1}\mathbf{S}\mathbf{M}$ and $\tilde{\mathbf{D}}_{1\alpha} = a_s^2 \dfrac{\partial}{\partial t_1} + \mathbf{e}_\alpha \cdot \nabla_1$.

Since $\mathbf{\Lambda}$ is invertible, Eq. (A.4) simply implies

$$g_\alpha^{(0)} = g_\alpha^{\mathrm{eq}}. \tag{A.7}$$

Also, the combination of Eqs. (A.5, A.6) gives

$$-\frac{1}{\delta t}\mathbf{\Lambda}_{\alpha\beta} g_\beta^{(2)} = a_s^2\partial_{t_2} g_\alpha^{(0)} + \tilde{\mathbf{D}}_{1\alpha}\left(\mathbf{I} - \mathbf{\Lambda}/2\right)_{\alpha\beta} g_\beta^{(1)}. \tag{A.8}$$

From the zeroth-order moments of $g_\alpha^{(1)}$ in Eq. (A.5) and $g_\alpha^{(2)}$ in Eq. (A.8) one can obtain

$$a_s^2\partial_{t_1}\left(\sum_\alpha g_\alpha^{(0)}\right) + \nabla_1 \cdot \left(\sum_\alpha \mathbf{e}_\alpha g_\alpha^{(0)}\right) = 0, \tag{A.9}$$

$$a_s^2\partial_{t_2}\left(\sum_\alpha g_\alpha^{(0)}\right)+\nabla_1\cdot\left[\left(\mathbf{I}-\mathbf{S}_1/2\right)_{\alpha\beta}\sum_\alpha \mathbf{e}_\alpha g_\alpha^{(1)}\right]=0\,, \tag{A.10}$$

where the following relations are noted

$$\sum_\alpha \mathbf{c}_\alpha \mathbf{\Lambda}_{\alpha\beta}=s_0\mathbf{c}_\beta,\ \sum_\alpha \mathbf{e}_\alpha \mathbf{\Lambda}_{\alpha\beta}=\mathbf{S}_{10}\mathbf{c}_\beta+\mathbf{S}_1\mathbf{e}_\beta\,, \tag{A.11}$$

with $\mathbf{c}=(1, 1, \ldots, 1)\in R^m$, s_0 a constant parameter, $\mathbf{S}_{10}$ a $m\times 1$ matrix, and $\mathbf{S}_1$ an invertible $m\times m$ relaxation matrix corresponding to the diffusion matrix [155].

Also from the first-order moment of $g_\alpha^{(1)}$ we obtain

$$\begin{aligned}\sum_\alpha \mathbf{e}_\alpha g_\alpha^{(1)}&=-\delta t\sum_\alpha \mathbf{e}_\alpha \mathbf{\Lambda}_{\alpha\gamma}^{-1}\tilde{\mathbf{D}}_{1\gamma}g_\gamma^{(0)}=-\delta t\mathbf{S}_1^{-1}\sum_\gamma \mathbf{e}_\gamma\tilde{\mathbf{D}}_{1\gamma}g_\gamma^{(0)}\\&=-\delta t\mathbf{S}_1^{-1}\left[a_s^2\partial_{t_1}\left(\sum_\alpha \mathbf{e}_\alpha g_\alpha^{(0)}\right)+\nabla_1\cdot\sum_\alpha \mathbf{e}_\alpha\mathbf{e}_\alpha g_\alpha^{(0)}\right].\end{aligned} \tag{A.12}$$

Eq. (A.12) can be inserted into (A.10) to yield

$$\begin{aligned}a_s^2\partial_{t_2}\left(\sum_\alpha g_\alpha^{(0)}\right)&=\delta t\nabla_1\cdot\left[\left(\mathbf{S}_1^{-1}-\mathbf{I}/2\right)\nabla_1\cdot\sum_\alpha \mathbf{e}_\alpha\mathbf{e}_\alpha g_\alpha^{(0)}\right]\\&\quad+\delta t\nabla_1\cdot\left[\left(\mathbf{S}_1^{-1}-\mathbf{I}/2\right)a_s^2\partial_{t_1}\sum_\alpha \mathbf{e}_\alpha g_\alpha^{(0)}\right].\end{aligned} \tag{A.13}$$

With the appropriate selection of $g_\alpha^{(0)}=g_\alpha^{\mathrm{eq}}$, $\partial_{t_1}\sum_\alpha \mathbf{e}_\alpha g_\alpha^{(0)}=0$ is noted and thus Eq. (A.13) reduces to

$$a_s^2\partial_{t_2}\left(\sum_\alpha g_\alpha^{(0)}\right)=\delta t\nabla_1\cdot\left[\left(\mathbf{S}_1^{-1}-\mathbf{I}/2\right)\nabla_1\cdot\sum_\alpha \mathbf{e}_\alpha\mathbf{e}_\alpha g_\alpha^{(0)}\right]. \tag{A.14}$$

Finally, we can combine the terms in $\epsilon\times$ Eq. (A.9), $\epsilon^2\times$ Eq. (A.14) and the source term of $O(\epsilon^2)$ to obtain

$$a_s^2\partial_t\left(\sum_\alpha g_\alpha^{(0)}\right)+\nabla\cdot\left(\sum_\alpha \mathbf{e}_\alpha g_\alpha^{(0)}\right)=\delta t\nabla\cdot\left[\left(\mathbf{S}_1^{-1}-\mathbf{I}/2\right)\nabla\cdot\sum_\alpha \mathbf{e}_\alpha\mathbf{e}_\alpha g_\alpha^{(0)}\right]+\delta t\sum_\alpha\frac{\omega_\alpha G_\phi}{F(U)\tau_0}\,. \tag{A.15}$$

Clearly, with g_α^{eq} defined in Eq. (4.26), $\sum_\alpha g_\alpha^{(0)}=\phi$, $\sum_\alpha \mathbf{e}_\alpha g_\alpha^{(0)}=-\mathbf{N}\frac{W_0^2}{F(U)\tau_0}\frac{\delta t}{\delta x}$ and $\sum_\alpha \mathbf{e}_\alpha\mathbf{e}_\alpha g_\alpha^{(0)}=\xi\phi\mathbf{I}$ can be readily verified; also, recalling the relaxation matrix in Eq. (4.27), Eq. (A.15) becomes

$$a_s^2 \partial_t \phi = \nabla \cdot \left[\frac{a_s^2}{F(U)} \frac{W_0^2}{\tau_0} \nabla \phi \right] + \frac{W_0^2}{\tau_0} \nabla \cdot \frac{\mathbf{N}}{F(U)} + \frac{G_\phi}{F(U)\tau_0} . \tag{A.16}$$

Eq. (A.16) is identical to the governing equation in (4.20) when preserving the terms up to $O(\epsilon^2)$. It is thus verified that the MRT-LB evolution scheme in Eq. (4.21) recovers the governing equation for the phase field up to second-order accuracy.

I

EVALUATION OF THE TIP VELOCITY AND RADIUS

With the objective of accurately evaluating the tip velocity and tip radius during the dendritic growth, bi-cubic interpolation using 16 data points of the phase field variable, ϕ_{ij}, (i = 1 ~ 4, j = 1 ~ 4) enclosing each tip is applied. Through the introduction of a local coordinate system (ξ, η), the bi-cubic function is constructed as $\phi(\xi,\eta)=\sum_{\alpha=0}^{3}\sum_{\beta=0}^{3}C_{\alpha\beta}\xi^{\alpha}\eta^{\beta}$ where $C_{\alpha\beta}$ are constant coefficients that can be easily determined with the ϕ_{ij} values from the phase-field solution. In addition, the Newton-Raphson method for root-finding in 2D is employed to accurately determine the tip coordinates (ξ_t, η_t) that satisfy the two conditions of $\phi(\xi_t,\eta_t)=0$, and $\left.\frac{\partial\phi}{\partial\xi}\right|_{(\xi_t,\eta_t)}=0$ (for north and south tips) or $\left.\frac{\partial\phi}{\partial\eta}\right|_{(\xi_t,\eta_t)}=0$ (for west and east tips). After determining the tip coordinates, the tip velocity can be readily calculated in the time marching procedure, and the tip radius is analytically calculated according to $\rho_{\text{tip}}=\frac{\partial_{\eta}\phi\big|_{(\xi_t,\eta_t)}}{\partial_{\xi}^{2}\phi\big|_{(\xi_t,\eta_t)}}$ (for north and south tips) and $\rho_{\text{tip}}=\frac{\partial_{\xi}\phi\big|_{(\xi_t,\eta_t)}}{\partial_{\eta}^{2}\phi\big|_{(\xi_t,\eta_t)}}$ (for west and east tips).

For 3D simulations, the center of the initial spherical seed is placed exactly on a lattice node, and the tip velocity and radius are evaluated on the selected 2D planes following the same process described above.